RIM4 deficiency leads to reduced somato-dendritic excitability of cerebellar Purkinje cells

Doctoral thesis

to obtain a doctorate (PhD)

from the Faculty of Medicine

of the University of Bonn

Hyuntae Kim
from Daejoen, South Korea
2023

Written with authorization of

the Faculty of Medicine of the University of Bonn

First reviewer: Prof. Dr. med. Dirk Dietrich

Second reviewer: Prof. Dr. med. Jens Eilers

Day of oral examination: 14. November. 2023

For the clinic and policlinic for Neurosurgery

Director: Prof. Dr. med. Hartmut Vatter

Table of Contents

List of abbreviations

ANOVA	Analysis of variance
AP	Action potential
AZ	Active zone
BK channel	the large conductance voltage- and Ca^{2+}-dependent K^+ channel
$Ca_v2.1$	P/Q-type voltage-gated Ca^{2+} channel
CB	Cerebellum
CF	Climbing fiber
CS	Complex spike
CV_{ISI}	coefficient of variation of inter-spike interval
CX	Cortex
DCN	Deep cerebellar nuclei
DHPG	(S)-3,5-Dihydroxyphenylglycine
DIC	Differential interference contrast
EA	Episodic ataxia
eIPSC	Evoked inhibitory postsynaptic current
EPSC	Excitatory postsynaptic current
fAHP	Fast afterhyperpolarization
GABA	γ-Aminobutyric acid
GC	Granule cell
GCL	Granule cell layer

HC	Hippocampus
IEI	Inter-event interval
ISI	Inter-spike interval
mACSF	Modified artificial cerebrospinal fluid
MF	Mossy fiber
mGluR	Metabotropic glutamate receptor
MIP	Maximum intensity projection
ML	Molecular layer
MLI	Molecular layer interneuron
OE	Overexpression
PC	Purkinje cell
PCL	Purkinje cell layer
PDZ	An acronym derived from proteins: Postsynaptic density protein, Drosophila disc large tumor suppressor, Zonula occludens-1
PF	Parallel fiber
PMT	Photo multiplier
PPD	Paired-pulse depression
PPR	Paired-pulse ratio
R_a	Access resistance
RIM	Rab3-interacting molecule
RIM-BP	RIM-binding protein
R_s	Series resistance

RT	Room temperature
sACSF	Standard artificial cerebrospinal fluid
SCA	Spinocerebellar ataxia
sIPSC	Spontaneous inhibitory postsynaptic current
SK channel	Small-conductance Ca^{2+}-activated K^+ channel
SS	Simple spike
SV	Synaptic vesicle
TRPC	Transient receptor potential channel
VGCC	Voltage-gated calcium channel
VGKC, K_v channel	Voltage-gated potassium channel
VGlut	Vesicular glutamate channel
VGSC, Na_v channel	Voltage-gated sodium channel
WM	White matter
ZF	Zn^{2+}-finger domain
$[Ca^{2+}]_e$	Extracellular calcium concentration

1. Introduction

It was one of the greatest beginnings of neuroscience when Santiago Ramón y Cajal, a Spanish neuroscientist, reported in the first issue of the *Revista Trimestral de Histología Normal y Patológica* in May 1888 a hyphothesis that nerve cells are not continuous, which was the first recognition of a synapse. Using a method developed by one of his great contemporaries Camillo Golgi, the so-called the Golgi staining, Cajal overcame technical limitations of microscopy and revealed the fundamental structure of the nervous system. For this groundbreaking discovery, Cajal received a Nobel Prize in Physiology or Medicine together with Camillo Golgi in 1906. In the 1950s, Cajal's findings were eventually refined along with the development of electron microscopy (Palay and Palade, 1955).

1.1 The synapse and active zone proteins

The brain is composed of countless neurons, which are elaborately interconnected by a complex network of synapses, where neuronal information is transmitted from one neuron to another one via either neurotransmitter release and diffusion or direct ion exchange. Synapses can be subdivided into two types: electrical and chemical synapses. Electrical synapses are capable of transmitting electric signals rapidly to neighboring cells due to a narrow gap between them. In the chemical synapse, synaptic vesicles (SVs) are involved in relaying neuronal information by releasing neurotransmitters into a synaptic cleft, where they bind to specific receptors localized on the receiving neuron.

The active zone (AZ) is a highly specialized area of the presynaptic plasma membrane. In the AZ, SVs containing neurotransmitters are clustered, docked, and primed in order to fuse rapidly with the plasma membrane when it is necessary. Arrival of an action potential (AP) at the axon terminal opens voltage-gated calcium channels (VGCCs) resulting in the influx of Ca^{2+}, which binds to Ca^{2+}-sensors located on SVs triggering exocytosis of SVs and release of neurotransmitter into the synaptic cleft (Katz, 1969). At the AZ, numerous proteins form a network regulating this elaborate process: Rab3-interacting molecules (RIMs), Munc13/18, SNARE complex, Piccolo, Basoon, and SV proteins, including Rab3, and Synaptotagmin-1 (Fig. 1).

In neuron, synaptic strength is plastically changing in response to its activity, and the plasticity of synaptic strength is one of the hallmarks of synaptic function. (Larrabee and

Bronk, 1947; Eccles and McIntyre, 1953). It has been elucidated that synaptic proteins modulate the exocytosis of the SVs (Schoch and Gundelfinger, 2006). The spatial arrangement of synaptic proteins is functionally pertinent to synaptic plasticity (Südhof, 2004). Synaptic plasticity has been extensively studied showing that it is crucial for animal behavior such as memory formation (reviewed in Neves et al., 2008) and motor learning (Piochon et al., 2014). Although we know the importance of synaptic function in animal, the exact mechanisms how synaptic proteins contribute to the cellular behavior, modifications of circuit connectivity, as well as animal behavior are not fully resolved.
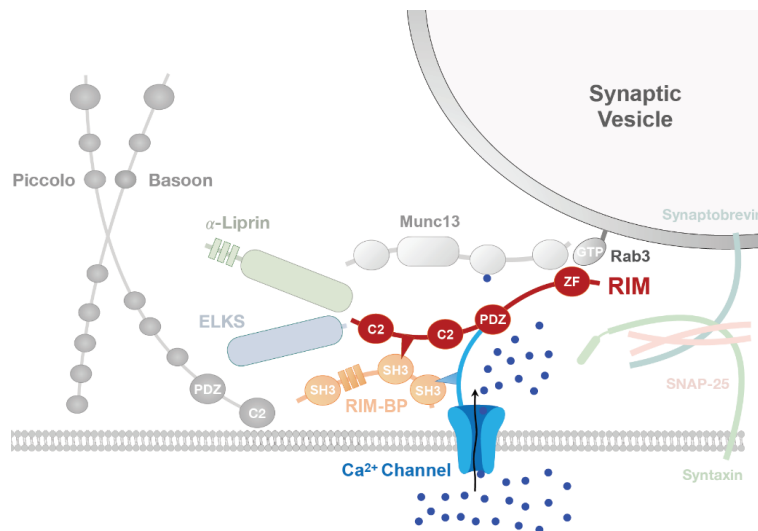
Figure 1.1: **Network of AZ proteins**. The key components of the presynaptic release machinery are depicted: RIM, RIM-binding protein (RIM-BP), Munc13, Ca^{2+}-channels, SV proteins including Rab3 and Synaptotagmin-1, and an assembled SNARE complex composed of synaptobrevin attached to SVs and SNAP-25 and Syntaxin on the plasma membrane. The figure was adapted from Kaeser et al., 2011.

1.2 RIM protein family

Within the cytomatrix at the AZ, RIMs are one of the central scaffolds interacting with many of the other AZ proteins and SVs via Rab-3, determine the density of Ca^{2+} channels and regulate neurotransmitter release (Wang et al., 1997; Wang et al., 2000; Schoch et al., 2002; Lu et al., 2005; Han et al., 2011; Kaeser et al., 2011). The RIM family consists of seven different isoforms that are encoded by four RIM genes (RIM 1-4) in the mammalian genome, which are expressed in three principal variants, α, β, and γ, by the usage of internal promoters. Out of these seven isoforms, four are large RIM isoforms (RIM1α/β and RIM2α/β), and three are small RIM isoforms (RIM2/3/4γ) (Wang and Südhof, 2003). Comprehensive studies of RIM unveiled its multiple domains. α-RIMs (RIM1α and

RIM2α) contain the entire set of RIM domains: an N-terminal Rab3-binding sequences, a Zinc-finger domain, a central PDZ domain, and two C-terminal C2A/B domains separated by proline-rich sequence which is the binding site of RIM-binding proteins (Fig. 1.2). β-RIMs are comparable to α-RIMs, but lack N-terminal Rab3-binding sequences (RIM1β) or both the N-terminals Rab3- and Munc13-binding sequences (RIM2β). γ-RIMs (RIM2/3/4γ) are smaller than the other isoforms and are composed only of C2B domains and isoform-specific N-terminals (Wang et al., 2000; Wang and Südhof, 2003; Kaeser et al., 2008).
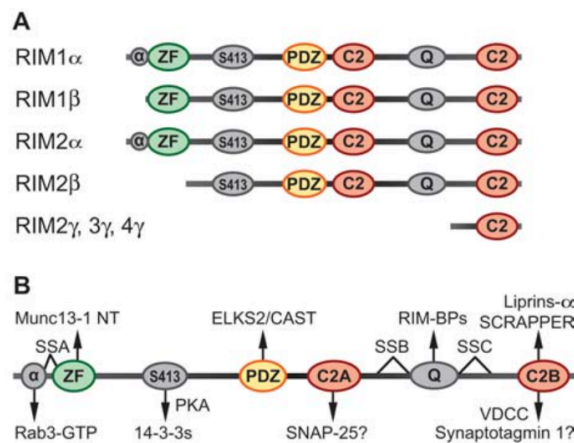
Figure 1.2: **The RIM family and its interaction domains**. A: The four RIM isoforms have a different composition of functional domains. α-RIMs (RIM1/2α) consist of the full RIM domains: A N-terminal Zn^{2+}-finger domain, a central PDZ domain, and C2A/B domains. β-RIMs are shorter than α-RIMs: RIM1β lacks only the N-terminal partially, RIM2β lacks both Zn^{2+}-finger domain and the part of the N-terminal. In contrast, smaller RIM isoforms (RIM2/3/4γ) have only C2B domain and an isoform-specific N-terminal. B: Functional domains of RIMs are where they interact with other synaptic proteins: From left, Helix α1 (α); Zn^{2+}-finger domain (ZF); Phosphorylation site for PKA, Serine 413 (S413); Postsynaptic density-95, Drosophila disc large tumor suppressor and zonula occludens-1 protein domain (PDZ); C2-domains (C2A/B); Proline rich sequence (Q); Splice sites in the RIM1/2 gene (SSA, SSB, SSC). Colored circles indicate the function domains (A, B) and arrows indicate the binding partners of RIMs (B). The figure was adapted from Mittelstaedt et al., 2010.

1.2.1 Large RIM isoforms: RIM1α/β and RIM2α/β

The majority of studies on RIMs were focused on the large RIM isoforms, which are the main scaffold proteins at the cytomatrix of the presynaptic AZ. Once the genetic structure of RIMs was revealed, the key functions of RIMs have been investigated by generating RIM deficient animal models. Genetic experiments performed in C. elegans, Drosphila and mice showed that the large RIMs are crucial for SV docking at the AZ, SV priming,

presynaptic plasticity and determining the density of Ca^{2+} channels (Koushika et al., 2001; Schoch et al., 2002; Han et al., 2011; Kaeser et al., 2011; Graf et al., 2012).

The presynaptic machinery brings SVs in close proximity to VGCCs at the AZ so that neurotransmitters are primed to be released. In electron micrographs of synapses, the fraction of docked SVs was drastically reduced in RIM1/2 double KO mice (Han et al., 2011; Kaeser et al., 2011). Furthermore, it was suggested that the tripartite interaction between RIM, Rab3 and VGCCs is essential for docking of SVs (Gracheva et al., 2008; Han et al., 2011). Determining the density of VGCCs at the AZ is another important function of the large RIM isoforms, which became apparent in conditional RIM1/2 double KO animals, which had drastically decreased levels of presynaptic VGCCs (Kaeser et al., 2011).

After docking, there is one further step, called priming, which brings the SVs even closer to the plasma membrane and enables the SVs to be ready for fast membrane fusion when action potential arrives by help of an assembled fusion machinery, such as Munc13-1 (Betz et al., 2001). SV priming determines the probability of neurotransmitter release and the size of the readily-releasable pool at a synapse. These two parameters determine the strength of the synapse. Synapses are able to change their strength plastically in response to neuronal activity within a short period (tens of milliseconds to several minutes; short-term plasticity) or a longer period (minutes to hours; long-term plasticity). Short-term plasticity is primarily a presynaptic feature, which can either enhance or depress the strength of a synapse. A paired-pulse stimulation, which can facilitate or depress neurotransmitter release in response to closely separated second stimulation, is a well-known method to examine the release probability at a synapse (Castillo and Katz, 1954; Dudel and Kuffler, 1968). It was reported that RIM1α-deficient mice showed increased paired-pulse facilitation at hippocampal CA3-CA1 synapses, which indicates a reduction in the probability of neurotransmitter release at these synapses (Schoch et al., 2002). In addition, ablation of the large RIM isoforms resulted in a strong reduction in calcium currents in the Calyx of Held, in cultured neurons, and in cerebellar granule cells, suggesting that the large RIM isoforms regulate neurotransmitter release in many neurons (Han et al., 2011; Kaeser et al., 2011; Kintscher et al., 2013). Synaptic plasticity is an important phenomenon in memory, learning, and social interaction which are abnormal in RIM1α KO animals (Powell et al., 2004; Blundell et al., 2010).

1.2.2 Small RIM isoforms: RIM3γ and RIM4γ

Unlike the large RIM isoforms, not much is known about the small RIM isoforms. As described above, γ-RIMs are composed of only one C2B domain and isoform-specific N-terminal sequences, lacking the majority of the protein interaction domains of the large RIMs (Wang and Südhof, 2003). According to Alvarez-Baron, Michel et al. (2013), γ-RIMs, RIM3γ and RIM4γ, have distinct expression patterns. In-situ hybridization micrographs showed the distribution of the mRNAs of both RIM3γ and RIM4γ highly expressed in the adult rat cerebellum. Specifically in the cerebellum, RIM3γ mRNA was observed in granule cells (GCs) while RIM4γ mRNA was most abundant in Purkinje cells (PCs). Moreover, the results of immunoblotting of rat brain homogenates supported these findings on the mRNA level. The strongest expression of RIM4γ protein was observed in the cerebellum. It was also detected in the cortex, hippocampus and olfactory bulb. During development in the brain, the expression of RIM3γ and RIM4γ increased and saturated around P15 for RIM4γ and P20 for RIM3γ (Alvarez-Baron and Michel et al., 2013).

The subcellular localization of RIM3γ and RIM4γ is distinct compared from the localization of the large RIM isoforms, especially at pre-synapses. The mRNA of RIM3γ was not only restricted in the soma, but also found in neuronal dendrites as well as in the postsynaptic densities shown by light and electron microscopy (Liang et al., 2007). According to the immunolabeling studies in cultured hippocampal neurons, RIM4γ exhibits a broader subcellular expression pattern, showing a distribution along the dendrites as well as axons (Alvarez-Baron and Michel et al., 2013).

In contrast to the large RIM isoforms, it is still not clear if RIM3γ and RIM4γ contribute to the modulation of neurotransmitter release even though they have been reported to bind to the b-subunit of VGCCs and suggested to regulate presynaptic Ca^{2+} influx (Uriu et al., 2010). Another study reported an interaction between the C2B domain of RIM3γ and VGCCs, specifically the C-terminus of the pore-forming α-subunit of $Ca_v1.3$ channels in cochlear inner hair cells (Picher et al., 2017).

Interestingly, RIM3γ and RIM4γ are important for establishing neuronal arborization. In cultured neurons, knock-down of either RIM3γ or RIM4γ drastically disrupted dendritic arborization. This morphological alteration was rescued by co-expression of shRNA resistant RIM3γ and RIM4γ together with the shRNAs (Alvarez-Baron and Michel et al., 2013). Affinity purification of tagged RIM3 and RIM4 from whole brain homogenate,

synaptosomes and cultured neurons identified novel binding partners of RIM3γ and RIM4γ suggesting an involvement of γ-RIMs in various cellular processes including neuronal arborization and vesicular trafficking (PhD thesis Katrin Michel, 2015). For example, the cell adhesion molecules - plakophilin4, δ-catenin and IQGAP3, involved in neuronal growth, - were found in the mass spectrometry data as interaction partners of RIM3γ and RIM4γ. Furthermore, proteins involved in vesicles formation and trafficking, like AP2 and AP3, were also identified.

1.2.3 γ-RIM-related neurological disorders

Proper information transfer from neuron to neuron and within neuronal networks is the prerequisite for normal brain function and deficits in this information flow has been linked to multiple neurological and cognitive disorders, like Alzheimer's disease, Parkinson's disease, epilepsy, schizophrenia, autism, and ataxia. Dysregulation of the synaptic machinery at the AZ alters synaptic transmission between neurons and may trigger neurological disorders. RIM proteins as one of the major synaptic proteins at the AZ have been associated with neurological disorders. For instance, schizophrenic behavior was found in RIM1α-lacking mice (Blundell et al., 2010). Schizophrenia patients showed an upregulation of the *RIMS3* gene, encoding RIM3γ, in the amygdala where it is important for processing emotions (Weidenhofer et al., 2006; Weidenhofer et al., 2009). A mutation of the *RIMS3* genes was also found in an autism patient (Kumar et al., 2010). Another study reported *de novo* truncating variants of in the *RIMS4* gene, encoding the RIM4γ protein, in autism patients (Leblond et al., 2019).

In order to investigate the functional role of RIM4, we produced constitutive RIM4 knock-out mice (RIM4 KO$_{const}$; K.Michel, Dissertation, 2015). The offspring of RIM4 KO$_{const}$ mice followed a mendelian distribution in their genotypes and all pups were viable (K.Michel, Dissertation, 2015). Both gene transcription and protein expression of RIM4 were abolished in the brain of RIM4 KO$_{const}$ mice. Interestingly, after the 3rd postnatal week, which is the time of weaning, RIM4 KO$_{const}$ mice had lower body weights than their WT littermates. More importantly, at the same time, they developed a strong episodic motor impairment in their hindlimbs. Monitoring of spontaneous episodes revealed that they occurred at least once every 24 hours and lasted one to four hours. The CatWalk system,

a video-based automatic analysis of gait, showed gait deficits in RIM4 KO$_{const}$ mice even in the absence of episodes (K.Michel, Dissertation, 2015).

1.3 The cerebellar cortex

Mammalian and avian as well as fish brain consist of two major masses: the cerebrum (a large mass, Lat. *great brain*) and the cerebellum (a small mass, the *little brain* in Latin). In humans, the cerebellum is attached to the bottom of the cerebrum and has a highly folded structure with finely spaced parallel valleculas. Its distinctive appearance was already recognized by Aristotle, who referred to it as *parenkephalis* (Marshall and Magoun, 1998). The size of the cerebellum varies across animals; in some fish it is larger than the cerebrum. The cerebellum is important for motor coordination and motor learning. In the 19th century, neurosurgeons observed that the surgical removal or lesion of all or part of the cerebellum influenced movement and caused disorders with impaired motor coordination. Although many studies revealed the importance of the cerebellum in fine motor control, the mechanisms explaining the linkage between neurological symptoms and specific alterations in the cerebellum are not fully understood yet.

1.3.1 Anatomy of the cerebellum

The cerebellum takes up only 10% of the total brain mass, but 80% of all brain neurons in humans and 60% in mice are located there (Herculano-Houzel et al., 2006; Azevedo et al., 2009). Interestingly, the proportion of neocortical and cerebellar neurons is conserved across mammalian species so that the cerebellum contains 3.6 times more neurons than the neocortex (Herculano-Houzel, 2010).

The cerebellum is a laminal structure composed of a highly folded cortex and white matter containing four deep cerebellar nuclei (DCN) surrounded by the fourth ventricle at the base. On a macro scale, the cerebellum as part of the metencephalon is located in the posterior cranial fossa. The cerebellum has two hemispheres like the cerebral cortex. The most medial region in the cerebellum is called the vermis surrounded by the paravermis on either side. Two fissures divide the cerebellum into three lobes: the primary deep fissure divides anterior and posterior lobes, while the posterior fissure separates the flocculonodular lobe from the posterior lobe. These regions can be further subdivided into 10 lobules (cerebellar lobules I-X) by shallow fissures (Fig. 1.3) (Sotelo and Wassef, 1991;

Cerminara et al., 2015). The cerebellar circuitry has been studied in detail, and its basic composition is maintained along the cerebellar cortex, which can be divided into three distinct layers: the molecular layer (ML), the Purkinje cell layer (PCL), and the granule cell layer (GCL). The ML is the outmost layer where the dendrites of Purkinje cells, climbing fibers (CFs), parallel fibers (PFs), and molecular layer interneurons (MLIs) are located. The innermost layer is the GCL. The GCL is mostly populated by GCs, although other cell types, such as Golgi cells and Lugaro cells, can also be found there. The PCL is located between these two layers. It is a monolayer formed by the somata of PCs as well as unipolar astrocytes called Bergmann glia (Fig. 1.3) (Apps and Garwicz, 2005; White and Sillitoe, 2013; Cerminara et al., 2015).
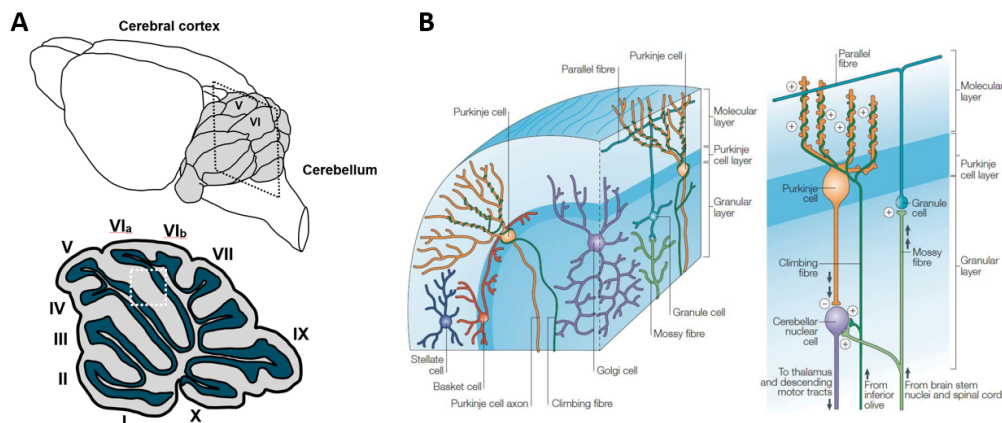
Figure 1.3. Gross anatomy of the mouse cerebellum and its basic structure. A. The cerebellum is a highly folded structure attached to the dorsal part of the cerebrum. The vermis is the most medial region of the cerebellum and consists of 10 cerebellar lobules (I-X). B. The cerebellar cortex consists of three layers: The Molecular layer, the Purkinje cell layer, and the Granule cell layer. The basic cellular composition of the cerebellar cortex includes Purkinje cells which are the main output neurons, Granule cells, Golgi cells, Stellate cells, and Basket cells. The two main afferents projecting to the cerebellum are the Climbing fibers which synapse directly with Purkinje cells by wrapping around their dendrites, and the Mossy fibers which synapse with Granule cells. The axons of the granule cells ascend along the Molecular layer where they bifurcate in a T-shaped fashion to form Parallel fibers, which connect with Purkinje cells making excitatory synaptic contacts. Adapted from Apps and Garwicz, 2005.

1.3.2 Spontaneous activity in cerebellar Purkinje cells

According to the type of neurotransmitter, neurons located in the cerebellar cortex can be classified into inhibitory γ-amminmobutyric acid (GABA)-ergic neurons and excitatory glutamatergic neurons. PCs are named after Jan Evangelista Purkyně, a Czech anatomist

and physiologist, who discovered them for the first time in 1837. PCs have an elaborate dendritic tree that extends into the ML as it was shown in Cajal's drawing.

As principal GABAergic neurons of the cerebellar cortex, PCs fire spontaneously with high frequencies even in the absence of synaptic inputs and the firing patterns as well as firing rate of PCs spikes are controlled by both synaptic inputs and intrinsic membrane properties (Häusser and Clark, 1997). Two types of APs are found in PCs: the simple spike (SS) and the complex spike (CS). CSs are evoked by inputs from CFs occurring at a low frequency (0.5-2 Hz) predominantly *in vivo*. The CS is a unique spike in PCs consisting of the initial large Na$^+$ spike followed by a burst of several small spikelets within the prolonged depolarization period (Eccles et al., 1966). Although the fundamental properties of SSs are determined intrinsically, synaptic inputs driven by sensory-induced afferent activities can also affect the ultimate firing characteristics of SSs in PCs. Non-invasive extracellular recordings of SSs in PCs have been performed in many laboratories both *in vitro* and *in vivo*, and revealed that PCs fire regularly with high frequency: 20-50 Hz regular SSs *in vitro* and 40-150 Hz both regular and irregular SSs *in vivo* (Bell and Grimm, 1969; Latham and Paul, 1971; Hounsgaard, 1979). Irregular firing spikes of PCs are often detected *in vivo* as synaptic inputs from CFs, PFs (glutamatergic) as well as MLIs (GABAergic) affect the firing rate of PCs in the intact cerebellar network (Granit and Phillips, 1956; Häusser and Clark, 1997). Some PCs display a complex pattern of SS activity the so called trimodal firing, which includes a tonic firing phase followed by a silent period and a rhythmical bursting phase. In these PCs, the behavior of the spontaneous spikes is changed from a regular firing mode to one that switches continuously among the tonic firing, bursting and silent mode. The trimodal firing may repeat for hours, but it can be different from one cell to the next (Womack and Khodakhah, 2002). These firing behaviors are shaped by the intrinsic membrane properties and dysfunction of ion channels results in signaling deficits in PCs, which are reported in ataxia-related studies described in the next chapter in detail.

1.3.3 Input and output at Purkinje cell synapses

The extensive dendritic arbors of PCs allow them to integrate their vast and complex synaptic inputs. Sensory information from the inferior olive, brain stem and spinal cord

enter the cerebellum via two major afferent fibers: the mossy fibers (MFs) and the CFs (Fig. 1.3).

The MFs form synapses on GCs which project their axons toward the pial surface of the ML and bifurcate in a "T" shape becoming PFs. The MF-GC-PF pathway relays excitatory input to the PCs and facilitates PC activity. It was reported that PFs extend around 3 mm forming about 300 synapses onto PC dendrites in the rat cerebellum (Palay and Chan-Palay, 1974; Arata and Ito, 2004; Ito, 2006). In the CNS, GCs are the most abundant neurons and the rat cerebellum holds approximately 10^7 GCs (Harvey and Napper, 1988). Thus, a single MF transmits its excitatory signals to around 500 GCs and 150,000 PCs (Ito, 1984; Ito, 2006). In each PC the PFs cover approximately 30% of the distal dendrites close to the pial surface of the ML in the mouse cerebellum and thereby a PC receives input signals from around 100,000 PFs (Harvey and Napper, 1988; Ichikawa et al., 2015).

After maturation of the cerebellum, each PC forms a contact with a single CF coming from the inferior olive, located in the medulla oblongata, which forms about 200 CF-PC synapses spaced at 2-3 μm intervals. Each CF bifurcates to 5-10 PCs and travels along the PC dendrites from proximal to medial dendrites covering about 80% of the dendritic territory (Ichikawa et al., 2015). Large amounts of glutamate are being released at CF-PC synapses which are relatively larger than typical central nervous system synapses and cause the generation of CSs at 0.5-2 Hz and a large influx of Ca^{2+} in PC dendrites (Ross and Werman, 1987; Knöpfel et al., 1990). Hence, CF signals are important in conveying sensory information and motor error signals.

The concept of microzones in the cerebellum was suggested by Andersson and Oscarsson in 1978. It proposes that there is a functional module in the cerebellar circuit that are composed of 10-15 neighboring PCs receiving the same CF input. PCs are the sole output neurons in the cerebellar cortex and project to the DCN which is embedded in the WM in the paravermis. The DCN are composed of three parts: the fastigial nucleus, the interposed nucleus and the dentate nucleus. The DCN receive signals from both excitatory and inhibitory neurons: Both PF- and CF-fibers relay excitatory input to the DCN and project to an inhibitory loop in the cerebellar cortex that modulates the activity of the DCN, but inhibitory input from PC axons is dominant (70-80%) suggesting that PCs are the major modulator of the output of the cerebellum (De Zeeuw and Berrebi, 1995). The GABAergic inputs from PCs activate GABA-gated Cl^- channels in the DCN so that the

membrane permeability to Cl⁻ is increased thereby hyperpolarizing the DCN (Palkovits et al., 1977; De Zeeuw and Berrebi, 1995).

1.3.4 Cerebellar ataxia

Ataxia, "lack of order" in Greek, is a neurological disease whose symptoms include lack of coordination, abnormal gait, tremors, deterioration of fine motor skills, eye movement abnormalities, slurred speech and so on. Cerebellar ataxia is caused by dysfunction of the cerebellar cortex and is found in many patients with a damaged cerebellum (reviewed in Mariotti et al., 2005).

Different types of ataxias are known. Spinocerebellar ataxia (SCA) is a group of hereditary cerebellar ataxias with autosomal dominant inheritance, which is caused by progressive neurodegeneration of the cerebellar circuit. Production of toxic polyglutamine proteins by expansion of a CAG nucleotide repeat are found in many SCA cases: SCA1-3, SCA6-7, and SCA17. SCA-related mouse models were generated by genetic manipulations by either overexpressing SCA-associated transgenes or expressing transgenes for an expansion of the CAG-repeat. For instance, a mouse line of SCA pathogenesis generated by the conditional expressions of mutant ataxin 1 in PCs proved that continuous expressions of mutant ataxin 1 causes SCA1 (Paulson et al., 2017).

Sporadic bouts of ataxic phenotypes are typically found in episodic ataxia (EA), another group of dominantly inherited disorders. EA can be induced by stress, physical exertion or startle. According to many ataxia studies, disturbed firing of PCs is the most prominent phenotype found in EA, and several mutations have been identified in patients (EA type 1-6; reviewed in Hoxha et al., 2018). Type two episodic ataxia (EA2) is the most common and the best characterized form of EA until now. Symptoms of EA2 include migraine, body shaking, stuttering and increased heart rate that lasts for hours. Mutations in *CACNA1A*, a gene encoding the pore-forming and voltage-sensing α1A subunit of P/Q-type VGCCs (Ca$_v$2.1), are found in EA2 patients (Mori et al., 1991; Ophoff et al., 1996). In 1962, Green M. C. and Sidman R. L. generated *tottering* mice with a point mutation in the α1A subunit of Ca$_v$2.1 and observed episodes of motor impairment (Green and Sidman, 1962). *Tottering* mice not only exhibit episodic motor impairments occurring at least once per day, but also abnormal eye movements (Hoebeek et al., 2005; Stahl et al., 2006). Moreover, in *tottering* mice episodic attacks can be induced by stress, which is similar to EA2 patients,

and by intraperitoneal caffeine injections (Fureman et al., 2002). As the episodes of motor impairment can be reliably reproduced in the lab, *tottering* mice have been widely used as a model of EA2 to elucidate the Ca^{2+}-mediated physiological mechanism underlying the ataxic phenotype.

1.3.5 Signaling deficits in Purkinje cells in ataxia model

As mentioned earlier, PCs display distinct electrophysiological properties, such as a spontaneous firing at high frequency, processing of a large amounts of input information, and a group convergence of output to the DCN. Deficits in PC signaling have been frequently found in ataxia mouse models. It has been reported in multiple studies that alterations in intrinsic membrane properties via mutations in channels results in disturbed pace-making activities in PCs which in turn causes ataxic phenotypes. However, the linkage between specific alterations in the spontaneous firing activities of PCs and the corresponding motor coordination impairments remains still unclear. The following chapters introduce ataxia models with demonstrated signaling deficits in PCs due to mutations in specific ion channels.

1.3.5.1 Disturbed pace-making activity in Purkinje cells

The pace-making activity of PCs which spontaneously generates APs is primarily modulated by intrinsic membrane properties even though synaptic inputs can also shape the PC firing rate. Ionic currents via cell membrane determines the firing properties of PCs. Previous studies demonstrated that voltage-dependent Na^+ and K^+ currents are crucial for high frequency discharges of PCs (Raman and Bean, 1999).

In PCs, the large conductance voltage- and Ca^{2+}-dependent K^+ channels (BK channels) located in the soma and dendrites are important for mediating firing of PCs. The slow-gated K^+ currents generated by BK channels affect the conductance during the afterhyperpolarization period (Gruol et al., 1991; Womack et al., 2009; Benton et al., 2013). Mice lacking BK channels were generated and they developed impaired motor coordination including abnormal gait in the foot-printing test (Sausbier et al., 2004). In neurons, excitability of the membrane can be regulated by the small-conductance Ca^{2+}-activated K^+ channels (SK channels). In the mammalian brain, three subunits of SK channels (SK1-3) are found in the CNS and the SK2 channels are the only subunit

expressed in PCs (Köhler et al., 1996; Xia et al., 1998; Cingolani et al., 2002). Blocking SK channels in cerebellar slices with the selective blocker apamin suggested that SK channels regulated PC excitability without altering the waveform of APs (Stocker et al., 1999; Belmeguenai et al., 2010). Interestingly, SK channel activators, such as 1-ethyl-2-benzimidazolinone, have been used as therapeutic substances in *tottering* mice, improving their motor performances (Walter et al., 2006). Other therapeutic agents, such as acetazolamide, 4-aminopyridine, and chlorzoxazone, were also administrated and improved the regularity of the PC pace-making activity as well as EA2 symptoms in *tottering* mice (Glasauer et al., 2005; Strupp et al., 2004; Strupp et al., 2007; Alviña and KJhodakhah, 2010).

1.3.5.2 Voltage-gated calcium channels

Changes in the calcium concentration (calcium event) are an important and reliable indicator of neuronal activity and calcium imaging techniques both in slice and in mice have been developed and used to detect calcium events. In neurons, membrane depolarization triggers opening of VGCCs (Ca$_v$ channels) and Ca^{2+} influx into the cell. Among the Ca$_v$ channels (L-, N-, P.Q, and R-type), the P/Q-type VGCCs are most the abundant variant in PC dendrites and account for 90% of Ca^{2+} currents (Ross and Werman, 1987; Tank et al., 1988; Regan, 1991). The Ca$_v$2.1 channels in PCs are clustered with Ca^{2+}-dependent K$^+$ channels, BK and SK channels, and these clusters allow Ca^{2+} to directly activate the K$^+$ conductance (Womack et al., 2004). In ataxia studies, mutant Ca$_v$2.1 channels mice are widely used to investigate the physiological mechanisms underlying EA2. The *tottering* mice exhibit a by 40% reduced Ca$_v$2.1 current density and a disturbed pace-making activity of PCs *in vivo* during the ataxic attack (Wakamori et al., 1998; Tara et al., 2018). Not only stress triggers episodes similar to EA2 patients, but also caffeine induces attacks in *tottering* mice disturbing pace-making activity of PCs *in vivo* (Raike et al., 2012; Tara et al., 2018). *Leaner* mice have a spontaneous mutation in the *CACNA1* gene and *ducky* mice have a mutation in the *CACNA2D2* gene which encodes the α2δ2 auxiliary subunit of VGCCs (Tsuji and Meier, 1971; Barclay et al., 2001). Both the leaner and ducky mice develop episodes of motor impairment, and the calcium currents and spontaneous firing rate were reduced in PCs similar to the *tottering* mice (Donato et al., 2006; Walter et al., 2006).

1.3.5.3 Voltage-gated potassium channels

In the process of AP generation, the voltage-gated K^+ channels (K_v channels) are opened when the neuron is depolarized by changes in the N^+ conductance, which repolarizes and hyperpolarizes the membrane potential by efflux of K^+ via K_v channels. The high-threshold K_v channels, especially the K_v3 subfamily, are key regulators of this process in rapidly firing neurons (Rudy and McBrain, 2001). Four K_v3 subunits ($K_v3.1$-3.4) are found in the CNS, but the expression of the $K_v3.3$ channels is the strongest in PCs (Weiser et al., 1994; Boda et al., 2012). Mutations in the *KCNC3* gene, encoding the $K_v3.3$ channel, were found in SCA13 patients (Waters et al., 2006). Mice lacking $K_v3.3$ channels develop an ataxic phenotype showing poor performances in balance beam tests (Joho et al., 2006). In PCs, three sub-threshold K_v channels (K_v1, K_v4 and K_v11 channels) are expressed and modulate membrane excitability (Guasti et al., 2005; Khavandgar et al., 2005; Wang and Schreuers, 2006). Genetic analyses identified mutations I *KNCA1* gene, which encodes the $K_v1.1$ channel, in EA1 patients (Browne et al., 1994). Mice lacking the $K_v1.1$ channel also showed an impaired motor performance when tested on a stationary rod (Zhang et al., 1999). The K_v4 channels are the major source of subthreshold inactivating K+ currents in PCs and only $K_v4.3$ channels are expressed in PCs, found in the soma and dendrites (Serôdio and Rudy, 1998; Wang and Schreurs, 2006). Genetic screening of both SCA19 and SCA22 patients detected mutations in the *KCND3* gene, encoding the $K_v4.3$ channel (Duarri et al., 2012; Lee et al., 2012). Mice lacking the $K_v4.3$ channels were generated but no obvious phenotype was detected (Niwa et al., 2007).

1.3.5.4 Metabotropic glutamate receptors

Released glutamate at synapses activates not only the ionotropic glutamate receptors, such as AMPA, NMDA and 23mmune23 receptors, but also metabotropic glutamate receptors (mGluRs) which belong to the group C family of G-protein-coupled receptors. Eight subtypes (mGluR1-8) are present and they are categorized in three groups (Group I-III) based on their structure and physiological function (Pin and Duvoisin, 1995). The mGluR1 is highly expressed In the cerebellum, especially In PCs, and located outside of the postsynaptic density where it can be activated by spillover of glutamate from PFs (Batchelor et al., 1994). $G_{\alpha11}$ and G_q proteins coupled to the mGluR1 are involved in signaling cascades activating phospholipase C and generate slow excitatory postsynaptic

currents (EPSCs) mostly through the short transient receptor potential channel (TRPC) 3 (Hartmann and Konnerth, 2008). The *moonwalker* mice which carry a point mutation in the gene encoding TRPC3 showed an impaired dendritic arborization of PCs and mGluR1 gain-of-function (Becker et al., 2009). More importantly, mGluR1 mediates large Ca^{2+} transients in PC dendrites (Batchelor and Garthwaite, 1997). mGluR1 deficient mice develop ataxic phenotypes including abnormal gait as shown by foot-printing and rotarod, impaired conditioned-eyeblink responses, and deficits in spatial learning in the Morris tests (Aiba et al., 1994; Conquet et al., 1994).

1.4 Aim of the study

Many aspects of synaptic function are determined by the release machinery at the active zone which is composed of a large number of proteins including RIMs. The strength of individual synapses is an important factor in the transmission and computation of neuronal information and synaptic dysfunction is associated with neurological and cognitive disorders. It is by now well known that the large RIM isoforms, RIM1 and RIM2, are essential for synaptic vesicle docking and priming at the active zone, mediate presynaptic plasticity and determine the density of Ca^{2+} channels at the AZ. On the contrary, not much is known about the function of RIM4 in the central nervous system. Preliminary studies carried out by the Schoch/Dietrich lab found that RIM4-deficient mice developed an episodic motor impairment of their hindlimbs. However, so far the underlying mechanisms and responsible circuits are unresolved. Hence, the goal of this thesis was to gain novel insight into the function of RIM4 in the cerebellar network and the physiological changes caused by RIM4 deficiency that trigger the episodes of motor impairment. In detail, we will address the following aims:

The first aim Is to Investigate if the loss-of-function of RIM4 impacts the dendritic arborization of cerebellar Purkinje cells as data from knock-down experiments in cultured neurons and *in vivo* suggested a role for RIM4 in maintaining normal neuronal morphology.

The second aim is to characterize both intrinsic electrophysiological properties and the signaling deficits of Purkinje cells. In addition, Ca^{2+} signaling in Purkinje cells will be evaluated in slices as well as in *in vivo* in order to gain new insight into the potential mechanisms explaining the motor impairment in RIM4-deficient mice.

The third aim is to identify a novel function of RIM4 in the cerebellar circuit by screening the functions of several key ion channels or receptors modulating excitability in Purkinje cells.

Finally, the fourth aim is to show whether the alterations observed in RIM4-deficient mice can be rescued by expressing RIM4 into Purkinje cells of RIM4 KO mice at different time points. These experiments will show if the changes are indeed directly caused by the absence of RIM4.

In summary, the results of this thesis will provide an insight how RIM4 is crucial in the regulation of the morphology of Purkinje cells and a signaling in cerebellar circuit that might explain a motor phenotype in RIM4 lacking mice.

2. Material and Methods

2.1 Animals

All experimental procedures were planned and performed according to the guidelines of the University of Bonn Medical Centre Animal-Care-Committee approved by the European Directive (2010/63/EU) on the protection of animals. All efforts were made to minimize pain and to reduce the number of animals usage. Experimental mice were housed under a 12h light-dark-cycle (light-cycle 7 am/7 pm) with a maximum of 5 animals per cage in a specialized animal facility supplied food/water *ad libitum* and nesting material (nestlets, Ancare Corp., Bellmore, NY, USA). The environment of cages was set to a temperature at $22 \pm 2°C$ and humidity at $55 \pm 10\%$.

2.1.1 RIM4 knock-out mouse lines

We produced RIM4-null mice according to the previous study conducted by K. Michel (Dissertation, 2015). To produce the first knock-out (KO) line, we used the "KO first" strategy by using embryonic stem cells carrying the targeting vector against RIM4: a splice acceptor-lacZ trap cassette was inserted by germline transmission interrupting the endogenous RIM4 transcripts and resulting in creating a constitutive KO (Fig. 2.1). Next, mice carrying floxed-RIM4 genes (RIM4$^{flox/flox}$) were generated by crossing the first KO line with mice expressing a flippase recombinase-transgene which gave rise to excise the gene cassette. Finally, the constitutive RIM4 KO mice (RIM4 KO$_{const}$) were generated by crossing RIM4$^{flox/flox}$ mice with the transgenic mice expressing ubiquitous Cre-recombinase (B6.C-Tg(Pgk1-cre)1Lni/CrsJ; Lallemand et al., 1998). The offspring of RIM4 KO$_{const}$ mice followed mendelian distribution in their genotypes and all pups were viable. It was proved that the level of gene transcription and protein expression was abolished in the brain of RIM4 KO$_{const}$ mice (K.Michel, Dissertation, 2015). Following the animal-care guidelines, heterozygous mice (RIM4$^{wt/d}$; RIM4 was ablated only in one allele of their genes) were used for breeding and maintaining the constitutive RIM4 line. As a control group, we used mice fully expressing RIM4 proteins (RIM4$^{wt/wt}$; RIM4 WT$_{const}$) driven by the same breeding line.

In order to generate conditional RIM4 KO line specifically targeting PCs, RIM4$^{flox/flox}$ mice were crossed with the transgenic mice expressing Cre recombinase controlled by Purkinje

cell protein 2 (PCP2) promotor (B6.129-Tg(PCP2-cre)2Mpin/J; purchased from The Jackson Laboratory; Barski et al., 2000). In the conditional RIM4 KO mice (PCP2-Cre$^{wt/tg}$:RIM4$\gamma^{fl/fl}$, RIM4 KO$_{PCP2}$), as a result, expression of RIM4 proteins was abolished in PCs. Mice carrying RIM4 wild-type alleles and expressing PCP-Cre recombinase (PCP2-Cre$^{wt/tg}$:RIM4$^{wt/wt}$, RIM4 WT$_{PCP2}$) were used as a control group.
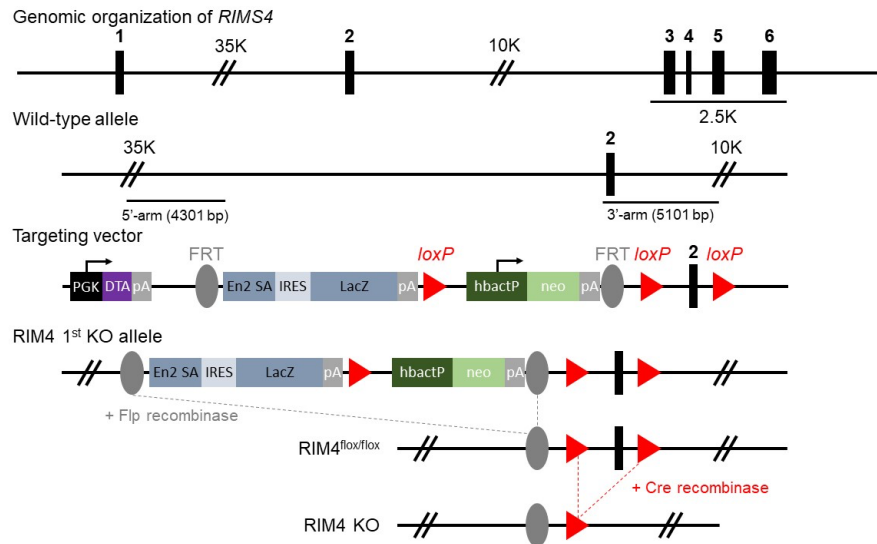
Figure 2.1. **Genetic strategy for generation of constitutive and conditional RIM4 KO mice**. Schematic description of RIM4 KO strategy. Wild-type produces fully functional RIM4 proteins containing all 6 exons. To generate the first RIM4 KO, the gene trap cassette was inserted via RIM4 targeting vector and this caused splicing of RIM4 interrupting protein expression. Crossing the first RIM4 KO mice with flippase (flp) recombinase expressing transgenic mice leaded to excision of the gene cassette and a generation of RIM4$^{flox/flox}$ mice. Finally, Cre-recombinase mediated recombination at the loxP sites around the exon 2 and resulted in ablation of RIM4 protein (ubiquitous Cre-recombinase, constitutive RIM4 KO; Purkinje cell-specific Cre-recombinase, conditional RIM4 KO). Adapted from dissertation of K. Michel (2015).

2.1.2 Preparation of acute cerebellar slices

Sagittal slices of cerebellar vermis were prepared acutely from both female and male mice of RIM4 KO$_{const}$ and RIM4 KO$_{PCP2}$ lines (Fig. 2.2). Prior to preparation, mice were deeply anesthetized with Isoflurane (Abbot, Chicago, IL, USA) and decapitated using a rodent guillotine (DCAPS, World Precision Instruments, Sarasota, FL, USA). The cerebellum was dissected out on a cooled surgical metal plate and immediately submerged in ice-cold modified artificial cerebrospinal fluid (mACSF) containing high sucrose at pH 7.4 (section 3.3.1). The cerebellum was glued with the cut face onto an agarose block (1.5 %, solid). One of the lateral hemispheres of the previously glued

cerebellum (1 mm) was cut parasagittally to make it flat. The flat part of glued cerebellum was placed into a vibratome plate and sectioned sagittally at 300 µm thickness (Leica VT 1200S, Leica Biosystems Nussloch GmbH, Wetzlar, Germany). Only the vermis slices were selected and incubated in a beaker filled with mACSF at pH7.4 in a water bath (WNB 22, Memmert GmbH and Co. KG, Schwabach, Germany) controlled at physiological temperature (36°C) for 30 minutes. Before experiments, slices were stored in standard artificial cerebrospinal fluid (sACSF) at room temperature (RT). All solutions were bubbled with 95% O_2 and 5% CO_2 in beakers at least 30 minutes before the usage, covered with parafilm (section 3.3.1). The cerebellar slice was placed on a poly-D-Lysine coated coverslip (0.1 mg/mL) to avoid any movement during the experiments. The coverslip with a slice was placed in the submerged chamber of a microscope (LSM5 Pascal, Zeiss, Oberkochen, Germany), which was perfused constantly with oxygenated sACSF (95% O_2, 5% CO_2) with a flow rate of 0.5-1.5 ml/min using a peristaltic pump at RT.
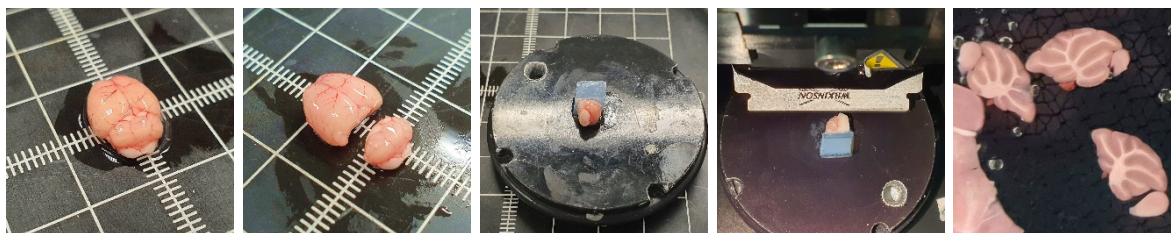
Figure 2.2: Procedure of acute cerebellar tissue. The steps of preparation of acute cerebellar slices were depicted: from left a whole mouse brain, dissected cerebellum, a vibratome plate with the glued cerebellum for sagittal slicing, and sagittal slices (300 µm).

2.2 Chemicals and reagents

Table 1. Used chemicals and reagents

Chemical	Target	Pharmacology	Concentration	Supplier
CNQX	AMPA/Kainate receptors	Competitive antagonist	TOCRIS	20 µM
Caffeine	Adenosine receptor	Antagonist	SIGMA	1 mM
D-APV	NMDA receptor	Competitive antagonist	TOCRIS	100 µM
(S)-3,5-DHPG	mGluR1 receptor	Selective agonist	TOCRIS	20 µM

Mefloquine	$K_v4.3$ channel	Antagonist	SIGMA	10 μM
QX-314 chloride	Na^+ channel	Blocker	TOCRIS	5 μM
SR 95531 hydrobromide (Gabazine)	$GABA_A$ receptor	Competitive antagonist	TOCRIS	10 μM
TTX	Na^+_v channel	Blocker	BIOTREND	1 μM

2.3 Solutions

2.3.1 Incubation/perfusion solutions: artificial cerebrospinal fluid

For acute slicing of cerebellar tissue, slices were stored in mACSF, containing (in mM): 87 NaCl, 2.5 KCl, 1.25 NaH_2PO_4, 7 $MgCl_2$, 0.5 $CaCl_2$, 25 $NaHCO_3$, 25 Glucose, and 75 Sucrose adjusted pH at 7.4 with 1 M NaOH or 1 M HCl. Once prepared, slices were stored in sACSF, containing (in mM): 124 NaCl, 3 KCl, 1.24 NaH_2PO_4, 2 $MgCl_2$, 2 $CaCl_2$, 26 $NaHCO_3$, and 10 Glucose adjusted pH at 7.35. During the experiments, sACSF was perfused constantly at 0.5-1.5 ml/min flow speed. All solutions were bubbled with 95% O_2 and 5% CO_2 in beakers at least 30 minutes before the usage, covered with parafilm. In order to prepare extracellular solutions containing higher Ca^{2+} concentration, sACSF was adjusted to contain 4 mM $CaCl_2$ and 0.5 mM $MgCl_2$. This solution was only used for recordings of evoked IPSCs in DCN.

2.3.2 Internal solutions for patch-clamp recordings

For whole cell patch-clamp recordings of PCs, the internal solution was used containing (in mM): 130 K-gluconate, 0.5 $MgCl_2$, 5 KCl, 4 NaCl, 4 Na_2ATP, and 10 HEPES adjusted pH at 7.3. In case of recordings to avoid sodium spikes, such as postsynaptic currents recordings, 5 μM QX-314 chloride was added into the internal solution. To measure the calcium currents, cesium-based internal solution was used containing (in mM): 130 Cs-MethaneSulfonate, 10 $CaCl_2$, 2 $MgCl_2$, 2 Na_2ATP, and 10 HEPES adjusted pH at 7.3.

For voltage clamp recordings of DCN, high chloride internal solution was used to achieve larger chloride driving force, containing (in mM): 90 K-gluconate, 0.5 $MgCl_2$, 45 KCl, 4 NaCl, 4 Na_2ATP, 10 HEPES, and 0.1 EGTA adjusted pH at 7.3. In order to block voltage-

gated sodium channels, 5 µM QX-314 chloride was also added before experiments. The reversal potential of Cl⁻ (-54.7 mV) was calculated as followed (Nernst equation):

$$V_{Eq.} = \frac{RT}{zF} \ln\left(\frac{[X]_{out}}{[X]_{in}}\right) \quad (1)$$

$$I_{ion} = g_{ion}(V_m - E_{ion}) \quad (2)$$

2.4 Adeno-associated viruses and stereotaxic injections

2.4.1 Adeno-associated viruses

Table 2. Used AAV constructs

Viral construct	Source or reference	Additional information
AAV1.CAG.GCaMP6f.WPRE.SV40	Penn Vector Core, Douglas Kim Lab	100836-AAV1
AAV2/1.CMV.mRFP	AG Schoch	custom
AAV2/1.CMV.mRFP.T2A.Flag.RIM4	AG Schoch	custom

2.4.2 Viral transduction of the adult cerebellum

All animals were transferred to the animal facility at least 2-3 days in advance for acclimatization. On the day of operation, mice were treated with analgesic (5 mg/kg ketoprofen s.c.) at least 30 minutes before. Mice were restrained with one hand with abdomen facing up and injected the anesthetic agents intraperitoneally through a needle inserted into the left or right lower abdominal quadrant: Fentanyl (0.05 mg/kg), Midazolam (5 mg/kg), and Medetomidin (0.5 mg/kg).

To express proteins of interest, I bilaterally injected AAV into adult RIM4 WT and KO mice in both constitutive and conditional lines (12-14 weeks old, both female and male; Fig. 2.3). In order to target the region of cerebellar vermis (Lobules IV, V, and VI), stereotaxic coordinates were set to 6.5, 1.2, and 0.8 mm (anterior-posterior, medio-lateral, dorso-ventral) relative to the Bregma.

When the mouse fell asleep completely, the surgical field was cleaned by shaving hairs with scissors or razor and disinfections of skins. During the entire surgery, mouse eyes were covered with lubricant ointment (Bephanthen, Bayer AG, Leverkusen, Germany) to prevent corneal drying. When foot withdraw reflex was absent, mouse was positioned in

the stereotaxic frame (World Precision Instruments Inc., Sarsota County, FL, USA) and incision was made about 1 cm along the midline of skull to reveal surgical area. After probing injection points, small holes were drilled in each site and the injection needle (NanoFil 33G, World Precision Instruments Inc., Sarsota County, FL, USA) was positioned carefully. Following 2 minutes of waiting time, in each site, 0.5 µl of virus (stock titer: 1×10^{13} vg/ml) was injected with an injection rate of 0.2 µl/minutes. Once the injection was completed, the needle was slowly retreated after 2 minutes of waiting time. The incision was sutured with dissolvable surgical thread, and the mouse was put on a warming pad for recovery. One hour after the induction of the anesthesia, the mouse was treated with antagonistic anesthetics i.p.: Naloxon (1.2 mg/kg), Flumazenil (0.5 mg/kg), and Atipamezol (2.5 mg/kg). The mouse was then put back to its home cage onto a pulp sheet and left the cage on a warming pad until the mouse was fully awake. The mouse was treated with analgesics once per day with Ketoprofen (5 mg/kg, s.c.) for 3 consecutive days after the surgery. In case the mouse had a weak and slow recovery phase, glucose (0.5 ml, 0.5 %, s.c.) and antibiotics (5 mg/kg Bytril, s.c.) were treated and documented in the operation-score sheets.
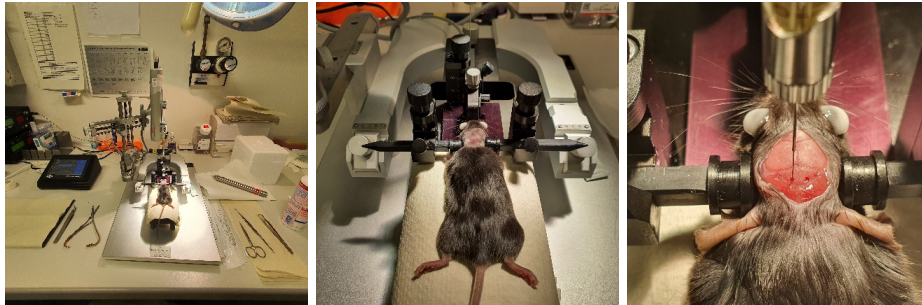
Figure 2.3: **Procedure of stereotaxic injections in adult mouse**. From left stereotaxic apparatus equipped with syringe pump and surgical tools, mouse fixed in the stereotaxic frame, and bilateral AAV injections with NanoFil syringe (33 G).

2.4.3 Viral transduction of the neonatal cerebellum

On the day of birth, the pups from the breeding pairs of constitutive RIM4^wt/d mice were bilaterally injected with AAV2/1.CMV.mRFP or AAV2/1.CMV.mRFP.T2A.Flag.RIM4 (Fig. 2.4). Analgesic (a drop of Metamizol) was orally administrated into pups before the injections. Pups were moved to ice for 2 minutes until they were immobile. Following the slight anesthesia, pups were injected with 1 µl of virus (at 2 injection sites over the cerebellum, 0.5 µl per site, 0.2 µl/second flow rate). All pups were kept on the heating pad

separated from their parents during the entire injections period. When injections were completed and pups were mobile again, they were placed back to the home cage.
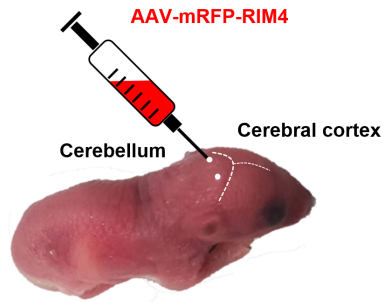
Figure 2.4: **AAV-injections into the cerebellum at 0 postnatal day**. After a newborn pup was anesthetized on ice for couple of minutes, 1 µl of AAV (0.5 µl per site at 0.2 µl/second flow rate) was delivered at two sites (white dots) in the cerebellum by hand-held injection needles.

2.5 Morphology analysis

2.5.1 Cerebellar morphology analysis

Parasagittal slices of RIM4 WT_{const}, KO_{const} and RIM4 WT_{PCP2}, KO_{PCP2} mice (15-20 weeks old, including both genders) were prepared and stained with Nissl green or Bisbenzimide (Hoechst 33342) fluorescence which reveals soma of neuronal cells and with calbindin which is exclusively expressed in PCs. For calbindin staining, primary antibody (rabbit anti-calbindin D28-K; 1:1000; Swant CB38-a) was treated overnight at 4°C and on the following day secondary antibody (Alexa 647 goat anti-rabbit; 1:500) was treated at 4°C for 4 hours. The stained cerebellar vermis slices were imaged with a Nikon Inverted microscope (20X, 0.5 N.A. Objective; Nikon, Tokyo, Japan) or with a laser-scanning confocal microscope (40X, 1.2 N.A. Objective; Nikon A1Plus, Tokyo, Japan). For confocal scanning, the pinhole was set to 13.5 µm and both gain and offset of PMT was adjusted to optimize images. At the selected field of view over the lobule V and VI, Z-stacks were acquired with a step size of 1 µm (three stacks per slice, 3 slices per animal).

For measurements of brain area, outlines of each region of interests were drawn manually using a software, Image J (NIH, MD, USA), and each area was measured based on the outlines: whole CB, ML, GCL, and WM.

Using calbindin stained cerebellar vermis, the number of PCs were counted along the PCL located in lobules V and VI. The density of PCs (the number of PCs/µm PCL) was calculated by dividing the counted number of PCs by the length of measured PCL. To

measure the thickness of ML, the length of straight lines perpendicular to the PCL in lobules V and VI was measured in calbindin expressing red channels by using an ImageJ.

2.5.2 Dendritic arborization of Purkinje cells

I*n vitro* single cell electroporation allowed us to label individual PCs in acute cerebellar slices using glass electrodes (0.86x1.50x80mm; electrode resistance, 5-6 MΩ) filled with 10 µl of internal solution containing red fluorescent dyes, Tetramethylrhodamine (TMR)-dextran (1 mM; 3000 MW). The electrode was placed close to the cell body of PC (<1 µm) under visual control using differential interference contrast (DIC) channel of a microscope (63x objective, 1.3 NA). For single cell electroporation, several trains of 10 positive voltage pulses spaced at 5 Hz were generated by a manually triggered stimulator (Model 2100, A-M systems, Sequim, WA, USA). The application of short voltage pulses led to permeability of the cell membrane so that the charged dyes could diffuse.

Z-stacks of the TMR-dextran-labelled PCs were imaged with a step size of 0.3-0.5 µm using a laser-scanning confocal microscope (40x Objective, 0.9 NA; LSM5 Pascal, Zeiss, Oberkochen, Germany). Prior to imaging, the pinhole size of the confocal microscope was set to 25.5 µm to resolve fine structures of the PC dendritic tree. The imaged PCs were reconstructed in three-dimensions (3D) by tracing dendrites based on the Z-stack images with a semi-automatic method using a software, Imaris (9.0, Bitplane, Oxford Instruments, Abingdon, UK). Dendritic arborization was evaluated by parameters measured from reconstructed PCs in 3D: the number of Sholl intersections, dendrite area, number of dendrite segments, total dendrite length. The number of sholl intersections was measured in reconstructed PCs from incremental homocentric spheres with 1 µm interval. The sum of the surface area in reconstructed PCs was defined as the dendrite surface area. To investigate the complexity of dendrites in detail, branch levels were calculated in each dendrite segment according to the algorithm in Imaris 9.0 software as followed: The initial branch from the soma was set to branch level 1. At each branching point, the branch level of following dendrite was set to next level if the mean diameter of the dendrite was smaller than other branches, whereas the dendrite with the greater or same diameter maintained on the same branch level. In case two dendrites have the same diameter, the dendrite with a greater branching angle was assigned to the next branch level while the dendrite with a smaller branching angle stayed at the same branch level.

2.5.3 Distribution of CF- and PF-PC synapses

To label CF- and PF-PC synapses, sagittal cerebellar tissue of RIM4 WT$_{PCP2}$ and KO$_{PCP2}$ mice was treated with antibodies: primary antibody, VGLUT1 polyclonal guinea pig antibody (1:500, Cat. No. 135 304, Synaptic System, Göttingen, Germany), Vglut2 polyclonal chicken purified antibody (1:500, Cat. No. 135 416, Synaptic System, Göttingen, Germany), rabbit anti-calbindin D-28k (1:1000, Cat. No. C B-38a, Swant, Burgdorf, Switzerland); secondary antibody, goat anti-chicken IgY antibody Alexa Fluor™ 488 (1:500, Cat. No. A-11039, Thermo Fisher Scientific, Waltham, MA, USA), goat anti-guinea pig IgG antibody Alexa Fluor™ 568 (1:500, Cat. No. A-11075, Thermo Fisher Scientific, Waltham, MA, USA), goat anti-rabbit IgG antibody Alexa Fluor™ 647 (1:1000, Cat. No. A-21245, Thermo Fisher Scientific, Waltham, MA, USA). Intensity line profile was measured by placing lines with 50 µm width perpendicular to PCL and the mean intensity within each line was plotted against the distance from the PC soma.

2.6 Analysis of spontaneous firing spikes of Purkinje cells

PCs fire APs spontaneously even in the absence of synaptic input, controlled by intrinsic ion channels (Häusser and Clark, 1997). Therefore, understanding of spontaneous spikes of PCs is one of key hallmarks to investigate electrophysiological properties in PCs. It is accessible in acute cerebellar slices to record spontaneous spikes extracellularly by placing recording electrodes around the axon hillock of PCs where APs are generated and by amplifying its signals. Even though it can be recorded from two or more neighboring PCs, spontaneous spikes from single PC are distinguishable in that the higher amplitude of spikes is, the closer PC is located.

2.6.1 Electrophysiology setup

The sagittal cerebellar slices were placed in the submerged chamber of a microscope (LSM5 Pascal, Zeiss, Oberkochen, Germany), which was perfused constantly with oxygenated sACSF (95% O_2, 5% CO_2) containing synaptic blockers, 20 µM CNQX and 10 µM Gabazine, with a flow rate of 0.5-1.5 ml/min using a peristaltic pump at RT. PCs located in cerebellar vermis (Lobule V-VIII) were visualized using 63x water immersion objective (1.3 NA). Recording electrode mounted on a headstage (ELC-01X, NPI electronic GmbH, Tamm, Germany) was filled with sACSF and placed close to the axon

hillock of PC soma, constantly monitored with an oscilloscope (Hameg HM507, Mainhausen, Germany). For recoding electrodes, glass capillaries with 1 mm thickness of the opening tip (GB150F-8P, Science Products, Hofheim, Germany) were prepared using a vertical puller (PP-830, Narishige, Setagaya, Tokyo, Japan). Signals were amplified with a pre-amplifier (EXT-02F/2, npi electronic GmbH, Tamm, Germany) and a post-amplifier (BF-48DGX, npi electronic GmbG, Tamm, Germany), filtered at 10 kHz, digitized (1440A digitizer, Molecular Devices, Canada) with a sampling rate of 20 kHz, and acquired using WinWCP software (University of Strathclyde Glasgow, UK).
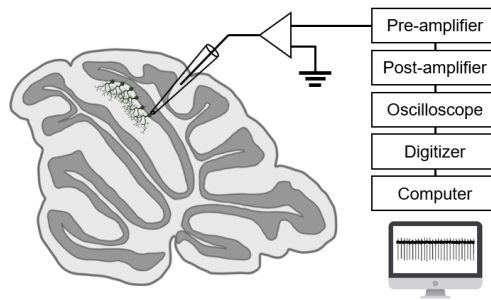

Figure 2.5: **Extracellular recording setup**. A schematic description of the extracellular recording setup. Spontaneous spikes of PCs were recorded using glass electrode placed around axon hillock. Signals were amplified and digitized to display the spikes in the computer.

2.6.2 Experimental procedure

Spontaneous spikes of PCs were recorded in RIM4 WT_{const}, KO_{const} (over 25 weeks old, both genders) and RIM4 WT_{PCP2}, KO_{PCP2} mice (6-8 weeks old, both genders) blinded to their genotypes during the experiments. In order to investigate intrinsic firing properties, both excitatory and inhibitory synaptic inputs were blocked by using 20 µM CNQX and 10 µM Gabazine respectively. Healthy PCs located at cerebellar lobule V-VIII were selected and recorded for 5 minutes. The acquired data was analyzed using a customized tool in Igor Pro (WaveMetrics Inc., OR, USA). For the detection of spikes, a threshold was set in each recording considering its signal-to-noise ratio: the rising phase of the first spike crossing a horizontal line (threshold) was detected and further spikes matching the first derivative were detected. When spikes with multiple-level amplitude were recorded, the threshold was set containing only spikes population with a larger amplitude. PCs with run-down spikes were discarded. To evaluate firing properties, I measured mean firing rate (Hz), inter-spike intervals (ISIs), and calculated coefficient of variation of ISIs (CV_{ISI}, the ratio of the standard deviation to the mean of ISIs).

To investigate the effect of caffeine on spontaneous spikes of PCs, I applied caffeine (1/3/10/20 mM) dissolved in sACSF for 10 minutes. To measure the effect on firing rate, mean firing rate of the last one-minute duration of caffeine application was normalized to mean firing rate of the baseline (5 minutes). To characterize firing behavior, additionally, auto-correlograms were generated by plotting the spike autocorrelation versus the time lags.

For the analysis of mGluR1-dependent signaling, I applied a selective group I mGluR agonist, (S)-3,5-Dihydroxyphenylglycine (DHPG), while recording spontaneous spikes in PCs as described above. After 5 minutes of baseline recording, 20 µM DHPG was applied for 6-10 minutes. To measure the effect of DHPG on spontaneous spikes, I calculated the mean firing rate and CV_{ISI} every minute, and the firing rate was normalized to the mean firing rate of the baseline. To characterize bursting behavior, auto-correlograms as well as histograms of ISIs were generated.

2.7 Whole-cell patch-clamp recordings

2.7.1 Electrophysiology setup

The sagittal cerebellar slices (200-300 µm thickness) were placed in the submerged chamber of a microscope (LSM5 Pascal, Zeiss, Oberkochen, Germany). The oxygenated sACSF (95% O_2, 5% CO_2) was perfused constantly in the chamber with a flow rate of 0.5-1 ml/min using a peristaltic pump at RT. PCs located in cerebellar vermis (Lobules V and VI) or DCN were visualized using 63x water immersion objective (1.3 NA) in DIC channel. Recording electrode mounted on a headstage (ELC-01X, NPI electronic GmbH, Tamm, Germany) was filled with internal solutions. Signals were amplified with a pre-amplifier (EXT-02F/2, npi electronic GmbH, Tamm, Germany) and a post-amplifier (BF-48DGX, npi electronic GmbG, Tamm, Germany), filtered at 3 kHz, constantly monitored with an oscilloscope (Hameg HM507, Mainhausen, Germany), digitized (1440A digitizer, Molecular Devices, Canada) with a sampling rate of 10 kHz, and acquired using WinWCP software (University of Strathclyde Glasgow, UK). An isolated pulse stimulator (Model 2100, A-M SYSTEM, Sequim, WA, USA) was installed to deliver electrical stimulation to stimulating electrodes (pulled glass pipette with resistance of 0.5-2 MΩ).
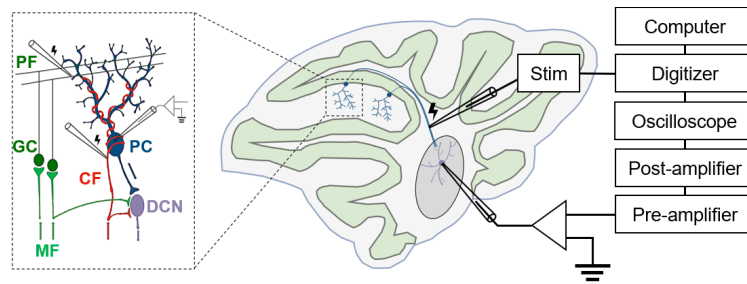
Figure 2.6: **Whole-cell patch-clamp recording setup**. A schematic description of the whole-cell patch-clamp recordings setup. An isolated pulse stimulator (Stim) was installed to evoke synaptic input-dependent responses. PC: Purkinje cell, DCN: Deep Cerebellar Nuclei, CF: Climbing fiber, MF: Mossy fiber, GC: Granule cell, PF: Parallel fiber.

2.7.2 Experimental procedure

Whole-cell patch-clamp recordings were performed in PCs of RIM4 WT_{const} and KO_{const} mice (4-6 weeks old, both genders) as well as in DCN of RIM4 WT_{PCP2} and KO_{PCP2} mice (4-6 weeks old, both genders). Under visual control in DIC, the recording electrode was approached to the cell body and achieved tight seal between electrode and cell membrane (larger than 1 GΩ). By applying negative pressure, the cell membrane was ruptured and a low access resistance (R_a) was formed in recording electrode. During all experiments, the R_a was frequently monitored and the cells with a higher R_a value (> 20 MΩ) were discarded.

For the analysis of intrinsic membrane properties of PCs, spontaneous APs were recorded in current-clamp mode by holding the cells at resting membrane potential (-60 mV). The waveform of 10 APs in each cell was characterized by measuring the peak amplitude (mV), the amplitude of fast afterhyperpolarization (fAHP; mV), and the full width (ms) from the onset of each AP. To test whether the blocking of $K_v4.3$ channels altered the waveform of APs in PCs, I performed whole-cell current-clamp in RIM4 WT_{PCP2} and KO_{PCP2} mice while applying 50 µM Mefloquine which is known as a potassium channel blocker. To avoid spontaneous spikes, PCs were clamped at -70 mV and evoked APs were recorded by injection of short currents (-150 to 200 pA) every 30 second. After 5-10 minutes of baseline recording, 50 µM Mefloquine was applied for 10 minutes. To evaluate the protocol, run-down tests were performed for 15-20 minutes without applying Mefloquine but changing the bottles containing the same sACSF. The full width of the first and randomly selected 5 APs was measured in each recording. The effect of Mefloquine was calculated by normalizing the mean value to that of the baseline.

To characterize the properties of CSs induced by CF inputs, whole-cell current-clamp or voltage-clamp was performed in PCs holding at -70 mV. CSs were evoked by electrical stimulation (5-10 V) via stimulating electrodes located around soma or proximal dendrites where CFs are located. CSs were "all-or-none" way showing a stereotypical waveform composed of rapidly rising initial Na$^+$ spike with several spikelets in prolonged depolarization period. In some PCs, antidromic APs were detected due to the electrical stimulus reached also at PCs but those were neglected for the analysis of CSs. To analyze the waveform of CSs, the peak amplitude of the initial spike (mV), the number of spikelets, and the length of prolonged depolarization duration (Coast-Line Index). Similar to the amplitude of AP, the peak amplitude of the initial spike was measured from its onset. The number of spikelets was counted when the spikes showed an increase greater than 5 mV after the initial Na$^+$ spike. The Coast-Line Index was measured in 15 ms duration from the onset of the initial peak containing the rest of spikelets. In voltage-clamp recording, I evaluated not only the magnitude of CF-evoked EPSCs, but also release probability of glutamate from CF by calculating paired-pulse ratio (PPR). Paired-pulse stimuli separated by 50 ms of inter-stimulus interval were applied to the stimulating electrode. PPR was calculated from the average peak amplitude of the first and the second responses in 5-10 successive recordings as followed:

$$\text{PPR (\%)} = \left(\frac{\text{eIPSC}_2}{\text{eIPSC}_1}\right) \times 100 \quad (3)$$

To measure calcium currents, whole-cell voltage-clamp recordings were performed in PCs of RIM4 WT$_{const}$ and KO$_{const}$ mice (4-6 weeks old) holding at resting membrane potential (-60 mV). To block Na$^+$ and K$^+$ channels, and both glutamate receptors (NMDA and AMPA), specific blockers, 1 µM TTX, 1 mM TEA and 100 µM 4AP, 50 µM APV, and 20 µM CNQX respectively, are added to the sACSF during the experiments. After five minutes of waiting time for diffusion of the cesium-based internal solution (see 2.3.2), a brief voltage-pulse in 200 ms duration was applied via recording pipette and depolarized the cell from -60 mV to -10 mV. The average peak current was measured from 3-5 recordings per cell. At the same time, time-series imaging (10-12 s) was performed using a laser-scanning confocal microscope (LSM5 Pascal, Zeiss, Oberkochen, Germany) visualizing PCs soma and dendrites and the average calcium transient was calculated depending on the dendritic branch levels. The amplitude of calcium transients (ΔF/F) in each region of interest was computed as $(F - F_b)/F_b$, where F is the average fluorescence

intensity at the peak of the transient and F_b is that at the baseline which was defined as 1 s duration before the onset of event.

Whole-cell voltage-clamp recordings were performed in DCN of RIM4 WT$_{PCP2}$ and KO$_{PCP2}$ mice (4-6 weeks old) to characterize the synaptic transmission of GABA at PC-DCN synapse. Glutamatergic DCN (> 20 µm somatic diameter; Batini et al., 1992) located at WM in the cerebellum were primarily selected. After the whole-cell configuration was achieved, cells were held at -80 mV using recording electrodes containing high Cl$^-$ internal solution (see 2.3.2) with 5 µM QX-314 to block voltage-gated sodium channels. To isolate IPSCs in DCN, 20 µM CNQX and 100 µM APV were included in the bath sACSF. The spontaneous inhibitory postsynaptic currents (sIPSCs) were recorded in DCN for 2-3 min and analyzed using a template-matching method in AxoGraph (https://axograph.com/). To evaluate the properties of GABA release, the amplitude, the frequency, and the kinetics including rise (20-80%) and decay time (tau) of sIPSCs were measured. Evoked inhibitory postsynaptic currents (eIPSCs) were recorded in DCN by electrical stimulation of PCs axons located in the WM near the recorded DCN (100-300 µm distance from the soma). PPR in PC-DCN synapses was compared by using the same protocol described above. As another approach to access the short-term plasticity, I measured the magnitude of the facilitation of the peak amplitude in higher extracellular calcium concentration ([Ca^{2+}]$_e$). After 10 minutes of baseline recording in 2 mM [Ca^{2+}]$_e$, the sACSF was exchanged with the one containing 4 mM [Ca^{2+}]$_e$ while recording the eIPSCs in DCN as described above. The effect of facilitation in a higher [Ca^{2+}]$_e$ was calculated by normalizing the average peak amplitude to that of the baseline.

2.8 Rescue of RIM4 in Purkinje cells in RIM4 deficient mice

Sagittal slices of cerebellar vermis (300 µm thickness) were prepared from the AAV injected mice (see 2.4). The expression of viral constructs was evaluated by visualizing the expression of red fluorescence proteins, mRFP. PCs strongly expressing mRFP were selected and categorized into 4 experimental groups: WT, overexpression of RIM4 (OE), KO, and Rescue (Table 3).

Table 3. **Experimental groups of the rescue experiments**. The mice injected with either AAV-mRFP or AAV-mRFP-RIM4 were categorized into 4 experimental groups based on

the expression of mRFP in each animal: WT, OE, KO, and Rescue. Both OE and Rescue groups were collected only from AAV-mRFP-RIM4 mice.

Viral construct	WT	OE	KO	Rescue
AAV-mRFP	Positive	-	Positive	-
AAV-mRFP-RIM4	Negative	Positive	Negative	Positive

Selected individual PCs were labelled by whole-cell patch-clamp using electrode containing internal solution with an additional green fluorescent dye, 500 µM Alexa Fluor™ 488 (Thermo Fisher Scientific, Waltham, MA, USA). Once the dye was fully diffused along the dendritic arbors of PCs, the electrode was pulled out and the labelled PCs were imaged in Z-stack with 0.5 µm interval using a laser-scanning confocal microscope (LSM5 Pascal, Zeiss, Oberkochen, Germany). In order to resolve the fine structures of PCs, the pinhole of microscope was set to 12.9 µm. The dendritic arborization of PCs were characterized by measuring dendritic tree area, maximum length, and full width at half maximum of tree in maximum intensity projection (MIP). The dendritic tree area was measured by tracing its outline using ImageJ software.

The analysis of spontaneous firing rate of PCs and application of caffeine and DHPG effects on spiking were performed in AAV-mRFP or AAV-mRFP-RIM4 injected mice as described in section 2.6.2. The genotypes of all used animals were revealed after the analysis.

2.9 Calcium imaging

It has been shown that CF signals arrived at PCs generate dendritic Ca^{2+} spikes and result in large influx of Ca^{2+} throughout the dendritic tree of PCs (Konnerth et al., 1992). To characterize calcium dynamics, I performed *in vivo* calcium imaging in PCs of RIM4 KO mice using one of the widely used genetically encoded calcium indicators (GCaMP6f; Nakai et al., 2001; Chen et al., 2013). I injected adult constitutive RIM4 mice (12-13 weeks old) with AAV-GCaMP6f and performed experiments two to three weeks after the injections (see 2.4.2). For further investigation on calcium transient and VGCCs in PCs, I performed *in vitro* experiments in PCs to measure CF-evoked EPSCs, CF-evoked postsynaptic calcium transient, and voltage-gated calcium currents.

2.9.1 Implantation of a cranial window

Thirty minutes prior to operation, a mouse was administered Burprenorphine (0.5 mg/kg) for analgesia and Dexamethason (0.2 mg/kg) to reduce inflammation subcutaneously. For anesthesia, a mouse was placed into a chamber containing 3-4% of Isoflurane (Abbot, Chicago, IL, USA). After slight anesthesia was achieved, a mouse was moved to a stereotaxic frame equipped with a gas mask providing a constant flow of 1-2% Isoflurane diluted in mixture of 95% oxygen and 5% CO_2, depending on the weight of the mouse (Fig. 2.7). A mouse was tightly fixed in the frame using a nose clamp and non-rupture ear bars. A surgical area was disinfected with 70% Ethanol and shaved with an electrical razor. Upon absence of toe-pinch reflex, the skin over the region of interest was removed with surgical scissors. Periosteum on the exposed area was scraped off with a scalpel, and the skull was swiped with a cotton swab or GELITA-SPON® (GELITA, Eberbach, Germany) soaked in PBS to remove any remnants of connective tissue. Craniotomy (4-5 mm in diameter) was performed approximately 2.5 mm posterior to lambda over cerebellar lobules V and VI using a drill (Ideal Micro-Drill™, CellPoint Scientific Inc., Gaithersburg, MD, USA). Kwik-sil (World Prevision Instruments Inc, Sarasota, FL, USA) was applied over the exposed brain surface, which was then covered with a round glass cover slip 5 mm in diameter. After the skull was dry, a custom-made head-mount was fixed on the skull with light-curable dental cement (Tetric EvoFlow Bulk Fill IVA) using UV-lamp (intensity 2300 mw/cm^2; Woodpecker iLED Curing Light, Woodpecker, China). Slow and steady breathing as a sign of a stable anesthesia was regularly monitored during the entire procedure.

Figure 2.7: **Procedure of implantation of a cranial window in the cerebellum**. Left: For surgery, a mouse was fixed in a stereotaxic frame equipped with an Isoflurane-flow gas mask. Middle: Craniotomy was performed over the cerebellum and covered with a round 5 mm cover glass. Right: A head-mount was attached to the skull.

2.9.2 *In vivo* calcium imaging in a head-fixed anesthetized mouse

After implantation of cranial window, a mouse was moved to the recording chamber equipped with a gas mask providing a constant flow of 1-2% Isoflurane diluted in mixture of 95% oxygen and 5% CO_2. A temperature-controlled heating blanket with a thermistor (Homeothermic Blanket, Harvard Apparatus™, Holliston, MA, USA) was placed on the recording chamber and set to 37°C to maintain mouse body temperature. The recording chamber was placed on the two-photon laser-scanning microscope (A1R MP, Nikon, Tokyo, Japan) with a water-immersion 25X objective lens (1.1 N.A., working distance 2 mm; CFI Apo LWD, Nikon, Tokyo, Japan). GCaMP6f was excited by a mode-locked Ti:Sapphire Laser (Chameleon Vision II, Coherent, Santa Clara, USA) tuned at 950 nm wavelength and detected in the green channel (520-550 nm bandpass filter). Laser power was used up to 200 mW to image GCaMP6f in dendrites as well as in soma of PCs. The level of non-descanned photo multipliers (PMT), image acquisition, and positioning of field of view (61.4 µm x 61.4 m) were controlled by Nikon Element software (Nikon, Tokyo, Japan). Dendrites or soma of PCs located at cerebellar vermis (lobules IV-VI) were imaged with bidirectional rapid scan in Galvano or Resonant mode respectively. All data were collected as time-series at high spatial resolution (512 X 512 pixels) with a sampling rate of 100.5 or 133.5 ms/frame, or line scans at 1-2 ms/line.
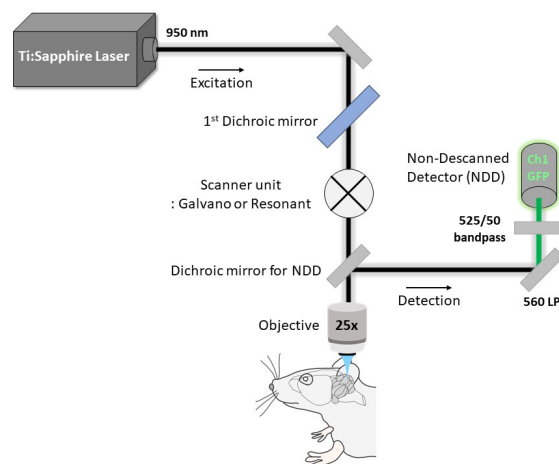

Figure 2.8: **Experimental setup of *in vivo* spontaneous calcium imaging in a head-fixed anesthetized mouse**. GCaMP6f in a head-fixed mouse was excited by two-photon laser tuned at 950 nm and emitted via 525/50 bandpass filter.

2.9.3 Analysis of spontaneous *in vivo* calcium events in Purkinje cells

For the analysis, at first, brain movement during the recording was corrected by eliminating nonrigid motion artifacts as described previously (Giovannucci et al., 2019). Motion vectors at subpixel resolution were estimated by sets of overlapping dendritic structures within the field of view in each frame. Within a field of view in acquired scans, each dendrite or soma was selected based on its anatomical structure. Average fluorescence intensity was extracted from the selected regions of interests in time-series images recorded for 2-3 minutes. Detection of spontaneous calcium events was performed using a 1st-derivative-based algorithm written in Matlab (MathWorks, Natick, MA, USA). For the global analysis of spontaneous calcium events in PC dendrites, the average amplitudes and inter-event intervals (IEIs) were measured. The amplitude of calcium transients ($\Delta F/F$) in dendrites was computed as $(F - F_b)/F_b$, where F is the average fluorescence intensity at the peak of the transient and F_b is that at the baseline which was defined as 0.5 s duration before the onset of detected events. The IEIs were calculated from the onsets of neighboring events.

To measure the synchronicity of spontaneous calcium events in neighboring PCs within the same field of view, the cross-correlation coefficient between two event traces at zero lag time was calculated based on the Pearson correlation using binarized event traces (where the event occurred was 1 and the others were 0), x and y, to avoid contamination by residual fluorescence in the cellular structure and noise:

$$Pearson's\ r = \frac{\sum(x_i-\bar{x})(y_i-\bar{y})}{\sqrt{\sum(x_i-\bar{x})^2\sum(y_i-\bar{y})^2}} \quad (4)$$

Mediolateral distances between dendrites were measured from the centroids of each dendrite within the field of view.

2.9.4 Analysis of evoked *in vitro* postsynaptic calcium transient in Purkinje cells

To measure the postsynaptic calcium transient in slice, acute cerebellar tissue of 4-6 weeks old RIM4 WT_{cosnt} and KO_{cosnt} mice were used (see 2.1.2). PCs located in vermis lobules V and VI were labeled with a calcium indicator, 200 µM Oregon green™ 488 bapta-1 (Thermo Fisher Scientific, Waltham, MA, USA). To trigger synaptic input, CFs were electrically stimulated as described previously (see 2.7.2). To verify mono-innervation of CF onto the PC, the input-output was analyzed by increasing the stimulation intensity from

0 to 60 V which was normalized to the threshold value. Multiple stimuli spaced at 300 ms were applied to CFs to evoke postsynaptic calcium bursts and the amplitude was measured as described previously (see 2.9.2).

4.5 Statistical analysis

All data in results were depicted as mean ± standard error of the mean. Statistical significance was tested using a software Igor Pro and differences were accepted at p-value < 0.05.

3. Results

In contrast to the large RIMs which are known as one of the central organizers in the AZ (Kaeser and Südhof, 2005; Südhof, 2012) the function of the small RIM isoforms has not been resolved yet. As a first step to investigate the function of RIM4 in the central nervous system, we generated RIM4 KO$_{const}$ mice (see 2.1.1; K. Michel, Dissertation, 2015). Interestingly, constitutive RIM4 deficient mice develop a strong episodic impairment, which in particular affects motor coordination of their hindlimbs. These episodes arise more than once per a day and each episode lasts on average 4 hours (K. Michel, Dissertation, 2015). It is well established since the 19th century that the cerebellum is involved in motor control and its damage causes impaired motor coordination also known as ataxia. Therefore, given the observation that RIM4 deficient mice exhibit an impaired motor coordination I here investigated the role of RIM4 in the cerebellar network.

3.1 RIM4 KO$_{const}$ mice show dysmorphic alterations in the cerebellum

Previous studies of RIM4 function in cultured neurons revealed alterations in dendritic arborization in the absence of RIM4 (Alvarez-Baron, Michel et al., 2013). Furthermore, it was shown that RIM4 is strongly expressed in the cerebellum (Alvarez-Baron, Michel et al., 2013) leading to the hypothesis that RIM4-deficient mice may show an altered morphology of the cerebellum.

3.1.1 Cerebellar area is reduced in RIM4 KO$_{const}$ mice

To answer the question if the constitutive ablation of RIM4 in mice caused changes in neuronal morphology, especially in the cerebellum, I compared the size of the cerebellum between RIM4 WT$_{const}$ and KO$_{const}$ mice. To this end, sagittal cerebellar slices (50 µm; vermis) of RIM4 WT$_{const}$ and KO$_{const}$ mice (4 mice in each group; both genders; 15-20 weeks old) were stained with fluorescent Nissl green. The area was measured by outlining each region of interest: cortex (CX), hippocampus (HC), whole cerebellum (CB), ML, GCL, and white matter (WM). Whereas the size of the cerebral cortex and the hippocampus was unchanged, the overall size of the cerebellum was significantly reduced in RIM4 KO$_{const}$ mice without distinct alterations in its overall structure showing fully developed lobules (Fig. 3.1A-B). I further analyzed the cerebellar sublayers and found that the area

was strongly reduced only in the ML of RIM4 KO$_{const}$ mice while no alteration was observed in the other regions, GCL and WM (Fig. 3.1.C-D).

To understand whether the reduced size of the cerebellum was due to a decreased number of PCs in RIM4 KO$_{const}$ mice, the number of PCs was quantified in cerebellar sections after immunolabeling against calbindin (Fig. 3.1.E). The density of PCs along the PCL was calculated by dividing the number of PCs by the length of the PCL and no clear difference was observed in RIM4 KO$_{const}$ compared to WT mice (Fig. 3.1.F).

Next, I addressed the question if the reduced cerebellar area could be caused by alterations in the PC dendritic tree, located in the ML. To address this, the thickness of the ML was determined in the cerebellar vermis (Lobules V and VI) by measuring the average length of straight lines perpendicular to the PCL. RIM4 KO$_{const}$ mice showed a significantly decreased thickness of the ML compared to the control group (Fig. 3.1.G).
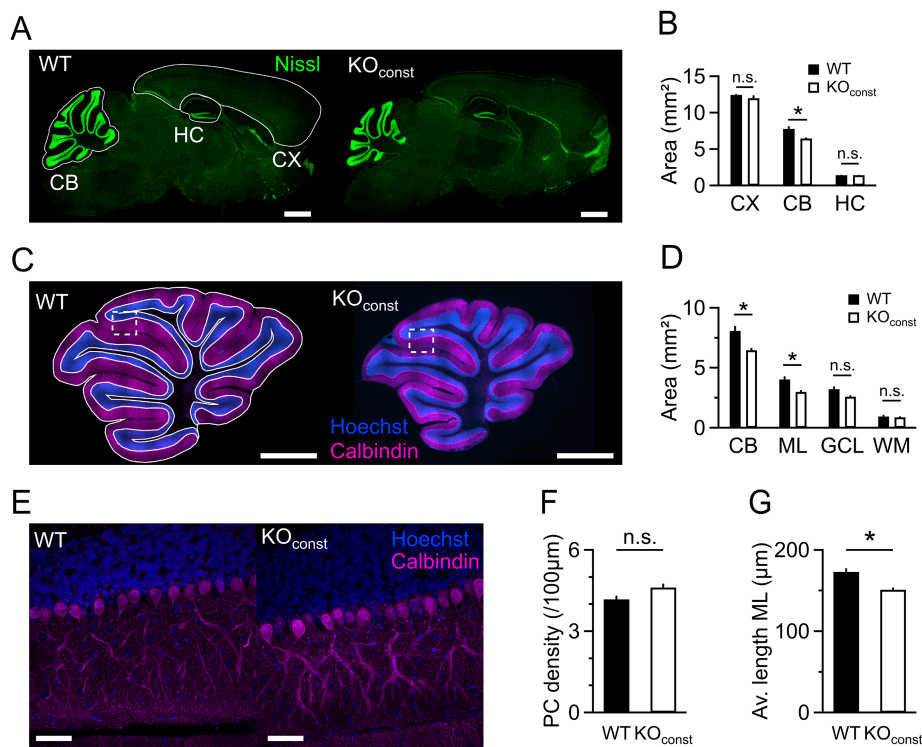

Figure 3.1: **Dysmorphic changes in the cerebellum of RIM4 KO$_{const}$ mice**. A. Representative scans of Nissl-green stained sagittal tissue in RIM4 WT$_{const}$ and KO$_{const}$ mice. The outline in each brain region where the area was measured is indicated (white line). Scale bars = 1 mm. B. The average area of each brain region was determined: RIM4 WT$_{const}$ 12.46 ± 0.12 mm^2, 7.78 ± 0.36 mm^2, 1.43 ± 0.05 mm^2; RIM4 KO$_{const}$ 11.99 ± 0.39 mm^2, 6.47 ± 0.13 mm^2, 1.43 ± 0.05 mm^2; cortex (CX), cerebellum (CB), hippocampus (HC) respectively. C. Representative scans of calbindin- and Hoechst-stained cerebellar tissue of RIM4 WT$_{const}$ and KO$_{const}$ mice. The outlines indicate where

the area was measured (white line). Dotted squares indicate the region shown in Figure E. Scale bars = 1 mm. D. The average area of the whole cerebellum und of the cerebellar sublayers was quantified: CB: RIM4 WT_{const} 8.08 ± 0.42 mm^2 and RIM4 KO_{const} 6.47 ± 0.18 mm^2, ML: RIM4 WT_{const} 4.04 ± 0.25 mm^2 and RIM4 KO_{const} 2.99 ± 0.15 mm^2, GCL: RIM4 WT_{const} 3.22 ± 0.22 mm^2 and RIM4 KO_{const} 2.59 ± 0.1 mm^2, and WM: RIM4 WT_{const} 0.95 ± 0.13 mm^2 and RIM4 KO_{const} 0.88 ± 0.07 mm^2 E. Representative scans of Hoechst and calbindin stained cerebellar tissue of RIM4 WT_{const} and KO_{const} mice. Scale bars = 50 µm. F. The mean density of PCs was measured in RIM4 WT_{const} 4.18 ± 0.13 and RIM4 KO_{const} 4.61 ± 0.14. G. The thickness of the ML was 173.05 ± 4.36 µm in RIM4 WT_{const} and 151.08 ± 2.83 µm in RIM4 KO_{const}. The bar graphs depict means ± SEM. Statistical significance was tested by unpaired Student's t-test (* $p < 0.05$).

3.1.2 Reduced complexity of dendritic arbors of Purkinje cells in RIM4 KO_{const} mice

Multiple studies examining ataxic mouse models demonstrated that a disrupted architecture of PCs is the cause for an impaired motor behavior (Gao et al., 2011; Girard et al., 2011; Jayabal et al., 2015). Based on the observation of a reduction in the thickness of the ML in the absence of RIM4, I next investigated the cytoarchitecture of PCs in RIM4 KO_{const} mice. For the analysis of PC morphology, individual PCs were labelled with 1 mM TMR-Dextran (3kDa) by single cell electroporation in cerebellar slices of both RIM4 WT_{const} and KO_{const} mice (over 100 days old; both genders; 11 WT_{const} mice, 10 KO_{const} mice). Labelled PCs were imaged using a laser-scanning confocal microscope and reconstructed in three dimensions (3D).

Obvious alterations in PCs of RIM4 KO_{const} mice were noticeable in images of MIPs, showing considerably less complex dendritic trees (Fig. 3.2.A). Firstly, the size of the dendritic tree of PCs was compared by measuring the area of an outline of the whole dendritic tree revealing a significant reduction by 40% in RIM4 KO_{const} mice (Fig. 3.2.B). Next to evaluate dendritic arborization, Sholl intersections were measured from reconstructed PCs with incremental concentric spheres spaced at 1 µm. The profiles plotting the number of Sholl intersections against the radial distance from the cell body showed clear differences in dendritic arborization. PCs of RIM4 KO_{const} mice showed less branching distally than those of WT_{const} mice, as evidenced by the maximum distance was smaller in RIM4 KO_{const} mice lacking dendrites over 200 µm from the soma (Fig. 3.2.C). It has been reported that branching patterns of PC trees are different depending on their location (Nedelescu et al., 2017). As I collected PCs located in either Lobule VI or VIII, I next examined PCs in these two locations separately. Although distinct branching patterns were observed depending on the location of the PCs, the results of the Sholl analysis were

comparable to the pooled data. Since the MIP images (Fig. 3.2.A) as well as the Sholl profiles exhibited reduced dendritic arbors in the middle of PC tree showing the lower number of intersections in the middle of branches around 100 μm from the soma (Fig. 3.2.C), I also assessed dendritic branch levels in each dendrite segment in order to compare the complexity of dendritic arbors in RIM4 KO_{const} mice. The total dendrite length was significantly smaller in branch levels 4, 5, and 6, while there were no differences in the dendritic complexity at the primary and distal branch levels (Fig. 3.2.D).
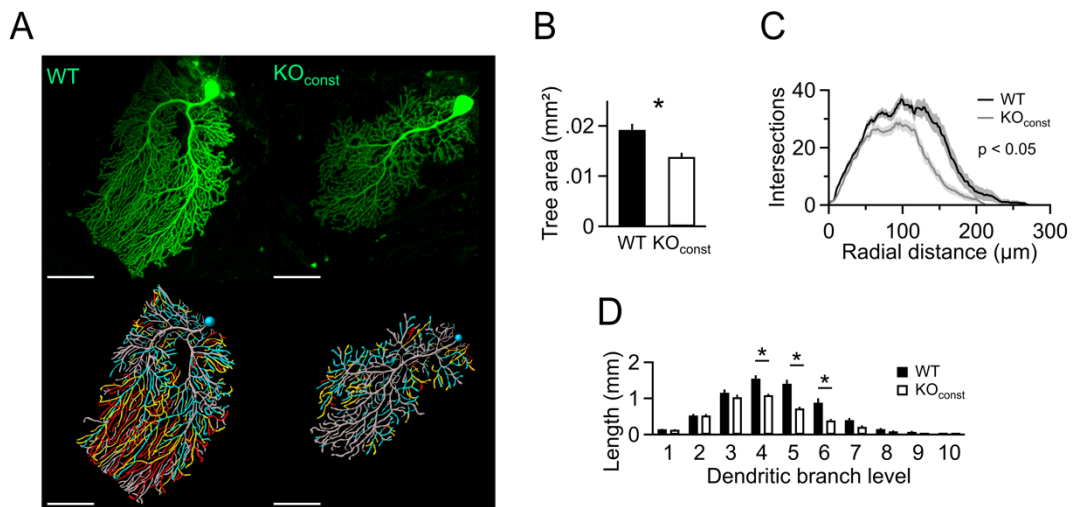

Figure 3.2: **Reduced dendritic arborization of Purkinje cells in RIM4 KO_{const} mice.** A. Representative scans of PCs labelled with 1 mM TMR-Dextran (upper panel) in RIM4 WT_{const} and KO_{const} mice, and reconstructed PCs in three dimensions (lower panel), color-coded branch levels (level 4 blue, level 5 yellow, and level 6 red). Scale bars, 50 μm. B. The mean area of the PC tree was reduced in RIM4 KO_{const} mice compared to WT, RIM4 WT_{const} 1.92 ± 0.12 x10^{-2} mm^2 and RIM4 KO_{const} 1.38 ± 0.08 x10^{-2} mm^2. C. Sholl analysis with incremental spheres at 1 μm interval revealed a reduced dendritic arborization in RIM4 KO_{const} mice. Kolmogorov-Smirnov test, $p < 0.05$. D. The total dendrite length depending on the branch level was measured in RIM4 WT_{const} and KO_{const} mice, RIM4 WT_{const} 1.6 ± 0.1 mm and RIM4 KO_{const} 1.1 ± 0.04 mm, at branch level 4; RIM4 WT_{const} 1.4 ± 0.1 mm and RIM4 KO_{const} 0.7 ± 0.04 mm, at branch level 5; RIM4 WT_{const} 0.9 ± 0.1 mm and RIM4 KO_{const} 0.4 ± 0.04 mm at branch level 6. The bar graphs show means ± SEM. Statistical significance was tested by unpaired Student's t-test (* $p < 0.05$) and with Bonferroni's correction for multiple comparisons.

3.2 The RIM4 deficiency results in disturbed spontaneous activity of Purkinje cells

PCs display spontaneous firing spikes even in the absence of synaptic inputs, and their pattern is highly regular (Häusser and Clark, 1997). As many mouse ataxia models demonstrated signaling deficits in pace-making activity of PCs (Raman et al., 1997; Walter et al., 2006; Kalume et al., 2007), I examined spontaneous spikes of PCs in RIM4-deficient

mice. I used slices of the sagittal cerebellar vermis of fully matured RIM4 WT$_{const}$ and KO$_{const}$ mice that were over 25 weeks old (5 RIM4 WT$_{const}$ mice and 6 KO$_{const}$ mice) and recorded spontaneous spikes juxtacellularly for 3-5 minutes in the presence of synaptic blockers (20 µM CNQX, 10 µM Gabazine). Recording electrodes containing sACSF were placed near the axon hillock of PCs (Fig. 3.3.A). Only healthy PCs located in Lobule V-VIII were selected for recordings and discarded if they showed run-down by checking the raster plots of the whole recording period during the analysis. Both RIM4 WT$_{const}$ and KO$_{const}$ mice showed regular spontaneous spikes but the mean firing rate was significantly decreased in RIM4 KO$_{const}$ mice (Fig. 3.3.B). To evaluate the firing behavior in detail, I analyzed the distribution of inter-spike intervals (ISIs) and calculated the coefficient of variation of the ISIs (CV$_{ISI}$), the ratio of the standard deviation to the mean, and plotted the cumulative distribution of CV$_{ISI}$ with a corresponding firing rate (Fig. 3.3.C). Two distinct populations were observed in the histogram of the CV$_{ISI}$ in WT$_{const}$ mice, a lower CV$_{ISI}$ group (tonic firing) and a higher CV$_{ISI}$ group with a higher firing rate (bursting) (Fig. 3.3.C), while a higher CV$_{ISI}$ group with over 1.0 CV$_{ISI}$ was absent in PCs of RIM4 KO$_{const}$ mice.

It was previously reported that PCs display a distinct firing behavior, called trimodal firing which consists of three different firing behaviors of PCs: tonic, silent and burst (Womack and Khodakhah, 2002). Tonic PCs are regularly firing cells with a lower CV$_{ISI}$ value (typically below 0.1) while bursting is relatively irregular displaying higher CV$_{ISI}$ values. Recorded PCs with higher CV$_{ISI}$ in WT$_{const}$ mice showed a comparable firing behavior as described in Womack and Khodakhah's study. Therefore, I defined distinct populations of PCs in WT$_{const}$ mice according to the CV$_{ISI}$ and compared the mean firing rate as well as the mean CV$_{ISI}$. The mean firing rate was still lower in RIM4 KO$_{const}$ mice when only tonically firing cells were selected (Fig. 3.3.C$_{(a)}$). Although most PCs showed tonic firing, there were some PCs exhibiting a rhythmical bursting while this population was surprisingly absent in RIM4 KO$_{const}$ mice (Fig. 3.3.C$_{(c)}$). Similar to the previous reports in dissociated PCs (Swensen and Bean, 2003), *in vitro* acute slices (Womack and Khodakhah, 2002), and *in vivo* (Jaeger and Bower, 1994), a stereotypical spike discharge was observed in RIM4 WT$_{const}$ mice during the burst firing: firing rates were gradually increased and terminated with an even more rapid increase in the firing rate and a smaller amplitude of the spike followed by a short pause up to several seconds (Fig. 3.4.A-B).

This pause (0.5-1 s), the inter-bursting interval, was relatively regular indicated by a lower CV$_{ISI}$ value as well as a lower peak in the Autocorrelogram (Fig. 3.4.C-D).
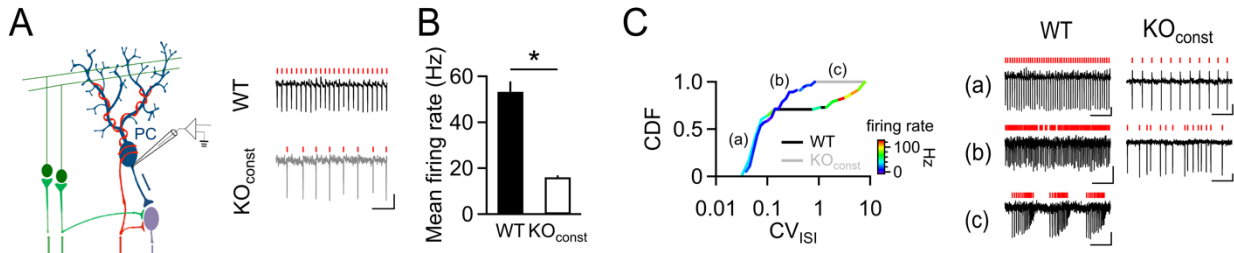

Figure 3.3: **Disturbed spontaneous firing in RIM4 KO$_{const}$ mice.** A. Schematic depiction of juxtacellular recordings of spontaneous spikes in PCs (left panel) and representative traces of regularly firing spikes in both RIM4 WT$_{const}$ and KO$_{const}$ mice. The recording electrode was located around the axon hillock of PCs. Both excitatory and inhibitory inputs were pharmacologically blocked (20 µM CNQX, 10 µM Gabazine). B. The mean firing rate of PCs was reduced in RIM4 KO$_{const}$ mice: RIM4 WT$_{const}$ 53.3 ± 4.5 Hz, RIM4 KO$_{const}$ 16.1 ± 0.85 Hz. C. Histogram of log transformed CV$_{ISI}$ combined with the mean firing rate, color-coded from 0 Hz in blue to 100 Hz in red showing a distinct population of firing PCs in WT$_{const}$ (left panel). Representative traces for each population are depicted in the right panel. The bar graphs show means ± SEM. Statistical significance was tested by unpaired Student's t-test (* p < 0.05).
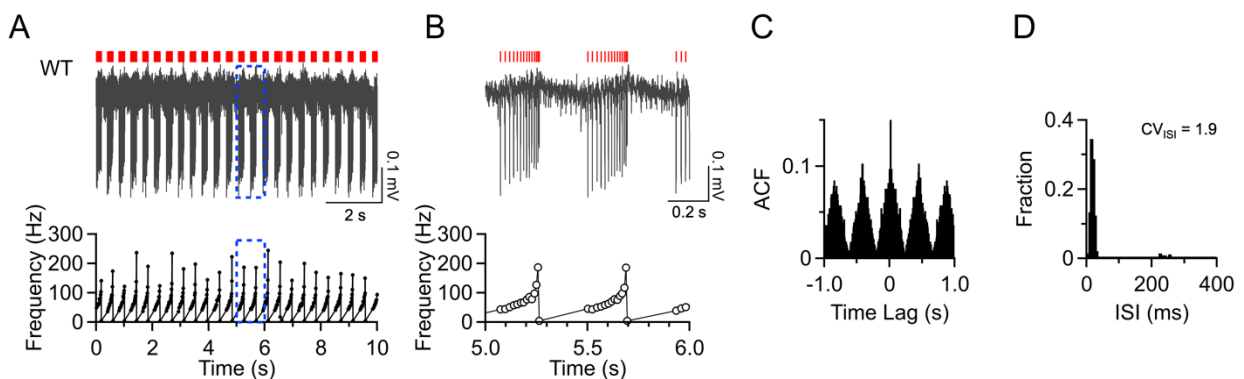

Figure 3.4: **Characterization of rhythmical bursting of PCs *in vitro*.** A-B. A rhythmical bursting of PCs was extracellularly recorded in slices. Each burst consisted of a train of several spikes and ended with a smaller spike. The firing rate was increased gradually during the burst and increased even more rapidly at the end of the burst. After each burst, there was a short pause (0.5-1 s). C. Peaks in the auto-correlogram revealed a rhythmical firing with a 0.5 s interval. Autocorrelation function (ACF). D. A histogram of ISIs during bursting showed two distinct group of spikes: rapid spikes during the burst, 10 ms interval; between bursts, 235 ms interval. The CV$_{ISI}$ value during the entire burst was 1.9.

3.3 Caffeine application reduces the firing rate of Purkinje cells in RIM4 KO$_{const}$ mice

Caffeine has been shown to evoke episodic motor impairments in many ataxia studies (Fureman et al., 2002; Raike et al., 2013; Tara et al., 2018). After intraperitoneally injection

of caffeine (25 mg/kg) into the RIM4 KO_{const} mice all of them developed motor impairments similar to the spontaneously occurring ones (mu data, Eva Schönhense, Nesrine Melitti). Therefore, I tested whether application of caffeine to the cerebellar slice disturbed spontaneous spikes or not. Spontaneous spikes of PCs were recorded juxtacellularly as a non-invasive method in both RIM4 WT_{const} and KO_{const} mice (3 mice in each group). After the stable baseline recording for 5 minutes, sASCF containing caffeine was applied in the bath for 10 minutes and washed out. Interestingly, caffeine disturbed spontaneous spikes of PCs in WT_{const} mice (Fig. 3.5). To determine the concentration dependence of the effect of caffeine on the spontaneous spikes of WT PCs, as a first step, I tested different caffeine concentrations before I examined the effect in RIM4 KO_{const} mice: 1, 3, 10, 20 mM. These experiments revealed that PCs suddenly stopped firing upon 20 mM Caffeine application (Fig. 3.5.E) but showed minimal effects on the firing rate without altering spike regularity in 1 mM caffeine (Fig. 3.5.A-D). To test if the application of a lower caffeine affects significantly more in RIM4 KO_{const} mice, it was determined to apply 1 mM caffeine in both RIM4 WT_{const} and KO_{const} mice and compare the effect (Fig. 3.6). The mean firing rate was significantly reduced in PCs of RIM4 KO_{const} mice while it was unchanged in WT_{const} mice (Fig. 3.6.B-D).

In conclusion, spontaneously firing spikes of PCs were disturbed in RIM4 KO_{const} mice showing a decreased mean firing rate. As a well-known trigger of ataxic episodes, caffeine was applied onto cerebellar slices and found to reduce the firing rate without altering regular firing behavior of PCs in RIM4 KO_{const} mice.
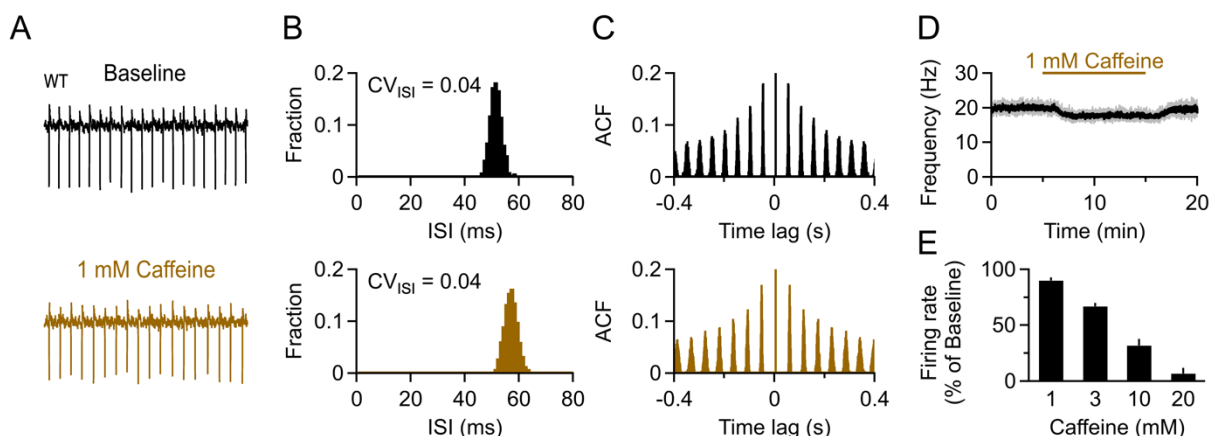

Figure 3.5: **Concentration-dependent effect of caffeine on spontaneous spikes.** A. Representative traces of spontaneous spikes in WT_{const} PCs at baseline (upper panel, black) and after 10 min of 1 mM caffeine application (lower panel, brown). B. Histogram

of ISIs and calculated CV_{ISI} (0.04 for both conditions). C. The autocorrelogram of the spikes during the 1 mM caffeine application was comparable to the one at baseline. D. A time course of frequency was plotted while 1 mM caffeine was applied in the bath. E. A summary of the concentration-dependent effect of caffeine on spontaneous spikes in WT_{const} PCs. Firing rate changes compared to baseline: 89.9 ± 2.8 % in 1 mM, 67.1 ± 3.2 % in 3 mM, 31.9 ± 5.9 % in 10 mM, 6.8 ± 5.1 % in 20 mM. The bar graphs indicate means ± SEM.
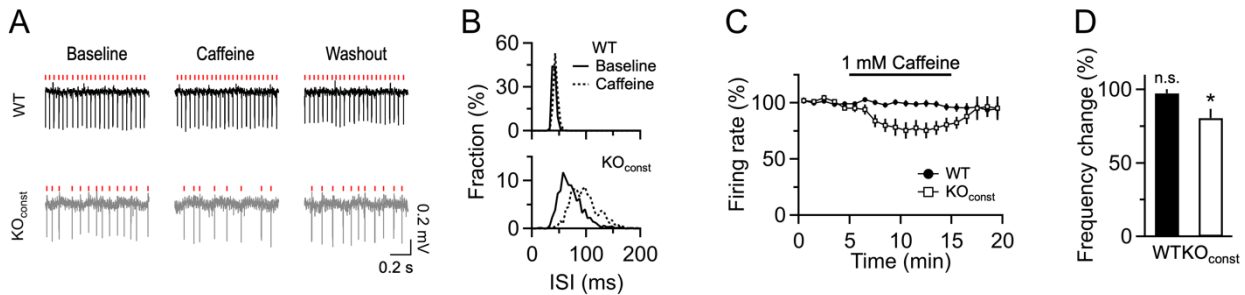

Figure 3.6: **Caffeine application strongly disturbed spontaneous spikes in RIM4 KO_{const} mice.** A. Representative traces of spontaneous spikes in each condition in RIM4 WT_{const} and KO_{const} mice. B. Histograms of ISIs showed that caffeine disturbed spontaneous spikes in RIM4 KO_{const} mice. Solid lines, baseline; dash lines, caffeine application. C. A time course of firing rate during 1 mM caffeine bath application. D. The frequency change was quantified 10 min after the caffeine application. RIM4 WT_{const} 97.5 ± 2.9 % and RIM4 KO_{const} 80.5 ± 6.3 %. The bar graphs indicate means ± SEM. Statistical significance was tested by unpaired Student's t-test (* $p < 0.05$).

3.4 The RIM4 deficiency disrupts calcium transient in Purkinje cells

Imaging changes in the intracellular calcium concentration of neurons is a commonly used to monitor neuronal activity. Previous studies have assessed calcium transients in PCs both *in vitro* and *in vivo* and revealed the importance of calcium signals to cause cerebellar outputs (Konnerth et al., 1992; Roome and Kuhn, 2018). RIM proteins are known to regulate VGCCs at presynapses and lack of RIM1/2 leads to a decreased density of VGCCs as well as to a reduced amplitude of presynaptic Ca^{2+} transients (Han et al., 2011; Kaeser et al., 2011). It is so far unknown if also RIM4 impacts the function and/or abundance of VGCCs, although the previous report showed that RIM3 and RIM4 bind to the β-subunit of VGCCs (Uriu et al., 2010).

3.4.1 Spontaneous *in vivo* calcium events in Purkinje cell dendrites are strongly disturbed in RIM4 KO_{const} mice

In vivo calcium imaging of PCs was performed in anesthetized and head fixed RIM4 WT_{const} and KO_{const} mice (6 RIM4 WT_{const} mice and 7 KO_{const} mice). In order to detect

calcium transients a genetically encoded calcium indicator, GCaMP6f, was virally transduced targeting PCs located at cerebellar vermis (especially lobules V and VI; Fig. 3.7.A; see also 2.4). An acute cranial window was inserted above the cerebellum where AAV-GCaMP6f had been injected, and PCs were imaged using a two-photon scanning microscope (Fig. 3.7.B; see also 2.9). Spontaneous calcium transients were detected in PC dendrites of both RIM4 WT$_{const}$ and KO$_{const}$ mice with a frame rate of 10 Hz (100.5 ms/frame), and average fluorescence traces from each dendrite were extracted by the anatomical structure of PC dendrites (Fig. 3.7.B). Notably, the average amplitude of spontaneous calcium spikes was significantly reduced in RIM4 KO$_{const}$ mice (Fig. 3.7.C-D). Although the average event rate was similar (Fig. 3.7.E), the temporal distribution of spontaneous calcium events was clearly different. In WT a distinct distribution of inter calcium-event intervals which were primarily driven by burst inputs from the IO was observed, showing three populations (three peaks in the histogram; Fig. 3.7.F). On the other hand, this firing behavior was lost in RIM4 KO$_{const}$ mice (Fig. 3.7.F).

 It has been reported that a group of 20-40 PCs deliver a synchronized signal to one DCN neuron eliciting a time-locking cerebellar output (Person and Raman, 2012). An erratic population activity of PCs has been demonstrated in previous ataxia studies (Hoebeek et al., 2005; Chen et al., 2009). Therefore, I analyzed the synchrony of spontaneous *in vivo* calcium events in neighboring PCs in RIM4 KO$_{const}$ mice. To this end, the Pearson correlation coefficient was compared between neighboring dendrites in RIM4 WT$_{const}$ and KO$_{const}$ mice depending on the distance between the centroids of the dendrites (Fig. 3.7.G). In both groups, PCs displayed a tendency to higher correlated calcium events between closer dendrites and lower synchronicity between remote dendrites (Fig. 3.7.G). However, the overall level of synchronicity between PC dendrites within the microzone was significantly reduced independent of their distance (Fig. 3.7.G-H). Reduced synchrony in RIM4 KO$_{const}$ mice was also clearly found in the raster plot of spontaneous calcium events showing weakly aligned spikes across PC dendrites within the microzone (Fig. 3.7.I).

 Taken together, these results show that ablation of RIM4 causes a reduced calcium transient and an altered temporal pattern of population activity in PCs.
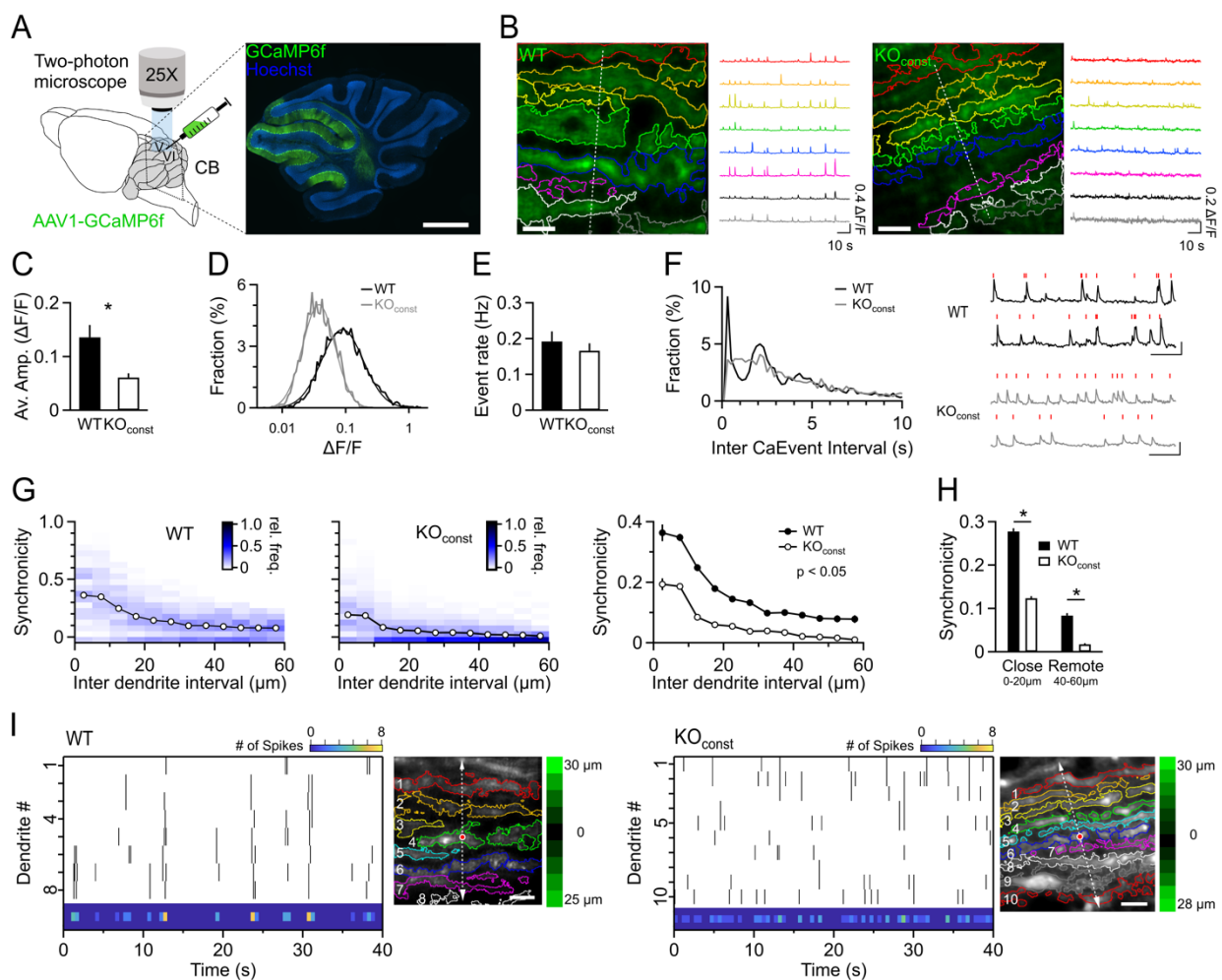
Figure 3.7: *In vivo calcium transient and the synchrony in neighboring PCs are reduced in RIM4 KO$_{const}$ mice.* A. Schematic depiction of AAV injection and *in vivo* calcium imaging in the cerebellum (left panel) and exemplary scan showing GCaMP6f expressing PCs as a result of viral transduction (right panel). B. Representative scans and extracted calcium traces in each corresponding dendrite in RIM4 WT$_{const}$ and KO$_{const}$ mice. C. The mean amplitude of calcium events was decreased in RIM4 KO$_{const}$ mice. RIM4 WT$_{const}$ 0.14 ± 0.02 ΔF/F, KO$_{const}$ 0.06 ± 0.01 ΔF/F. D. Gaussian distribution of amplitude of calcium events revealed the shift of the entire population in RIM4 KO$_{const}$ mice. E. The average event rate of spontaneous calcium events was not changed. RIM4 WT$_{const}$ 0.19 ± 0.03 Hz, KO$_{const}$ 0.17 ± 0.02 Hz. F. The distribution of the inter-calcium event interval showed distinct groups in RIM4 WT$_{const}$ mice but was lost in KO$_{const}$ mice. Representative traces showing these spike patterns (right panel). G. The synchronicity of spontaneous calcium events between dendrites was plotted against the inter dendrite interval measured by the shortest distance between the centroids of dendrites. A two-way ANOVA test was performed to test for significant differences between RIM4 WT$_{const}$ and KO$_{const}$ mice. H. The average value of synchronicity was compared depending on the distance between dendrites: close, 0-20 μm and remote 40-60 μm. RIM4 WT$_{const}$ 0.28 ± 0.01 in Close and 0.08 ± 0.01 in Remote, KO$_{const}$ 0.12 ± 0.01 in Close and 0.02 ± 0.01 in Remote. I. The temporal distribution of calcium events was described by a raster plot of representative experiments in RIM4 WT$_{const}$ and KO$_{const}$ mice (left panel). Each black bar indicated an

individual calcium spike. PC dendrites within the microzone were selected (right panel) and the distance was measured from the center dendrite in the field of view (red dot, center dendrite; dash arrows, mediolaterally spaced dendrites) and color coded (black to bright green). Color-coding (from 0 dark blue to 8 bright yellow) indicated the sum of the number of calcium spikes in each bin (left panel). The bar graphs indicate means ± SEM. Statistical significance was tested by unpaired Student's t-test (* $p < 0.05$).

3.4.2 A calcium-related signaling deficit is found in the cerebellar slice of RIM4 KO_{const} mice

As a next step to understand the signaling deficit in spontaneous *in vivo* calcium events in RIM4 ablated mice, I investigated a calcium-related signaling in PCs by performing whole-cell patch clamp in PCs of RIM4 WT_{const} and KO_{const} mice. It has been reported that spontaneous *in vivo* calcium transients in PCs are primarily driven by CF activity (Roh et al., 2020). Therefore, I next examined CF-evoked signaling in PCs (RIM4 WT_{const} 8 cells from 3 mice and KO_{const} 11 cells from 3 mice). PCs were voltage-clamped at -70 mV and CFs were electrically stimulated with paired-pulse stimuli spaced at 50 ms by a glass electrode (Fig. 3.8.A; see also 2.7.2). GABAergic inputs were blocked by using 10 µM Gabazine to isolate EPSCs. In both RIM4 WT_{const} and KO_{const} mice, PCs displayed stereotypical EPSCs with a paired-pulse depression showing a reduced magnitude at the second response (Fig. 3.8.B). However, the mean amplitude of the first peak of EPSCs was strongly increased in RIM4 KO_{const} mice (Fig. 3.8.C). To rule out artifacts from the whole cell recordings, the series resistance (R_s) was monitored, discarding cells with a higher R_s value over 20 MΩ or a change over 20% during recordings. Yet, there was no significant difference in R_s between recorded cells (Fig. 3.8.D). On the other hand, the PPR remained unchanged in RIM4 KO_{const} mice suggesting an unaltered probability of neurotransmitter release at CFs (Fig. 3.8.E).

Next, postsynaptic calcium transients evoked by CF-stimulation were measured in PCs of RIM4 WT_{const} and KO_{const} mice (10 cells from 4 WT_{const} mice and 13 cells from 5 KO_{const} mice). PCs were labelled with the calcium indicator, OGB-1, and whole-cells clamped at -70 mV (Fig. 3.9.A). Electrical stimulation of CFs triggered a strong calcium transient in the whole dendritic tree of PCs (Fig. 3.9.B). Interestingly, the amplitude of the calcium transients as well as of the complex spikes were unchanged in RIM4 KO_{const} mice (Fig. 3.9.B-C). When multiple inputs of CFs were delivered to PCs in short intervals (0.3 s),

however, PCs in RIM4 KO_{const} mice were not able to integrate the magnitude of the calcium transient to the same degree as WT_{const} PCs (Fig. 3.9.D-E). Additionally, I did not find signs of multiple innervations of CFs onto a single PC showing a "all-or-none" response regardless of stimulation intensity (Fig. 3.9.F).

Additionally, I investigated if ablation of RIM4 in PCs caused changes in VGCCs. OGB-1 labelled PCs were voltage-clamped at -60 mV via a recording electrode. To isolate calcium currents in PCs, multiple channels and receptors were blocked by applying 1 µM TTX (Na^+ channels), 1 mM TEA and 100 µM 4AP (K^+ channels), 50 µM APV, and 20 µM CNQX (glutamate receptors, NMDARs and AMPARs) while depolarizing the somata of PCs to -10 mV (Fig. 3.10.A-B). As a result, a calcium transient was triggered along the entire PC tree in both RIM4 WT_{const} and KO_{const} mice (Fig. 3.10.B). Interestingly, both the mean calcium transient along the entire PC dendrites and the peak calcium current were significantly increased in RIM4 KO_{const} mice (Fig. 3.10.C-D), indicating a potentially a higher number of VGCCs.

In summary, these *in vitro* results suggest that the presence of RIM4 is critical to maintain normal calcium signaling in PCs.
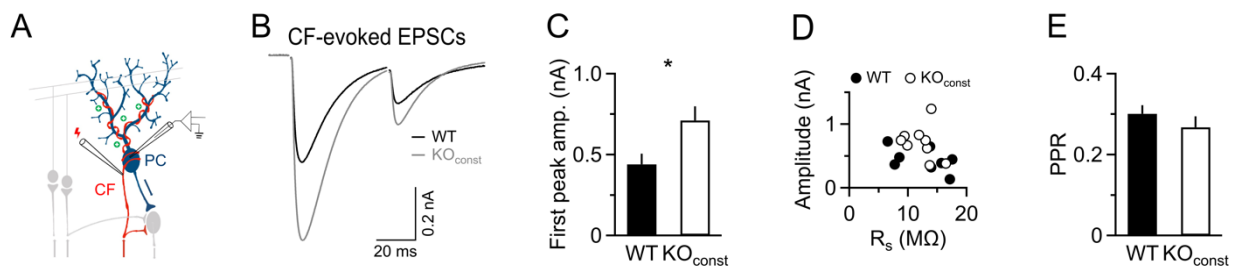

Figure 3.8: CF-mediated EPSCs are increased in PCs of RIM4 KO_{const} mice. A. Cartoon depicting the set-up of the whole-cell voltage clamp experiments in PCs. CFs were electrically stimulated with a glass electrode. B. EPSCs were evoked by paired-pulse stimuli spaced at 50 ms in both RIM4 WT_{const} and KO_{const} mice. C. The average amplitude of the first peak of EPSCs was increased in RIM4 KO_{const} mice. RIM4 WT_{const} 0.44 ± 0.07 nA and KO_{const} 0.71 ± 0.09 nA. D. Series resistance (R_s) was monitored in each recording and discarded when it was over 20 MΩ. E. The paired-pulse ratio (PPR) was unchanged in RIM4 KO_{const} mice. RIM4 WT_{const} 0.3 ± 0.02 and KO_{const} 0.27 ± 0.03. The bar graphs indicate means ± SEM. Statistical significance was tested by unpaired Student's t-test (* $p < 0.05$).
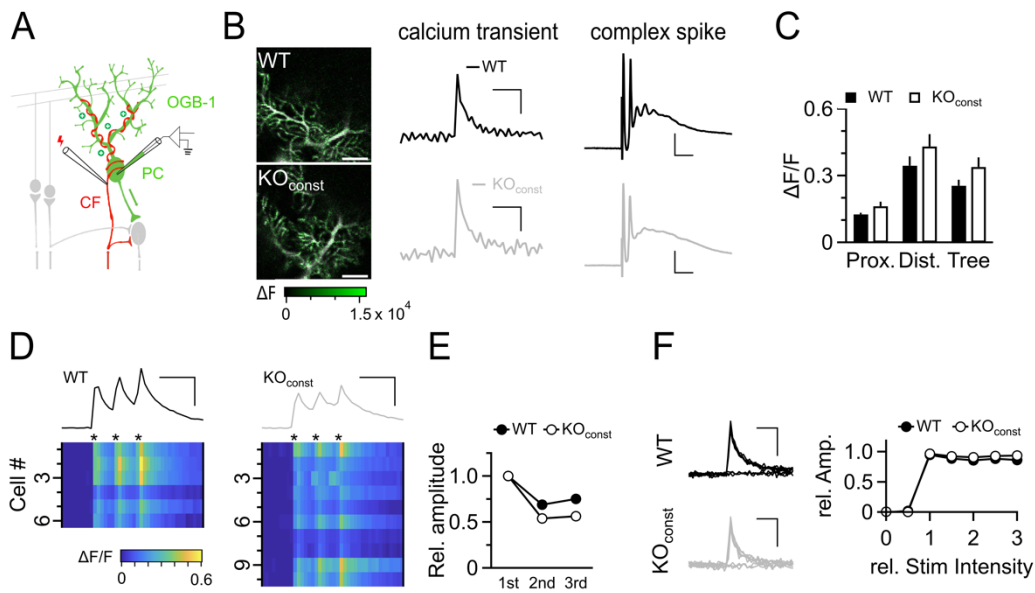
Figure 3.9: **CF-evoked calcium transients are unchanged, but multiple CF inputs trigger the lower calcium transient in RIM4 KO$_{const}$ mice.** A. Scheme depicting the experimental set-up. PCs were voltage-clamped with a recording electrode filled with the calcium indicator OGB-1 and CFs were electrically stimulated. B. Representative experiments in RIM4 WT$_{const}$ and KO$_{const}$ mice showing CF-evoked postsynaptic calcium transients in PC dendrites. ΔF at peak (color-coded, 0 black to 1.5 x 10^4 bright green) was superimposed to the average F scan (white). Corresponding traces of calcium transients (middle panel) upon CF-stimulation after image analysis and current traces showing complex spikes (right panel) from somatic current-clamp recordings. Scale bars: 1 s (horizontal, middle panel) and 0.1 $\Delta F/F$ (vertical, middle panel); 5 ms (horizontal, right panel) and 20 mV (vertical, right panel). C. The average amplitude was measured depending on the location of the dendrites: proximal (Prox.) and distal (Dist.) part of PC dendrites, and the whole tree (Tree). RIM4 WT$_{const}$ 0.13 ± 0.01 $\Delta F/F$ in Prox., 0.34 ± 0.04 $\Delta F/F$ in Dist., and 0.25 ± 0.03 $\Delta F/F$ in Tree; KO$_{const}$ 0.16 ± 0.02 $\Delta F/F$ in Prox., 0.43 ± 0.06 $\Delta F/F$ in Dist., and 0.34 ± 0.04 $\Delta F/F$ in Tree. D. Representative traces and color-coded $\Delta F/F$ profiles (0 dark blue to 0.6 bright yellow) of calcium transients in PCs of RIM4 WT$_{const}$ and KO$_{const}$ mice. Asterisks indicates when CFs were stimulated. Scale bars: 0.5 s (horizontal) and 0.1 $\Delta F/F$ (vertical). E. The relative amplitude in each response was reduced in RIM4 KO$_{const}$ mice. RIM4 WT$_{const}$ 0.69 ± 0.02 at 2nd response and 0.75 ± 0.02 at 3rd response; KO$_{const}$ 0.54 ± 0.02 at 2nd response and 0.56 ± 0.02 at 3rd response. F. Representative traces of calcium transients in PCs with a different simulation intensity (left panel) and the averaged amplitude change over the stimulation intensity (right panel). Both the amplitude and the stimulation intensity were normalized to the first response. Scale bars: 1 s (horizontal) and 0.05 $\Delta F/F$ (vertical). The bar graphs indicate means ± SEM. Statistical significance was tested by unpaired Student's t-test (* p < 0.05).
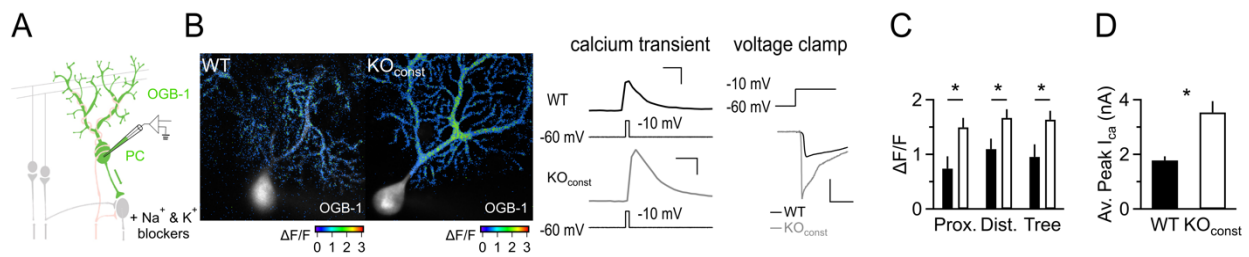
Figure 3.10: Higher calcium currents are found in PCs of RIM4 KO_const mice. A. A schematic depiction of the calcium imaging experiments. PCs were filled with the calcium indicator OGB-1. B. Representative experiments showing a calcium transient in PCs after a somatic depolarization via a recording pipette. ΔF at peak (color-coded, 0 purple to 3 $\Delta F/F$ red) was superimposed to the average F scan (white). Corresponding traces of calcium transients (middle panel) upon somatic depolarization after image analysis and voltage traces (right panel) from somatic voltage-clamp recordings. Scale bars: 1 s (horizontal, middle panel) and 0.5 $\Delta F/F$ (vertical, middle panel); 20 ms (horizontal, right panel) and 2 mA (vertical, right panel). C. The average amplitude ($\Delta F/F$) of the calcium transients was measured depending on the location of dendrites: proximal (Prox.) and distal (Dist.) part of PC dendrites, and the whole tree (Tree). RIM4 WT_const 0.74 ± 0.22 $\Delta F/F$ in Prox., 1.1 ± 0.2 $\Delta F/F$ in Dist., and 0.95 ± 0.23 $\Delta F/F$ in Tree; KO_const 1.50 ± 0.17 $\Delta F/F$ in Prox., 1.67 ± 0.16 $\Delta F/F$ in Dist., and 1.64 ± 0.16 $\Delta F/F$ in Tree. D. The average peak calcium current was strongly increased in RIM4 KO_const mice. RIM4 WT_const 1.78 ± 0.15 nA and KO_const 3.54 ± 0.41 nA. The bar graphs indicate means ± SEM. Statistical significance was tested by unpaired Student's t-test (* $p < 0.05$).

3.5 Purkinje cell specific RIM4 KO mice reproduces the phenotype of the constitutive knockout

The results from the analysis of the constitutive RIM4 mice showed that loss of RIM4 function impacted dendritic morphology, pace-making activity, as well as calcium signaling in PCs, and ultimately resulted in the occurrence of an episodic motor impairment. The availability of conditional RIM4 KO mice enabled us to ablate RIM4 specifically in cerebellar PCs. RIM4[floxed] mice were crossed with B6.129-Tg(Pcp2-cre)2Mpin/J mice expressing Cre recombinase under the Purkinje cell-protein 2 (PCP2) promotor producing off-spring with RIM4 KO alleles by Cre-mediated recombination specifically in PCs (RIM4 KO_PCP2) (see 2.1.1; unpublished data). As control group, I used WT mice from the RIM4[floxed] mouse line expressing Cre-recombinase under control of the PCP2 promoter (WT_PCP2). Firstly, the behavior of the RIM4 KO_PCP2 mice was monitored for 14 consecutive days in video-equipped home cages revealing that the mice developed the similar episodic motor impairments, both spontaneously as well as after caffeine administration (Nesrine Melitti, unpublished data). These observations showed that the striking behavioral

phenotype occurring in RIM4 KO_{const} mice was reproduced by the selective ablation in PCs.

3.5.1 Validation of PC-specific Cre-recombinase expression of the Pcp2-cre line

To validate the PC-specificity of the B6.129-Tg(Pcp2-cre)2Mpin/J line, I evaluated the expressions of the Cre in the cerebellum by crossing the PCP2-cre expressing mice with red fluorescence protein, tdTomato, reporter mice (see 2.1.1). PCP2-cre recombination in the tdTomato-reporter line gave rise to expressions of tdTomato in PCs across the entire cerebellum (Fig. 3.11.A-B). The recombination efficiency was tested in sagittal cerebellar tissues of the PCP2-Cre::tdTomato-reporter line (P24-25 old, 5 mice) stained with green fluorescent Nissl. The number of both tdTomato and Nissl positive PCs was counted and the fraction of colocalized PCs was calculated (Fig. 3.11.B) and revealed a recombination rate of 96% in this line (Fig. 3.11.C). As reported previously (Witter et al., 2016), 4% of Molecular layer interneurons (MLIs) also expressed tdTomato in the reporter line (Fig. 3.11.D-E).
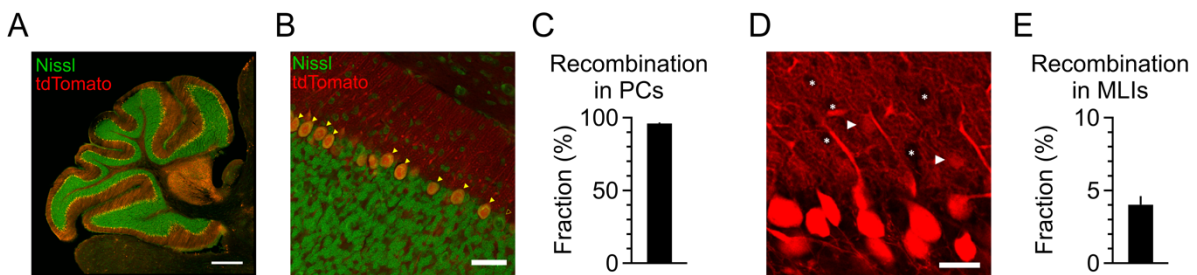

Figure 3.11: **High recombination efficiency in the PCP2-Cre:tdTomato reporter line**. A. Representative scan of the cerebellum in a tdTomato expressing RIM4 WT_{PCP2} mouse. Scale bar, 1 mm. B. Representative scan showing tdTomato positive PCs along the cerebellar lobule VI. tdTomato expressing PCs were counted in Nissl-stained tissue (filled triangle). The empty triangle indicates a PC without tdTomato expression. Scale bar, 50 µm. C. The recombination efficiency in PCP2-Cre:tdTomato in PCs was 96.1 ± 0.7 %. N = 5 mice, p24-25. D. A representative scan showing tdTomato expressing MLIs. Filled triangles indicate tdTomato expressing MLIs and asterisks indicate not recombined MLIs. E. The recombination efficiency of tdTomato in MLIs was 3.7 ± 0.3 %. The bar graphs indicate means ± S.E.M.

3.5.2 Cerebellar area is reduced in RIM4 KO_{PCP2} mice

To test if the morphological changes in the cerebellum also are found in RIM4 KO_{PCP2} mice, the size of the cerebellum was compared between RIM4 WT_{PCP2} and KO_{PCP2} mice (4 RIM4 WT_{PCP2} and 5 KO_{PCP2} mice; both genders) as described in previously for the

constitutive RIM4 KO line (see 3.1.1; Fig. 3.1). Similarly, the overall size of the cerebellum was significantly reduced by 30% in RIM4 KO_{PCP2} mice without changes in other brain regions such as cortex and hippocampus (Fig. 3.12.A-B). Only the area of the ML was smaller in RIM4 KO_{PCP2} mice (Fig. 3.12.C-D). To confirm that the dysmorphic alteration in PC dendritic arborization caused a reduction in cerebellar size, I measured the density of PCs and the thickness of the ML. RIM4 KO_{PCP2} mice showed a decreased thickness of the ML while no obvious changes were detected in the density of PCs (Fig. 3.12.E-G).

In conclusion, the specific ablation of RIM4 in PCs was critical enough to reproduce dysmorphic changes in PCs. Therefore, I deduced that RIM4 has a crucial role in establishing the morphology of PCs and that the deficit in cerebellar morphology could contribute to the motor impairments in RIM4 KO mice.
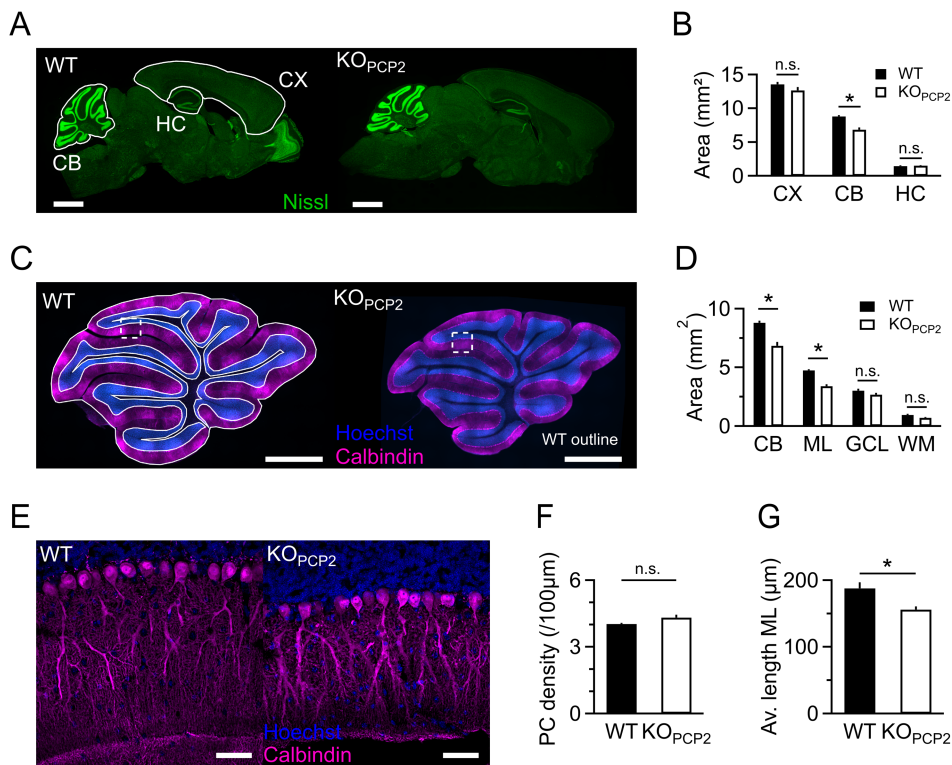

Figure 3.12: **Dysmorphic changes in the cerebellum of RIM4 KO_{PCP2} mice**. A. Representative scans of Nissl-green stained sagittal tissue in RIM4 WT_{PCP2} and KO_{PCP2} mice. The outlines indicate where the area was measured in each brain region. B. The average area of each brain region was measured: RIM4 WT_{PCP2} 13.56 ± 0.37 mm^2, 8.81 ± 0.18 mm^2, 1.44 ± 0.11 mm^2; RIM4 KO_{PCP2} 12.66 ± 0.50 mm^2, 6.85 ± 0.33 mm^2, 1.51 ± 0.06 mm^2; cortex (CX), cerebellum (CB), hippocampus (HC) respectively. C. Representative scans of Calbindin- and Hoechst-stained cerebellar tissue in RIM4 WT_{PCP2} and KO_{PCP2} mice. The outlines indicate where the area was measured in each subregion. Dotted squares indicate the region where scans in Figure E were taken. Scale bars = 1

mm. D. The average area of each region of interests was measured from the whole CB: RIM4 WT$_{PCP2}$ 8.81 ± 0.18 mm^2 and RIM4 KO$_{PCP2}$ 6.85 ± 0.33 mm^2, ML: RIM4 WT$_{PCP2}$ 4.75 ± 0.09 mm^2 and RIM4 KO$_{PCP2}$ 3.41 ± 0.16 mm^2, GCL: RIM4 WT$_{PCP2}$ 3.02 ± 0.17 mm^2 and RIM4 KO$_{PCP2}$ 2.68 ± 0.15 mm^2, and WM: RIM4 WT$_{PCP2}$ 0.96 ± 0.10 mm^2 and RIM4 KO$_{PCP2}$ 0.71 ± 0.07 mm^2 E. Representative scans of Hoechst and calbindin stained cerebellar tissue in RIM4 WT$_{PCP2}$ and KO$_{PCP2}$ mice. Scale bars = 50 µm. F. The mean density of PCs was measured in RIM4 WT$_{PCP2}$ 4.03 ± 0.05 and RIM4 KO$_{PCP2}$ 4.32 ± 0.13. G. The thickness of the ML was 187.87 ± 9.08 µm in RIM4 WT$_{PCP2}$ and 155.88 ± 4.86 µm in RIM4 KO$_{PCP2}$. The bar graphs indicate means ± SEM. Statistical significance was tested by unpaired Student's t-test (* $p < 0.05$).

3.5.3 The spontaneous firing rate of Purkinje cells is reduced in RIM4 KO$_{PCP2}$ mice

Next, I addressed if the signaling deficits in PCs could be reproduced in RIM4 KO$_{PCP2}$ mice. Moreover, the conditional RIM4 KO line allowed us to examine the intrinsic electrophysiological properties of PCs in RIM4-deficient mice by blocking synaptic inputs and to better understand the functional role of RIM4 in PCs. Spontaneous spikes of PCs were recorded juxtacellularly from the mice (6-8 weeks old; 6 WT $_{PCP2}$ and 6 KO $_{PCP2}$ mice) for 5 minutes in each cell in the presence of synaptic blockers (20 µM CNQX, 10 µM Gabazine). Recordings and analysis were performed as described previously for the constitutive RIM4 line (see 3.2). In both RIM4 WT $_{PCP2}$ and KO$_{PCP2}$ mice, PCs displayed regular spontaneous spikes and the mean firing rate was significantly reduced in RIM4 KO$_{PCP2}$ mice (Fig. 3.13.A). I performed the same analysis as for constitutive RIM4 line with regard to the tonic firing behavior and the bursting of PCs. Here, I also found that distinct populations could be identified in the histograms of ISIs in the WT $_{PCP2}$ mice (Fig. 3.13.B) and that the higher CV$_{ISI}$ group, corresponding to bursting PCs, was absent in RIM4 KO$_{PCP2}$ mice (Fig. 3.13.B-D). Among the population of tonically firing PCs with a relatively low CV$_{ISI}$ value in WT $_{PCP2}$ mice, the regularity of spontaneous spikes gradually differed which was noticeable in the recorded spike trains. Nevertheless, irregular firing PCs were not clearly separated based on their distribution of ISIs (Fig. 3.13.C-D). Interestingly, the disturbance in spontaneous firing spikes of PCs was not observed in other mouse lines, such as constitutive RIM1alpha KO and PCP2-RIM1/2 KO mice (Fig. 3.13.E-F).
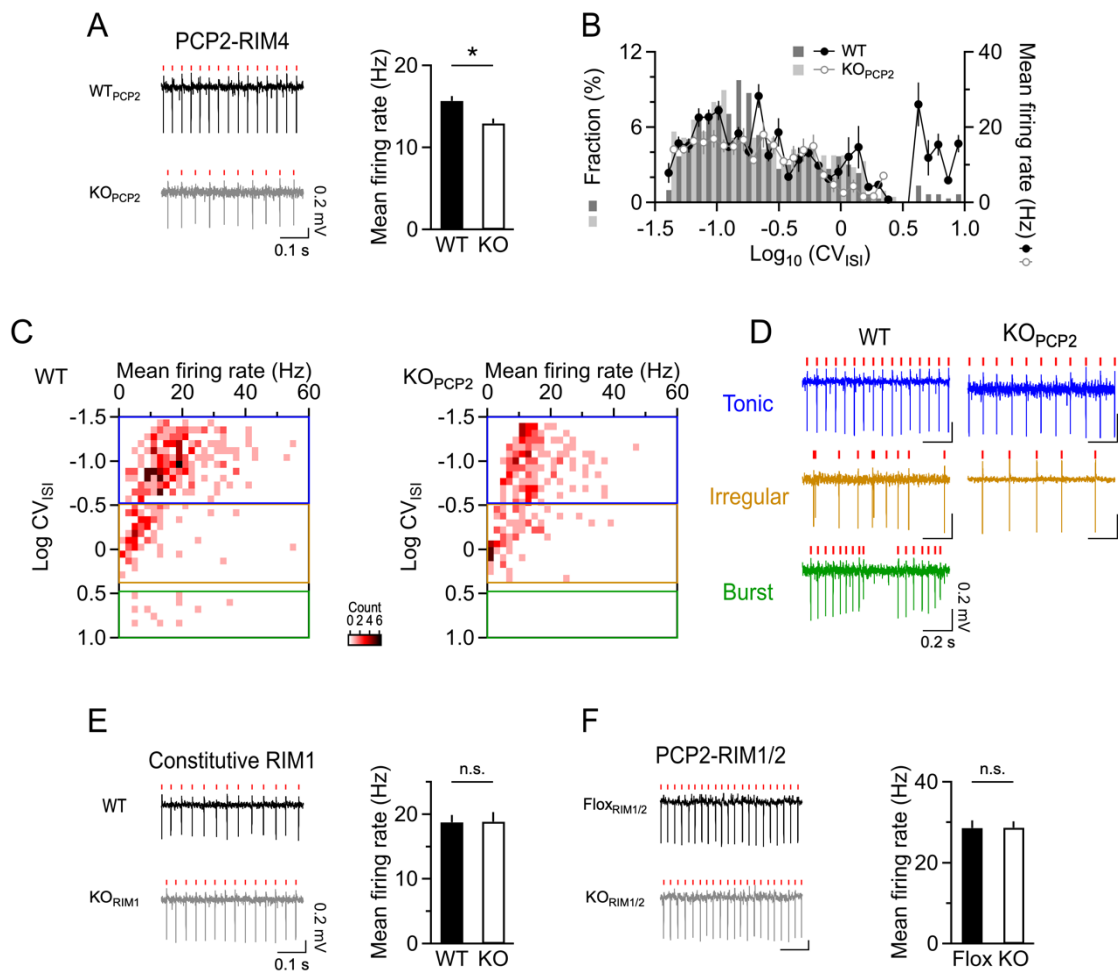
Figure 3.13: **Disturbed spontaneous firing spikes are observed only in RIM4 KO$_{PCP2}$ mice.** A. Representative traces of regularly firing spikes in both RIM4 WT and KO$_{PCP2}$ mice. The recording electrode was located around the axon hillock of PCs. Both excitatory and inhibitory inputs were blocked by blockers in the bath (20 µM CNQX, 10 µM Gabazine). The mean firing rate was reduced in RIM4 KO$_{PCP2}$ mice. RIM4 WT$_{PCP2}$ 15.69 ± 0.58 Hz, RIM4 KO$_{PCP2}$ 12.9 ± 0.59 Hz. B. Histogram of log transformed CV$_{ISI}$ combined with mean firing rate in each bin showing a distinct population of firing PCs. A distinct distribution of CV$_{ISI}$ was observed in WT mice, which was absent in RIM4 KO$_{PCP2}$ mice. C-D. Distribution of recorded PCs in RIM4 WT$_{PCP2}$ and KO$_{PCP2}$ mice: log transformed CV$_{ISI}$ (vertical axis) and mean firing rate (horizontal axis). The number of PCs was color coded: 0 (white) to 6 cells (black). C. Representative traces of PCs displaying a different firing behavior in RIM WT$_{PCP2}$ and KO$_{PCP2}$ mice: tonic (blue), irregular (brown), and burst (green), selected depending on the CV$_{ISI}$ values on the left panels I. E-F. The mean firing rate was unaltered in both constitutive RIM4 KO mice and RIM1/2 KO$_{PCP2}$ mice. Representative traces and the mean firing rate are shown in the left and right panels, respectively. Constitutive RIM1 WT 18.76 ± 1.12 Hz, RIM1 KO 18.86 ± 1.46 Hz, RIM1/2 Flox 28.63 ± 1.87 Hz, and KO$_{PCP2}$ 28.72 ± 1.59 Hz. The bar graphs indicate means ± SEM. Statistical significance was tested by unpaired Student's t-test (* p < 0.05).

3.5.4 PCs of RIM4 KO$_{PCP2}$ mice exhibit an increased caffeine-sensitivity

Intraperitoneal injection of caffeine (25 mg/kg) induced an episode of motor impairment also in RIM4 KO$_{PCP2}$ mice, which was not observed in WT mice as well as in saline (10 ml/kg) injected RIM4 KO$_{PCP2}$ mice (Nesrine Melitti, unpublished data).

As it has been already shown that an application of 1 mM Caffeine reduced the firing rate of PCs in RIM4 KO$_{Const}$ mice (Fig. 3.6), I anticipated the same results in RIM4 KO$_{PCP2}$ mice. However, the similar results would tell us a different message, suggesting that the caffeine effect is not directly due to the reduced synaptic input on PCs and RIM4 is crucial for maintaining cellular excitability as RIM4 is only ablated in PCs in RIM4 KO$_{PCP2}$ mice. Therefore, I hypothesized that RIM4 might be involved in modulating intrinsic firing properties of PCs and the signaling deficit in PCs ultimately resulted in impaired motor coordination in RIM4 KO$_{PCP2}$ mice.

To answer this, I tested if caffeine application disturbs the intrinsic spontaneous spikes of PCs in RIM4 KO$_{PCP2}$ mice. As described previously in RIM4 KO$_{Const}$ mice (see section 3.3), spontaneous spikes of PCs were recorded juxtacellularly in both RIM4 WT$_{PCP2}$ and KO$_{PCP2}$ mice (4 WT$_{PCP2}$ and 4 KO$_{PCP2}$ mice) in the presence of synaptic blockers (20 µM CNQX and 10 µM Gabazine; Fig. 3.14.A). Interestingly, 1 mM caffeine reduced the mean firing rate in both RIM4 WT$_{PCP2}$ and KO$_{PCP2}$ mice (by 16% in RIM4 WT$_{PCP2}$ and by 44% in KO$_{PCP2}$; Fig. 3.14.B, E). However, whereas this reduction was not observed in WT$_{const}$ mice in the absence of the synaptic blockers (Fig. 3.6), a strong effect of caffeine on spiking was observed in RIM4 KO$_{PCP2}$ mice under these conditions (Fig. 3.14.E). Firing behavior was also analyzed by assessing histograms of ISIs as well as the auto-correlograms. While the spike regularity was unaltered in WT$_{PCP2}$ PCs showing comparable histograms of ISIs and peaks in auto-correlograms, RIM4 KO$_{PCP2}$ mice displayed an obvious change in the firing behavior (Fig. 3.14.C-D). A quantitative analysis showed that caffeine application in the presence of synaptic blockers in the bath decreased firing regularity in RIM4 KO$_{PCP2}$ mice showing a higher CV$_{ISI}$ value (Fig. 3.14.F).

In conclusion, the signaling deficit with regard to spontaneous firing spikes in PCs observed in RIM4 KO$_{const}$ mice was reproducible in RIM4 KO$_{PCP2}$ mice. In the absence of synaptic inputs, PCs in RIM4 KO$_{PCP2}$ mice are not able to maintain the spontaneous activity when caffeine is introduced.
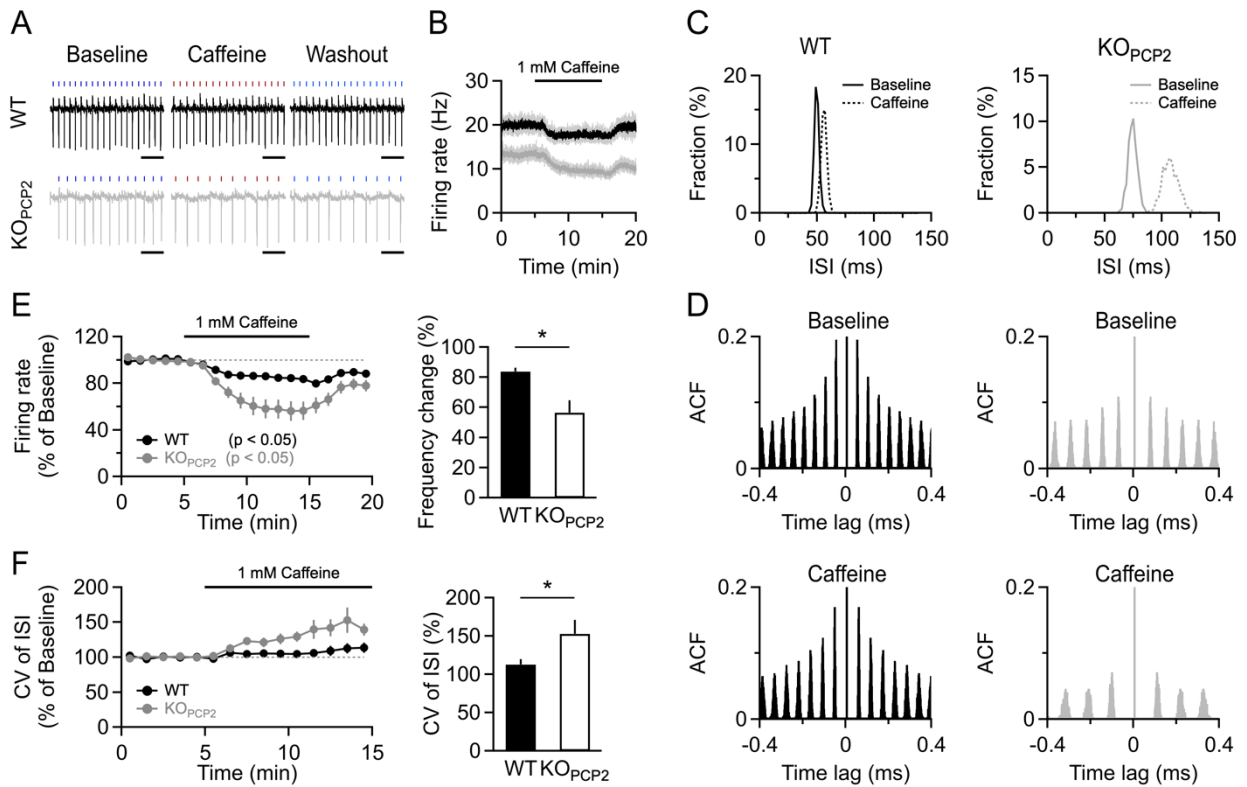
Figure 3.14: **A higher sensitivity to caffeine alters the spontaneous spike pattern in RIM4 KO$_{PCP2}$ mice**. A. Representative traces of spontaneous spikes before, during and after 1 mM caffeine application. The bars on top of each trace indicate the onset of each spike. Scale bars, 0.2 s. B. Representative time course of firing rate changes upon 1 mM caffeine application. C. Histograms of ISIs at baseline and after caffeine application. D. Autocorrelation in each condition showed changes in spike regularity during caffeine application in RIM4 KO$_{PCP2}$ mice. E. Changes in the firing rate after 1 mM caffeine application. Time course of the firing rate (left panel) and quantified frequency changes after 10 min of caffeine application (right panel, bar graph). RIM4 WT$_{PCP2}$ 83.73 ± 2.59 %, KO$_{PCP2}$ 55.49 ± 8.22 %. F. Changes in firing regularity quantified in CV$_{ISI}$ after 1 mM caffeine application. Time course of CVISI (left panel) and quantified CV$_{ISI}$ changes after 10 min of caffeine application (right panel, bar graph). RIM4 WT$_{PCP2}$ 112.8 ± 7.1 %, KO$_{PCP2}$ 152.8 ± 17.9 %. The bar graphs indicate means ± SEM. Statistical significance was tested by unpaired Student's t-test (* p < 0.05).

3.6 Functional role of RIM4 in the cerebellar circuit

Whereas the large RIM isoforms have a key role in the synaptic transmission as reported by multiple studies (Schoch et al., 2002; Fourcaudot et al., 2008; Han et al., 2011; Kaeser et al., 2011), the functions of the small RIM isoforms, especially RIM4, is not well understood yet. Unlike α- and β-RIMs, γ-RIMs are found not only in the presynaptic cytomatrix, but also in post-synapses, in dendrites and in soma (Alvarez-Baron et al., 2013). In addition to this finding, as our previous data suggested, RIM4 might play different

roles in the cerebellum especially in PCs rather than modulating synaptic transmission. A decreased dendritic tree size and a reduced spontaneous activity in PCs suggest that PCs without RIM4 might display an impaired intrinsic membrane property. To solve this puzzle, I investigated the novel function of RIM4 in PCs by electrophysiological recordings in RIM4 KO$_{PCP2}$ mice.

3.6.1 RIM4 has no critical role in presynaptic transmission unlike the large RIMs

As RIM is known to be important in synaptic transmission at the presynaptic AZ, I firstly examined whether the ablation of RIM4 altered synaptic transmission in PC synapses onto DCN. DCN are the hub in the cerebellum where the sole output of PCs is collected. The axons of PCs are travelling through the white matter of the cerebellum and their GABAergic inputs arrive at the DCN. Here, I performed whole cell voltage-clamp in DCN in acute cerebellar slices and characterized the synaptic GABA transmission at PC-DCN synapses in RIM4 WT$_{PCP2}$ and KO$_{PCP2}$ mice (4-6 weeks old; 11 WT$_{PCP2}$ and 7 KO$_{PCP2}$ mice).

Glutamatergic DCN (> 20 μm somatic diameter; Batini et al., 1992) were primarily selected and voltage clamped at -80 mV using recording electrodes containing high chloride internal solution (see 2.3.2). 5 μM QX-314 was added to the internal solution to block voltage-dependent sodium channels. The evoked inhibitory post-synaptic currents (eIPSCs) were recorded in the DCN by stimulating the PCs axons located at the white matter around the recorded DCN (100-300 μm distance from the soma) electrically using stimulating electrodes containing sACSF (Fig. 3.15.A). To isolate eIPSCs in the DCN, 20 μM CNQX and 100 μM APV were included in the bath sACSF. Paired-pulse stimulation, successive stimuli applied to a synapse at short time intervals, gives rise to either a presynaptic facilitation or depression of neurotransmitter release in response to the latter stimulus. This phenomenon, called short-term plasticity, is mediated primarily presynaptically. Hence, I applied paired-pulse stimuli spaced at 50 ms inter-spike interval to the PC axon fibers. Typically, GABAergic neurons have a high release probability, so that the response to the second stimulus is reduced compared to the first since the majority of synaptic vesicles were released by the first stimulus, and the interval is too short for the replenishment of the readily releasable pool. PC-DCN synapses in both RIM4 WT$_{PCP2}$ and KO$_{PCP2}$ mice showed a slight paired-pulse depression (PPD) and the mean

PPD values were similar (Fig. 3.15.B-C). Another approach to characterize the release probability is to monitor the magnitude of facilitation of the peak amplitude in a $[Ca^{2+}]_e$. Therefore, I measured the magnitude of facilitation in 4 mM $[Ca^{2+}]_e$ compared to 2 mM $[Ca^{2+}]_e$ in both RIM4 WT$_{PCP2}$ and KO$_{PCP2}$ mice (7 WT$_{PCP2}$ and 5 KO mice). These measurements showed that the amplitude of the first peaks was increased approximately by two-fold in both RIM4 WT$_{PCP2}$ and KO$_{PCP2}$ mice (Fig. 3.15.D), yet there was no difference between the two groups (Fig. 3.15.E).

Besides synaptic plasticity at PC-DCN synapses, I analyzed the input and output level in one of the major glutamatergic synapses onto PCs. I found that the release probability at CF-PC synapses in RIM4 KO$_{const}$ mice was also unchanged showing comparable PPR values (Fig. 3.8.E).

Taken together, this data demonstrates that the release probability in PC-DCN and CF-PC synapses was not altered in RIM4 KO$_{PCP2}$ mice indicating that RIM4 is not involved in regulating basal synaptic transmission in contrast to RIM1 and RIM2.
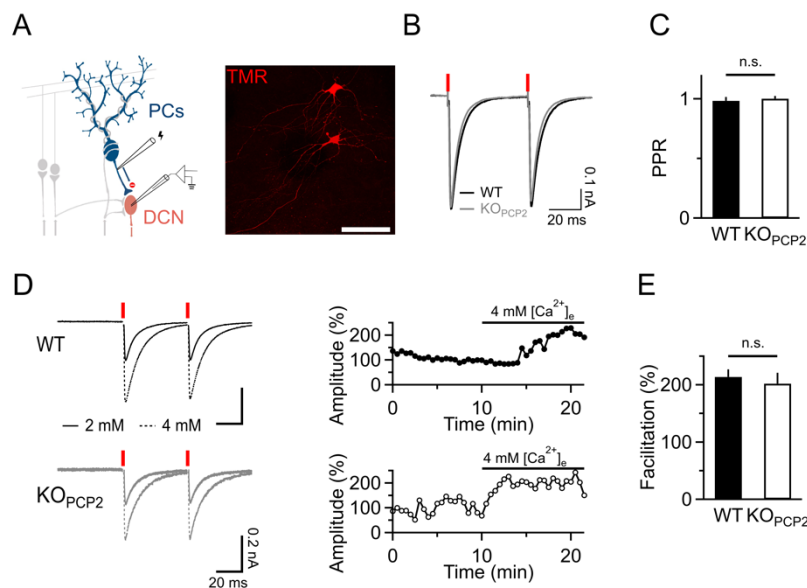

Figure 3.15: **Unchanged GABA release at PC-DCN synapses in RIM4 KO$_{PCP2}$ mice.** A. Schematic depiction of the recording set-up and representative scan showing recorded DCN neurons labelled with red fluorescence dye, TMR, via a patch pipette. Scale bar, 100 µm. B. Representative traces showing stereotypical paired-pulse depression at PC-DCN synapses in both RIM4 WT$_{PCP2}$ and KO$_{PCP2}$ mice. C. Unchanged paired-pulse ratio. RIM4 WT$_{PCP2}$ 0.98 ± 0.03, KO$_{PCP2}$ 1.00 ± 0.02. D. Representative traces showing the impact of increasing the extracellular calcium concentration (left panel, 2 mM solid line, 4 mM dash lines) and corresponding time course of amplitude change (right panel) in RIM4 WT$_{PCP2}$ and KO$_{PCP2}$ mice. E. A higher extracellular calcium level facilitated the amplitude of both RIM4 WT$_{PCP2}$ and KO$_{PCP2}$ mice. RIM4 WT$_{PCP2}$ 213.8 ± 13.2 %, KO$_{PCP2}$ 202.1 ± 18.9 %.

The bar graphs indicate means ± SEM. Statistical significance was tested by unpaired Student's t-test (* $p < 0.05$).

3.6.2 RIM4 KO$_{PCP2}$ mice show a broadened action potential of Purkinje cells

The results from the PC spike recordings demonstrated a signaling deficit in overall output and in intrinsic electrophysiological properties of PCs. Previously, a screen for novel interaction partners of RIM4 in the central nervous system had been performed, and it was found that 21% of the binding partners were proteins regulating vesicle trafficking (K. Michel, Dissertation, 2015). Taken together, I hypothesized that RIM4 might be involved in either the trafficking of channels into dendrites or their function. To test this, I examined if the ablation of RIM4 had an impact on the functions of several channels that are highly expressed in PCs and which have been associated to ataxia (reviewed in Hoxha et al., 2018).

Neurons fire an action potential (AP) and the waveform of an AP is driven by voltage-gated sodium channels (VGSCs, Na$_v$ channels) and voltage-gated potassium channels (VGKCs, K$_v$ channels) (Hodgkin and Huxley, 1939). Hence, investigating the waveform of APs was the first step to understand the intrinsic excitability of PCs in RIM4-deficient mice. To this end, I performed whole cell current clamp in PCs to record spontaneous APs at resting membrane potential (-60 mV) in RIM4 WT$_{PCP2}$ and KO$_{PCP2}$ mice (7 WT$_{PCP2}$ and 6 KO mice; 10 and 8 cells respectively). To characterize the waveform of APs, I analyzed the peak amplitude, the amplitude of fAHP, and the full width of APs. Overall, both RIM4 WT$_{PCP2}$ and KO$_{PCP2}$ mice showed the typical shape of APs: rapid rise, falling, undershoot, and refractory period (Fig. 3.16.A). The average peak amplitude was not changed while the amplitude of fAHP was significantly larger in RIM4 KO$_{PCP2}$ mice compared to WT$_{PCP2}$ (Fig. 3.16.B-C). RIM4 KO$_{PCP2}$ mice display a significantly larger AP width (Fig. 3.16.D). These results suggested that the absence of RIM4 in PCs might affect the function of K$_v$ channels.
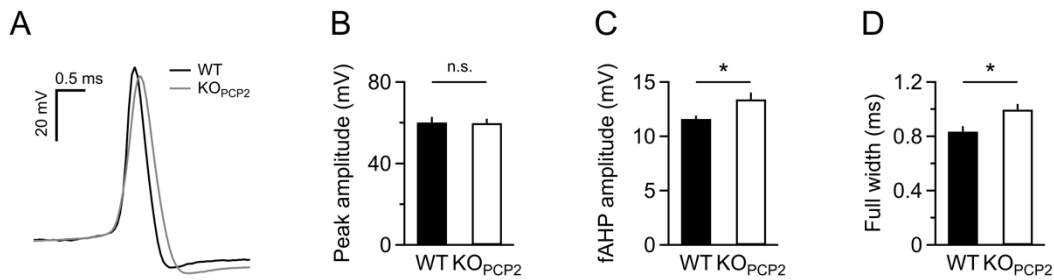
Figure 3.16: **Action potentials in RIM4 KO$_{PCP2}$ mice show a broadened wave form.** A. Representative traces of APs recorded in RIM4 WT$_{PCP2}$ and KO$_{PCP2}$ mice. B. The average peak amplitude was unchanged. RIM4 WT$_{PCP2}$ 60.2 ± 2.7 mV, KO$_{PCP2}$ 59.8 ± 2.2 mV. C. The average amplitude of fAHP was higher in RIM4 KO$_{PCP2}$ mice. RIM4 WT$_{PCP2}$ 11.6 ± 0.3 mV, KO$_{PCP2}$ 13.4 ± 0.6 mV. D. The average full width of an AP was increased in RIM4 KO$_{PCP2}$ mice. RIM4 WT$_{PCP2}$ 0.84 ± 0.04 ms, KO$_{PCP2}$ 1.0 ± 0.04 ms. The bar graphs indicate means ± SEM. Statistical significance was tested by unpaired Student's t-test (* p < 0.05).

3.6.3 KCND3 channels are not fully functional in RIM4 KO$_{PCP2}$ mice

Functional ion channels are very important to maintain the firing properties of neurons and mutations of ion channels often alter intrinsic membrane properties. In many ataxia studies, it has been revealed that various mutations in ion channels affect signaling of PCs and are the cause for ataxic phenotypes (Hoxha et al., 2018). In PCs, K$_v$4.3 channels, the only K$_v$4 subunit expressed in PCs, are the major source of the subthreshold inactivating K$^+$ currents, and mutations of the gene encoding K$_v$4.3 cause spinocerebellar ataxia-19 (Serôdio and Rudy, 1998; Duarri et al., 2012). Blocking of the K$_v$4.3 channels with Mefloquine, a well-known antimalarial drug as well as a potassium channel blocker, resulted in broaden APs in the rat right ventricular myocytes (Perez-Cortes et al., 2015). In the transcriptomics and proteomics data comparing RIM4 WT$_{const}$ versus KO$_{const}$, K$_v$4.3 (KCND3) showed slight changes in the cerebellar tissue of RIM4 KO$_{const}$ mice (Eva Schönhense, unpublished data). Therefore, I tested if the blocking of K$_v$4.3 channels altered the waveform of APs in PCs and if the absence of RIM4 in PCs affected Kv4.3 channels.

Whole cell current-clamp was performed in both RIM4 WT$_{PCP2}$ and KO$_{PCP2}$ mice (4-6 weeks old, 4 WT$_{PCP2}$ and 3 KO$_{PCP2}$ mice; 12 and 10 cells respectively). APs were recorded by injecting short currents every 30 second and PCs were clamped at -70 mV to avoid spontaneous spikes. After 5-10 minutes of baseline recording, 50 µM of Mefloquine was bath applied for 10 minutes. The AP width was measured from the first AP in each

recording, and the effect of blocking was calculated by comparing the average values from 3-5 successive recordings. Compared to the run-down test results without alterations in AP width, Mefloquine application resulted in a broadening AP waveform in PCs of WT_{PCP2} mice (Fig. 3.17). In contrast, the AP full width was not significantly changed after Mefloquine application in RIM4 KO_{PCP2} mice. In short, $K_v4.3$ channels in RIM4 KO_{PCP2} mice might not be functional as blocking of the $K_v4.3$ channels had no effect in these mice suggesting the broader AP waveform of RIM4-deficient in PCs affected the function of $K_v4.3$ channels resulting in a broadened AP waveform.
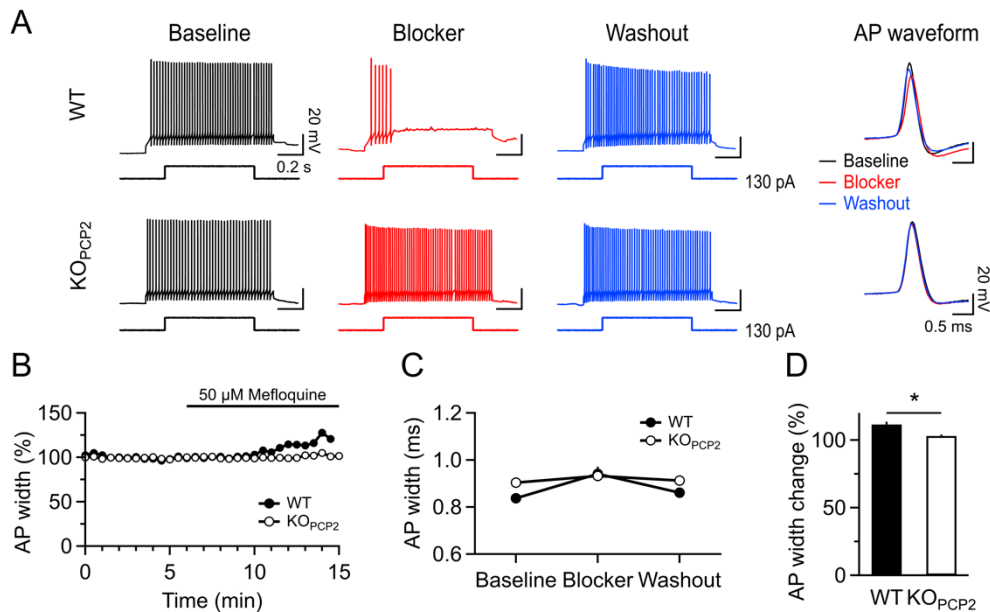

Figure 3.17: **Blocking of KCND3 channels changes the action potential waveform only in WT mice.** A. Representative experiments in RIM4 WT_{PCP2} and KO_{PCP2} mice showing the effect of the KCND3 blocker, Mefloquine, on the AP waveform. APs were evoked by a brief current injection (130 pA for 1 s). The first AP in each recording was aligned and depicted on the right panel. B. A time course of AP width from the exemplary experiments showed an increased AP width in the RIM4 WT_{PCP2} mouse without changes in the KO_{PCP2} mouse when 50 μM Mefloquine was bath applied. C. The average AP width was measured in each condition in RIM4 WT_{PCP2} and KO_{PCP2} mice showing a significant change in RIM4 WT_{PCP2} mice. RIM4 WT_{PCP2} 0.84 ± 0.02 ms at Baseline, 0.94 ± 0.03 ms with Blocker, 0.86 ± 0.02 ms after washout; RIM4 KO_{PCP2} 0.9 ± 0.02 ms at Baseline, 0.93 ± 0.02 ms with Blocker, 0.91 ± 0.02 ms after washout. Statistical significance was tested by paired Student's t-test ($p < 0.05$). D. The effect of Mefloquine on AP width was calculated in percentage by normalizing the AP width to the baseline. RIM4 WT_{PCP2} 111.5 ± 2.0 %, KO_{PCP2} 103.0 ± 1.1 %. The bar graphs indicate means ± SEM.

3.6.4 RIM4 KO$_{PCP2}$ mice show an altered shape of complex spikes

Strong excitatory inputs delivered by CFs trigger the generation of CSs in PCs. CS is a unique spike in PCs that is composed of an initial Na$^+$ spike followed by high frequency spikelets (Eccles et al., 1996). In many ataxia models, such as mouse models of SCA1, SCA7, SCA14 and SCA23, CF signaling is drastically altered (Ebner et al., 2013; Smeets and Verbeek, 2016). Unlike short APs, the waveform of CSs displays prolonged depolarization with several small spikelets, and a study showed that Kv3.3 channels are important for the generation of CS waveforms (Zagha et al., 2008).

In order to evaluate the properties of PC encoding of synaptic inputs from CFs, I performed whole cell current-clamp in PCs (clamped at -60 mV) and recorded CSs evoked by electrical stimulation in RIM4 WT$_{PCP2}$ and KO$_{PCP2}$ mice (9 WT$_{PCP2}$ and 9 KO$_{PCP2}$ mice; 14 cells each). An antidromic AP was neglected for further analysis as it was delivered by activation of PC axons. In both groups, CSs were evoked in an "all-or-none" way showing a typical waveform without changes in amplitude upon stimulation intensity (Fig. 3.18.A). The peak amplitude of the initial spike was not different in RIM4 KO$_{PCP2}$ mice (Fig. 3.18.B). The coast-line index that reflected the magnitude of postsynaptic outputs was measured in 15 ms duration from the onset of the initial peak containing the rest of the spikelets, and it was significantly decreased in RIM4 KO$_{PCP2}$ mice (Fig. 3.18.C). The number of spikelets defined as a greater increase than 5 mV after the initial Na$^+$ spike within the measured coast-line was counted and it was drastically reduced in RIM4 KO$_{PCP2}$ mice compared to WT$_{PCP2}$ mice (Fig. 3.18.D). As a conclusion, I observed an altered output of PCs resulting from the activation of CFs in RIM4-deficient mice and it might be due to disturbed K$_v$3.3 channels as it was reported in Zagha et al., 2008.

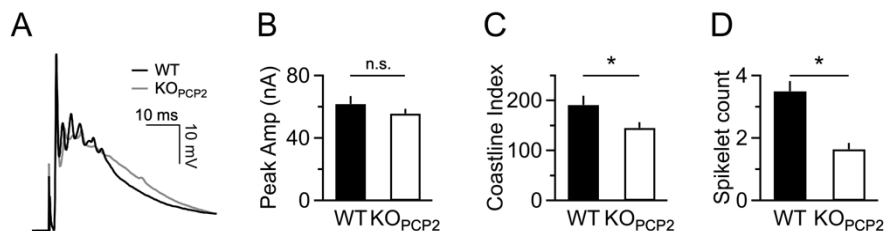**Figure 3.18**: **Altered CS waveforms in RIM4 KO$_{PCP2}$ mice.** A. Representative traces of CSs in RIM4 WT$_{PCP2}$ and KO$_{PCP2}$ mice. B. The average peak amplitude was unchanged. RIM4 WT$_{PCP2}$ 61.8 ± 5.1 mV, KO$_{PCP2}$ 55.8 ± 3.0 mV. C. The average Coastline Index measured in 15 ms duration from the onset of the initial spike was decreased in RIM4 KO$_{PCP2}$ mice. RIM4 WT$_{PCP2}$ 191.6 ± 18.3, KO$_{PCP2}$ 145.6 ± 11.3. D. The average number of spikelets defined as a spike greater than 5 mV after the initial spike during the

depolarized period was reduced drastically in RIM4 KO$_{PCP2}$ mice. RIM4 WT$_{PCP2}$ 3.5 ± 0.3, KO$_{PCP2}$ 1.6 ± 0.2. The bar graphs indicate means ± SEM. Statistical significance was tested by unpaired Student's t-test (* $p < 0.05$).

3.6.5 Aberrant innervation of CFs in RIM4 KO$_{PCP2}$ mice

PCs receive two major glutamatergic inputs, from CFs and PFs, and the way how these fibers innervate to PCs are distinct (Fig. 3.19.A). In the cerebellum, CFs and PFs can be distinguished by immunohistochemistry as they express different vesicular glutamate transporters (Vglut): Vglut1 in PFs and Vglut2 in CFs (Lorenzetto et al., 2009). Therefore, I labeled PF- and CF-PC synapses in RIM4 WT$_{PCP2}$ and KO$_{PCP2}$ mice by Vglut1 and Vglut2 staining and measured the density of these synapses along the ML (Fig. 3.19.B; see also 2.5.3). As a result, no clear difference was found in PFs between groups (Fig. 3.19.C). No signs of somatic innervations of CFs were observed in any of the mice (Fig. 3.19.D). However, the distribution of CF-PC synapses obviously differed in the RIM4 KO$_{PCP2}$ mice showing more abundant proximal innervations of CFs while the total density of Vglut2 puncta along the ML remained same (Fig. 3.19.E-F).
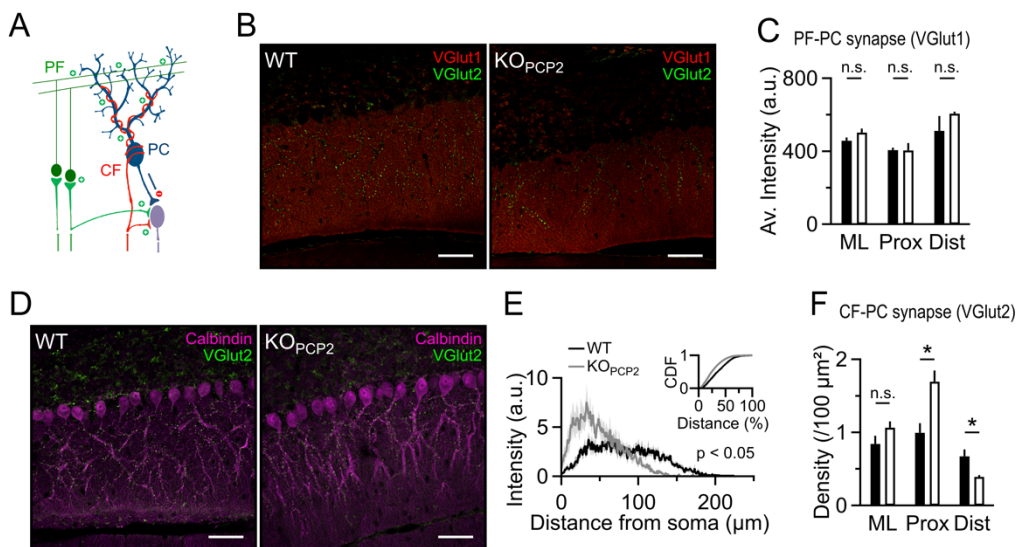

Figure 3.19: **Increased proximal distribution of CF-PC synapses in RIM4 KO$_{PCP2}$ mice.** A. Schematic drawing depicting a cerebellar circuit containing PF- and CF-PC synapses. B. Representative scans from Vglut1 (red) and Vglut2 (green) stained cerebellar slices of RIM4 WT$_{PCP2}$ and KO$_{PCP2}$ mice. scale bars = 50 μm. C. The average intensity in each region, such as ML, proximal (Prox) and distal (Dist) region of ML was unchanged. RIM4 WT$_{PCP2}$ 458.0 ± 17.4 in ML, 406.5 ± 13.5 in Prox, 512.0 ± 81.4 in Dist; KO$_{PCP2}$ 502.6 ± 21.9 in ML, 405.2 ± 40.0 in Prox, 606.1 ± 10.6 in Dist. D. Representative scans of Calbindin (magenta) and Vglut2 (green) stained cerebellar tissue in RIM4 WT$_{PCP2}$ and KO$_{PCP2}$ mice. scale bars = 50 μm. E. Intensity line profiles showed an increased

distribution of CF-PC synapses in RIM4 KO$_{PCP2}$ mice (gray) compared to WT$_{PCP2}$ mice (black). A cumulative distribution of CF-PC synapses aligned to their relative location from the soma is shown in the subpanel. Statistical significance was tested by Kolmogorov-Smirnov test ($p < 0.05$). F. The average density of fluorescence intensity was compared in each region showing a higher density in Prox but a lower density in Dist in RIM4 KO$_{PCP2}$ mice. RIM4 WT$_{PCP2}$ 0.8 ± 0.1 in ML,1.0 ± 0.1 in Prox, 0.7 ± 0.1 in Dist; KO$_{PCP2}$ 1.1 ± 0.1 in ML, 1.7 ± 0.2 in Prox, 0.4 ± 0.02 in Dist. The bar graphs indicate means ± SEM. Statistical significance was tested by unpaired Student's t-test (* $p < 0.05$).

3.6.6 mGluR1-dependent signaling deficit is observed in RIM4 KO$_{PCP2}$ mice

PFs relay excitatory inputs on PCs with glutamate release. Repetitive activation of PFs can result in spill-over of glutamate, thereby and activating mGluR1 which is a G-protein coupled receptor strongly expressed in PCs outside the postsynaptic density (Batchelor et al., 1994). It has also been reported that mutant mice lacking mGluR1 develop impaired motor coordination, deficient LTD as well as an impaired motor learning (Aiba et al., 1994; Ichise et al., 2000). Therefore, I investigated if mGluR1-dependent signaling was altered in RIM4-deficient mice. DHPG is a selective group I mGlu receptor agonist. I analyzed the effects of DHPG on spontaneous spikes in PCs using RIM4 WT$_{PCP2}$ and KO$_{PCP2}$ mice (8 WT and 5 KO mice; 31 and 15 cells respectively). Spontaneous spikes of PCs were recorded as described previously (see 3.2) in the presence of synaptic blockers (20 µM CNQX and 10 µM Gabazine) and 20 µM DHPG were applied for 6-10 minutes. Interestingly, activation of mGluR1 resulted in increased firing rates in WT$_{PCP2}$ PCs in two steps (Fig. 3.20.A): primary effect (Pri, increased firing rate approximately 240% compared to baseline, Base) and secondary effect (Sec, a rhythmical bursting). The primary effect preceded in all recordings and increased firing frequency while the spikes remained very regular as it was shown in low CV$_{ISI}$ values, the histograms of ISI and Auto-correlogram (Fig. 3.20.A-C). The following secondary effect was clearly distinct in spike behaviors. In the presence of DHPG, regular spikes suddenly turned into burst firing which showed a stronger increase in firing rate (around 400%) and exhibited bursts of several spikes (Fig. 3.20.A). In the bursting period, CV$_{ISI}$ values were much higher than those of regular spikes at the baseline, and the spikes were rhythmical showing relatively regular inter-bursting intervals that were noticeable in Auto-correlogram (Fig. 3.20.C). The primary effect on spontaneous spikes was similar, showing increased firing rates while regularity was unchanged (Fig. 3.20.D-E). Surprisingly, however, the rhythmical bursting was

completely absent in PCs of RIM4 KO$_{PCP2}$ mice (Fig. 3.20.F). In RIM4 KO$_{PCP2}$ mice, DHPG application resulted in either silence or tonic firing of PCs (Fig. 3.20.A).

Additionally, I tested the effect of DHPG on the spontaneous firing spikes of PCs in RIM1 and RIM2 lacking mice. Unlike RIM4 KO$_{PCP2}$ mice, the ablation of RIM1/2 in PCs did not affect the mGluR1-dependent signaling. An increased firing rate and spike regularity by DHPG application was similar to RIM1/2 and RIM4 WT$_{PCP2}$ mice (Fig. 3.20.D). More importantly, application of DHPG induced bursting spikes in PCs without RIM1/2 (Fig. 3.20.F).

Taken together, I conclude that RIM4 is a key regulator of multiple channels and receptors in PCs maintaining the somato- and dendritic-excitability of PCs.
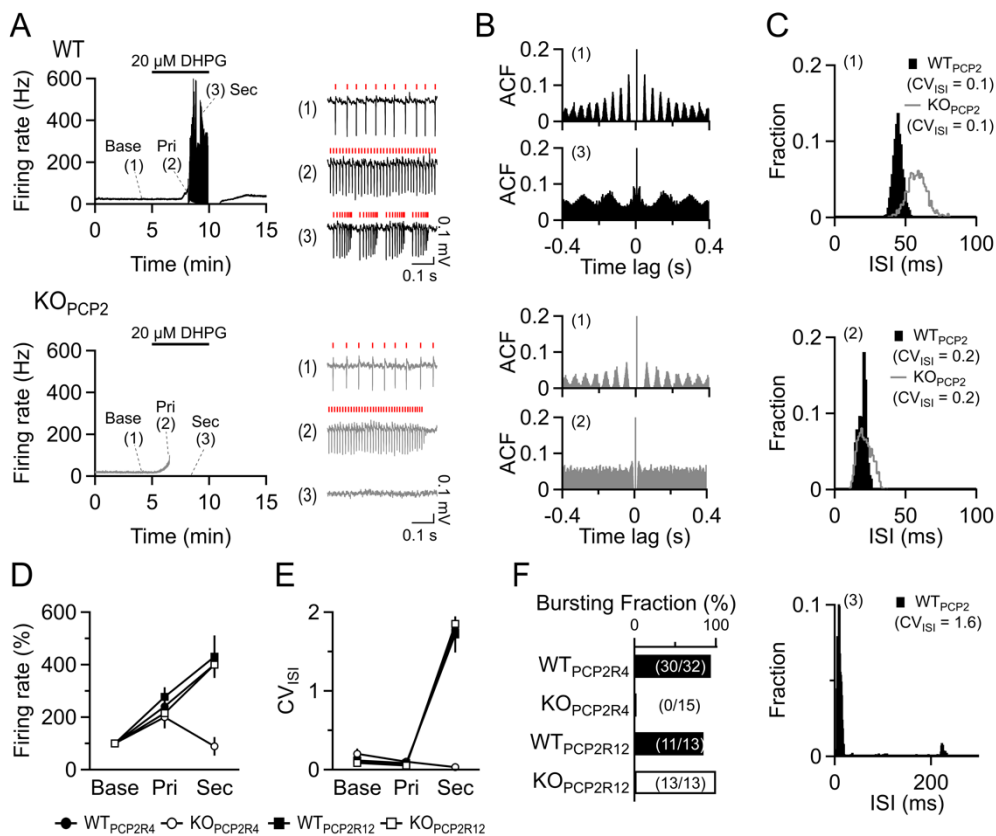

Figure 3.20: **RIM4 KO$_{PCP2}$ mice show a mGluR1-dependent signaling deficit.** A. Representative experiments with a time course of the firing rate and an exemplary trace for each phase: baseline (Base), primary effect (Pri), and secondary effect (Sec). Bath application of 20 µM DHPG induced an increase in the firing rate in two steps. Red bars on the right panel indicate the onset of individual spikes. B. Auto-correlograms in each condition displaying spike regularity. C. Histograms of ISIs were generated and CV$_{ISI}$ in each phase was calculated. D-E. The mean firing rate as well as CV$_{ISI}$ in each step were measured and normalized to the baseline in RIM4 WT$_{PCP2}$ and KO$_{PCP2}$ and in RIM1/2 WT$_{PCP2}$ and KO$_{PCP2}$ mice. RIM4 WT$_{PCP2}$ 240.9 ± 43.4 % and 0.06 ± 0.01 in Pri, 400.3 ±

33.4 % and 1.78 ± 0.08 in Sec; RIM4 KO$_{PCP2}$ 199.7 ± 42.4 % and 0.10 ± 0.02 in Pri, 88.9 ± 35.6 % and 0.03 ± 0.01 in Sec; RIM1/2 WT$_{PCP2}$ 277.6 ± 36.9 % and 0.08 ± 0.02 in Pri, 430.8 ± 81.3 % and 1.72 ± 0.23 in Sec; RIM1/2 KO$_{PCP2}$ 215.2 ± 14.5 % and 0.09 ± 0.01 in Pri, 400.3 ± 43.7 % and 1.85 ± 0.07 in Sec. F. The number of bursting PCs at the second phase was counted in each group. RIM4 WT$_{PCP2}$ 93.75 %, RIM4 KO$_{PCP2}$ 0 %, RIM1/2 WT$_{PCP2}$ 84.6 %, and RIM1/2 KO$_{PCP2}$ 100 %.

3.7 Delivery of RIM4 in PCs via AAV injections rescues the excitability of PCs in RIM4 deficient mice at the cellular level

Ablation of RIM4 in PCs resulted in a reduced dendritic arborization and a disturbed spontaneous activity. To verify if these alterations are directly caused by the absence of RIM4 in PCs or an indirect consequence of signaling deficit in PCs, I delivered AAV viral particles expressing RIM4 to RIM4-deficient PCs (Fig. 3.21). Custom-designed AAV constructs were used containing a mRFP-T2A-Flag-RIM4 cassette and a construct coding for mRFP without RIM4 was used as control (Fig. 3.21.A). *In vivo* AAV injections were performed at two different time points, at postnatal day 0 (P0) and at 12 weeks, to test for developmental effects (Fig. 3.21.B). The cerebellar vermis Lobules IV-VI were targeted, and the expression of the viral construct was monitored by the level of mRFP expression in PCs (Fig. 3.21.C). I compared the effect of RIM4 delivery in PCs between 4 experimental groups (see 2.8 and Table 3): WT, OE, KO, and RIM4 expressing cells in RIM4 KO PCs (Rescue). During the experiments and analysis, I was blind to their genotype, and it was only revealed once the analysis was fully performed.

As a reduced dendritic arborization in PCs was one of the key findings in RIM4 lacking mice, PCs with a high level of mRFP expression were labeled by whole cell patch clamping using an electrode containing a green-fluorescent dye (Alexa 488, 500 µM) in the internal solution (see 2.8). To examine dendritic arborization, the dendritic tree area was measured by drawing an outline of the PC tree. Delivery of RIM4 to the neonatal cerebellum in RIM4 KO mice fully restored the dendritic morphology (Fig. 3.22.A-B). Unlike the result from P0 rescue experiments, altered dendritic arborization of PCs remained even though RIM4 was introduced in the adult RIM4 KO mice (Fig. 3.22.C-D). These results indicate that the alterations in the dendritic tree of PCs caused by the absence of RIM4 during development cannot be reversed by RIM4 after maturation. Therefore, the expression and function of RIM4 during the developmental stage is critical

for the establishment of PC morphology and this RIM4-dependent process cannot be re-initiated after maturation.

Next, I addressed the question if the delivery of RIM4 in the adult stage could rescue PC activity. To probe this, spontaneous spikes of PCs expressing mRFP were recorded extracellularly as described previously (see 3.2 and 3.3). Interestingly, the firing property was comparable to WT in PCs when RIM4 was re-introduced in RIM4 deficient PCs (Fig. 3.22.A). Also, the firing behavior induced by 1 mM caffeine bath application remained similar to the WT level (Fig. 3.22.B). More surprisingly, bursting PCs were restored in the RIM4 rescue group (Fig. 3.22.C-F).

In summary, these data suggest that RIM4 is necessary during the developmental period to maintain the full dendritic arbors of PCs and modulation of PC excitability, and could acutely be involved.
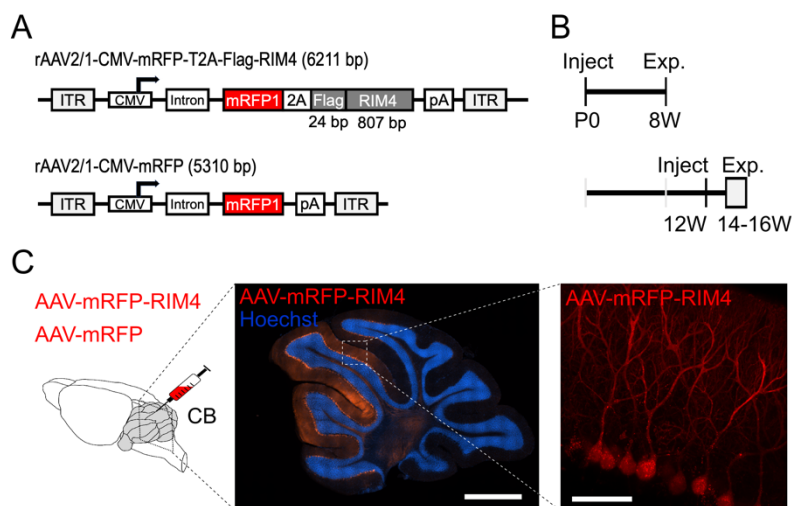

Figure 3.21: **Strategy to deliver RIM4 to RIM4-lacking PCs.** A. Schematic depiction of the AAV constructs containing either the mRF-RIM4 (rAAV2/1-CMV-mRFP-T2A-Flag-RIM4) or the mRFP (rAAV2/1-CMV-mRFP) cassette. B. Delivery of AAV viral particles was performed at two time points, postnatal day 0 (P0) and at 12 weeks old. Experiments were performed after a couple of weeks in adult mice and for 8 weeks for newborns to allow for maximal protein expression and function. C. A schematic depitction of injection sites in the cerebellum (left panel) and representative scans showing PCs highly expressing mRFP (right panel). Scale bars 500 µm and 50 µm.
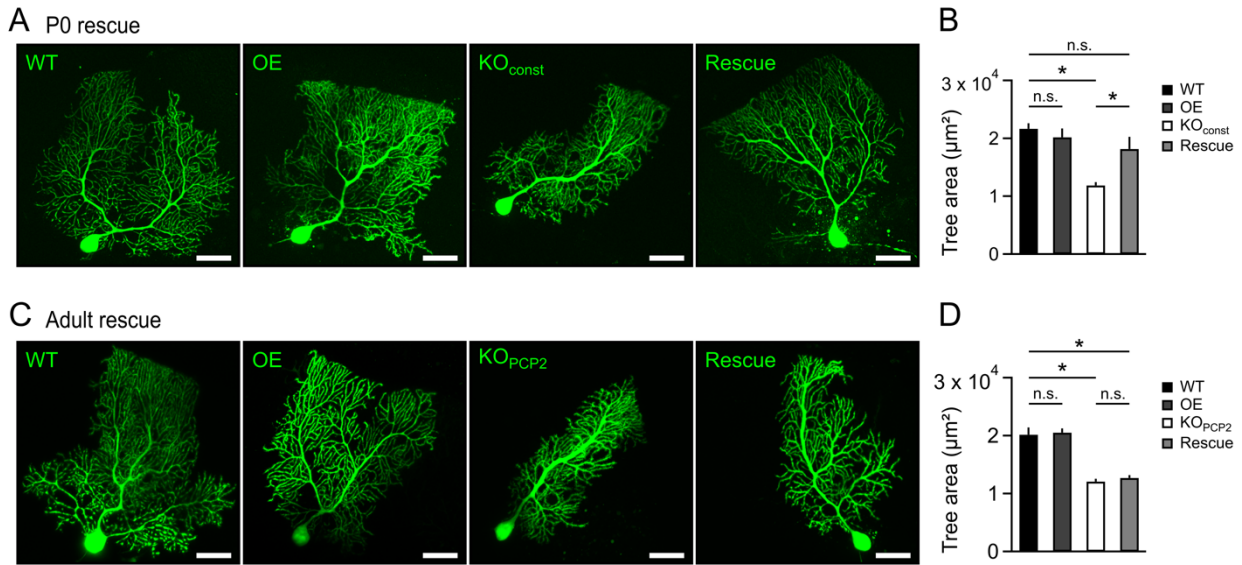
Figure 3.22: **Rescue of PC dendritic arborization.** A. Representative scans of PCs labeled with a green-fluorescent dye, 500µM Alexa 488, in each group of P0 rescue experiments. B. The average PC tree area showed normal dendritic morphology after RIM4 delivery into RIM4 deficient PCs. WT $2.2 \pm 0.1 \times 10^4$ µm^2; OE $2.0 \pm 0.2 \times 10^4$ µm^2; KO $1.2 \pm 0.1 \times 10^4$ µm^2; Rescue $1.8 \pm 0.2\ 0.1 \times 10^4$ µm^2. C. Representative scans of labeled PCs in each group of the adult rescue experiments. D. The average tree area revealed no restoration of dendritic arborization when RIM4 was deliverd to the brain at the late time point into the RIM4 KO. WT $2.0 \pm 0.1 \times 10^4$ µm^2; OE $2.1 \pm 0.1 \times 10^4$ µm^2; KO $1.2 \pm 0.1 \times 10^4$ µm^2; Rescue $1.3 \pm 0.1\ 0.1 \times 10^4$ µm^2. The bar graphs indicate means ± SEM. Statistical significance was tested by unpaired Student's t-test (* $p < 0.05$).
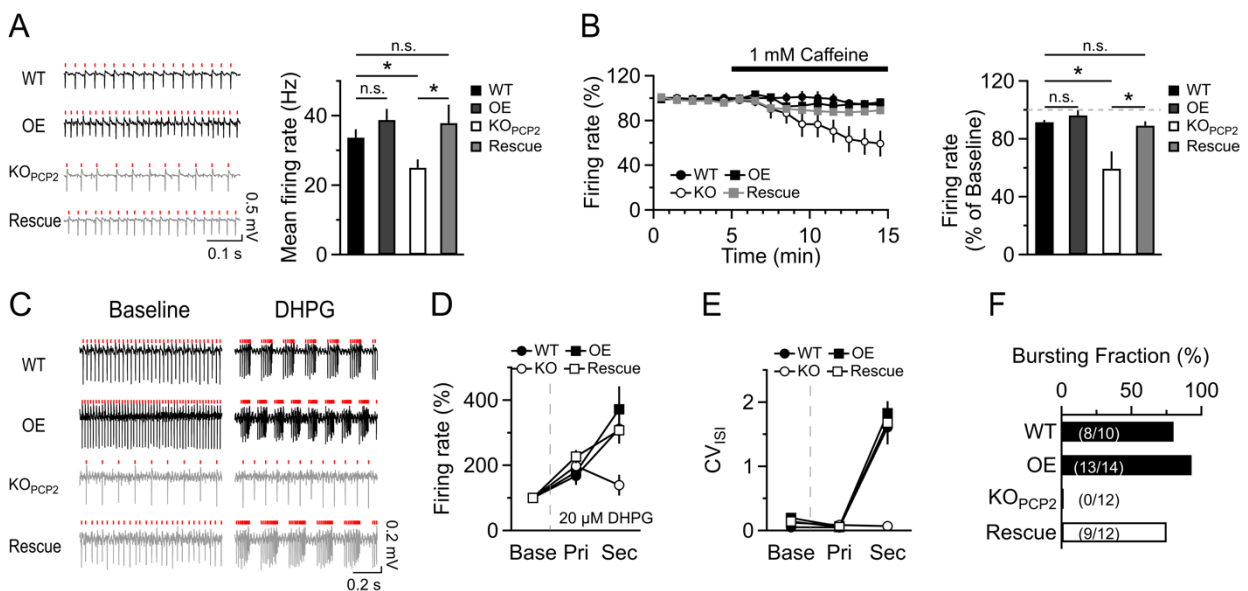

Figure 3.23: **Delivery of RIM4 can reverse the abnormal firing properties of RIM4 ablated PCs.** A. Representative traces in each group (left panel). The mean firing rate was increased in the rescue group compared to PCs without RIM4. WT 33.7 ± 2.4 Hz; OE

38.8 ± 3.2 Hz; KO 25.0 ± 2.4 Hz; Rescue 37.9 ± 5.3 Hz. B. The average time course and firing rate upon 1 mM caffeine bath application showed a fully rescued phenotype. WT 91.1 ± 1.5 %; OE 96.3 ± 3.7 %; KO 59.4 ± 12.0 %; Rescue 89.2 ± 2.9 %. C. Representative spike traces in each group at baseline and after 20 μM DHPG application. D-E. The average changes in firing rate and CV_{ISI} in each group upon DHPG bath application. WT 167.9 ± 19.0 % and 0.1 ± 0.01 CV_{ISI} in Pri, 311.8 ± 45.6 % and 1.6 ± 0.3 CV_{ISI} in Sec; OE 179.6 ± 39.5 % and 0.1 ± 0.02 CV_{ISI} in Pri, 371.8 ± 70.8 % and 1.8 ± 0.2 CV_{ISI} in Sec; KO 197.9 ± 19.7 % and 0.1 ± 0.03 CV_{ISI} in Pri, 139.1 ± 31.9 % and 0.1 ± 0.02 CV_{ISI} in Sec; Rescue 226.9 ± 20.2 % and 0.1 ± 0.01 CV_{ISI} in Pri, 307.5 ± 38.0 % and 1.7 ± 0.3 CV_{ISI} in Sec. F. The number of bursting PCs at the second phase was counted in each group. WT 80 %, OE 92.9 %, KO 0 %, and Rescue 75 %. The bar graphs indicate means ± SEM. Statistical significance was tested by unpaired Student's t-test (* $p < 0.05$).

4. Discussion

The full-length RIM family members, RIM1 and RIM2, are known to be important for modulating synaptic transmission at the AZ (reviewed in Südhof, 2012). However, the role of the small RIM isoforms, RIM3 and RIM4, in the central nervous system are still not understood in detail. Surprisingly, mice without RIM4 in all cells develop episodes of strong motor impairment. Selective ablation of RIM4 in Purkinje cells results in a similar phenotype which is not observed in mice lacking RIM4 in either the neocortex and hippocampus, or the inferior olive or mice without RIM1/2 in cerebellar PCs. In this study, I've demonstrated that RIM4 is important for maintaining neuronal arborization and intrinsic electrophysiological properties of PCs, thereby modulating cerebellar output. Together, the data presented in this thesis indicates that in contrast to the long RIM variants RIM4 is essential to ensure normal motor behavior by a mechanism different from the regulation of synaptic transmission.

4.1 RIM4 is crucial for preserving the integrity of the cerebellar circuit

A normal dendritic arborization of neurons is very important to maintain their electrophysiological properties, and a disturbed neuronal morphology can severely impact membrane properties and synaptic connections (reviewed in McAllister, 2000). A dysmorphic change in the cerebellum, especially a reduced dendritic arborization of PCs, is one of the key cellular pathologies found in RIM4 lacking mice (Fig. 3.2). Degeneration of PCs has been reported in multiple ataxia studies, especially in SCA mouse models (reviewed in Zoghbi and Orr, 2009). For instance, KO mice of *SUN1*, a gene encoding a protein directly coupled to the cytoskeleton, show a reduction of cerebellar volume by 25% and of the number of PCs by 33% and develop an impaired motor coordination (Wang et al., 2015). The *ANKFY1* mutant mice, a gene encoding protein involved in vesicle transport (Kuriyama et al., 2000), display a drastic reduction in PC density and in their dendritic arbors, and exhibit body weight loss and motor deficits (Ding et al., 2017). The loss of *TMEM30A*, a gene related to the transport of phospholipids, in PCs results in cerebellar atrophy, such as a PC degeneration and a reduced ML thickness, and in cerebellar ataxia (Yang et al., 2018). Unlike these reports, mice without RIM4 in PCs do not exhibit any hallmarks of degeneration (Fig. 3.1.F and 3.12.F). *Tottering* mice which

show the phenotype most similar to our model also do not develop PC degeneration but exhibit a reduced cerebellar volume and thickness of the ML (Isaacs and Abbott, 1995). The onset of these abnormalities in cerebellar morphology is around 3 weeks old when the *tottering* mice develop ataxic phenotype. This timeline of the episode's occurrence is also very similar to our mouse model. The analysis of several ataxic mouse model provided evidence that an impaired motor function can occur prior to PC degeneration (Shakkottai et al., 2011; Jayabal et al., 2015). Together these findings suggests that neurodegenerative phenotypes are mostly found in chronic ataxia models but not in many episodic ataxia models. A dysfunction in PC activity is strongly linked to the development of an ataxic phenotype in mice in addition to cerebellar atrophy. This link will be further discussed in the following section.

Although RIM4 was deleted specifically in PCs, CF-PC synapses were also affected, showing a more abundant proximal distribution without changes in the overall number of CF-PC synapses (Fig. 3.19). This phenomenon has been also reported in the *ducky* mouse, another ataxic mouse model which is caused by a mutant in *CANCA2D2* gene, encoding an auxiliary $\alpha 2\delta 2$ subunit of VGCCs (Beeson et al., 2020). The observed differential distribution of CF-PC synapses might be predominantly due to reduced dendritic arbors in the PCs of RIM4 KO mice. Delivery of RIM4 in the cerebellum of neonatal RIM4 KO mice restored the dendritic arbors of PCs while it did not rescue this phenotype when reintroduced into the adult brain (Fig. 3.22). These results suggest an important role of RIM4 in the regulation of dendritic growth during the developmental stage. During the early developmental stage, PCs undergo the process of synapse elimination in order to achieve the mono-innervation of CFs (reviewed in Kano et al., 2018). In the earlier phase, signaling via $Ca_v2.1$ channels in PCs triggers the translocation of CFs from the PC soma to dendrites and strengthens CF wiring (Hashimoto et al., 2011). Although calcium signaling is strongly disturbed in RIM4 KO mice (Fig. 3.7), the results from the slice experiments provided no evidence for multiple innervations of CFs (Fig. 3.9.F) and for remaining CF terminals on PC somas (Fig. 3.19.D). In the late developmental stage, signaling via mGluR1 is critical to maintain CF and PF territories on PC dendrites (Ichikawa et al., 2015), yet the mGluR1-related signaling is also disrupted in RIM4 KO mice (Fig. 3.20). Therefore, impaired mGluR1-triggered signaling during the development

in the absence of RIM4 in PCs could cause the aberrant distribution of CF-PC synapses in RIM4 KO mice.

In summary, RIM4 is important for maintaining cerebellar morphology and signaling deficits in RIM4-ablated PCs, especially the calcium- and mGluR1-related signaling, might contribute to impaired CF-PC synapses during development, and ultimately cause a dysmorphic change in PCs.

4.2 Aberrant PC activity without RIM4 induces episodic motor impairments or motor deficits

Spontaneous activity is one of the key features of cerebellar PCs. In the absence of synaptic inputs PCs fire spontaneously with a high frequency both *in vitro* (20-50 Hz; Yamamoto, 1973) and *in vivo* (40-150 Hz; Bell and Grimm, 1969; Hounsgaard, 1979). Multiple lines of evidence in this study support the hypothesis that RIM4 has a role in the regulation of intrinsic membrane properties of PCs: (1) a reduced firing rate in the absence of synaptic inputs (Fig. 3.3 and 3.13), (2) a disturbed potassium conductance (Fig. 3.16-3.18), and (3) a signaling deficit via mGluR1 activation (Fig. 3.20). The high-frequency APs in PCs are generated by the intrinsic conductance primarily via voltage-gated sodium channels (Na_v), producing a resurgent current (Khaliq et al., 2003). Among the pore-forming α subunits (Na_v 1.1-1.9; Goldin et al., 2000), PCs express $Na_v1.1$ in the cell body (accounts for 60% of sodium conductance in PCs; Westenbroek et al., 1989) and $Na_v1.6$ in the soma, axon hillock, and dendrites (contributing to the remaining sodium conductance in PCs; Kalume et al., 2007). Mutant mice of these channels are known to be also associated with ataxic phenotypes (Levin et al., 2006; Kalume et al., 2007). Although the mean firing rate is significantly decreased in RIM4 KO mice (Fig. 3.3B), interestingly, the function of Na_v is not altered without RIM4 showing the same peak amplitude of APs suggesting unchanged Na^+ conductance (Fig. 3.16.B).

The pace-making activity of PCs is known to be important to maintain motor coordination (Walter et al., 2006; Tara et al., 2018). A reduced firing rate of PCs is commonly found in mouse SCA models: SCA1 (Hourez et al., 2011), SCA2 (Hansen et al., 2013), SCA3 (Shakkottai et al., 2011), SCA5 (Perkins et al., 2010), SCA6 (Jaybal et al., 2016), and SCA13 (Hurlock et al., 2008). A dysfunction of PCs without changes in the firing rate has also been frequently found in episodic ataxia (EA) models (reviewed in Hoxha et al., 2018).

For instance, a mutant in the gene encoding the pore-forming and voltage-sensing α1A subunit of Ca$_v$2.1 (*CACNA1A*) exhibits type-2 episodic ataxia (EA2; Ophoff et al., 1996). A mouse line (*tottering*) with a point mutation at the α1A subunit of Ca$_v$2.1 was generated by Green M. C. and Sidman R. L. in 1962 and these mice develop episodes of motor impairment. A change in spike regularity rather than in the firing rate of PC spikes is the key feature that has been described not only in the *tottering* mice (Alviña and Khodakhah, 2010; Tara et al., 2018) but also in other Ca$_v$-mutant mice, the *leaner* and *ducky* mice (Walter et al., 2006). In PCs, the spike regularity is primarily controlled by calcium-dependent potassium channels (K$_{Ca}$), especially by the small-conductance calcium-activated potassium (SK) channels (Walter et al., 2006). Among the three subunits, PCs express only SK2 channels (Cingolani et al., 2002) which are important for controlling the pace-making activity in mice (Kasumu et al., 2012). Importantly, the function of SK2 channels in PCs is coupled to calcium entry via Ca$_v$2.1 in PCs (Womack et al., 2004) as SK2 channels are colocalized with Ca$_v$2.1 (Indriati et al., 2013). In EA2 mouse models, it has been reported that the dysfunction of SK2 channels is highly associated with the irregular firing spikes of PCs (Walter et al., 2006). Therefore, the activation of SK2 channels using a pharmacological approach, such as chlorzoxazone and 1-ethyl-2-benzimidazolinone, has been a therapeutic target in EA2 mouse models (Alviña and Khodakhah, 2010; Walter et al., 2006). Neither the function or localization of SK2 channels in PCs has been tested yet in RIM4 lacking mice. But the data that the spike regularity is not altered in RIM4 KO mice (Fig. 3.3C and 3.6B) suggests that the function of SK2 channels might not be altered in these mice.

In ataxia studies, the administration of caffeine is a tool to investigate physiological changes during ataxic episodes, for example the *tottering* mice develop an episodic motor impairment after caffeine injection (Fureman et al., 2002; Raike et al., 2013). We found that also RIM4 KO mice develop episodes after intraperitoneal caffeine injection. An erratic PC activity in the *tottering* mice is found during both spontaneous and caffeine-induced ataxic episodes (Tara et al., 2018). One might suppose that the erratic PC activity during the episode is mainly due to the abnormal and hyperactive movements, but an analysis of *tottering* mice revealed that they display the irregular activity even during the stationary period (Tara et al., 2018). In my study, the pace-making activity of PCs was tested in slices in the presence of synaptic blockers. The slices were prepared from mice

that had no episodes shortly before the preparation. Therefore, it has been aimed for investigating the intrinsic firing properties of PCs in the RIM4 ablated mice so that we could understand better the function of RIM4 in the modulation of somatic excitability in PCs. The RIM4 deficient mice exhibit a motor dysfunction even outside of ataxic episodes, suggesting that it might be explained by the disturbed intrinsic firing properties of PCs in these mice. An altered intrinsic property could change the output from the cerebellar cortex causing uncoordinated cerebellar commands. PCs display a strongly disturbed spontaneous activity while caffeine is applied in both RIM4 KO_{const} (Fig. 3.6) and KO_{PCP2} mice (Fig. 3.14), and this phenomenon is reversed when RIM4 is introduced (Fig. 3.23). These results prove that RIM4 is required for maintaining spontaneous activity of PCs.

Therefore, RIM4 is crucial to maintain the excitability and intrinsic membrane properties of PCs and a signaling deficit in the pace-making activity of PCs without RIM4 might induce the motor phenotype.

4.3 Absence of RIM4 changes the temporal pattern of the cerebellar output

Precision of neuronal activity is very important especially when signaling from multiple neurons conveys a population response. A microzone is a functional module in the cerebellar cortex, and it overlaps with a somatotopic receptive field along the sagittal sections (Anderson and Oscarsson, 1978). It has been reported that a group of 20-40 PCs converges and delivers highly synchronized inputs to one DCN neuron eliciting a time-locked cerebellar output (Person and Raman, 2012). In the cerebellum, the precision of PC spikes is crucial for motor control, and a disturbed population activity of PCs in the cerebellar cortex has been shown in the *tottering* mice (Hoebeek et al., 2005; Chen et al., 2009). Altered intrinsic firing properties of individual PCs in the absence of RIM4, displaying a reduced spontaneous activity and the loss of rhythmical bursting spikes (Fig. 3.3 and 3.13), might cause the imprecision of the cerebellar output. According to the histogram of log transformed CV_{ISI} (Fig. 3.3.C and 3.13.C) WT PCs cover the full range of firing behavior in terms of their regularity, but RIM4 KO mice show a loss of spikes population, lacking rhythmical bursting spikes. PCs display a distinct firing behavior, called trimodal firing which is composed of three different firing behaviors: tonic, silence, and burst (Womack and Khodakhah, 2002). While a rhythmical bursting was observed in WT mice which is very similar to that described by Womack and Khodakhah's, it was

surprisingly absent in the entire data sets of RIM4 KO mice (Fig. 3.3.C and 3.13.C). As discussed in the previous section (see 4.2), the spike regularity is critical to maintain a normal motor coordination. The rhythmical bursting spikes are regulated by the BK channels (Cheron et al., 2009). BK channels are highly expressed in the cerebellum and mice lacking BK channels develop an ataxic phenotype (Chen et al., 2010). An injection of the BK channel blocker, paxilline, into WT mice triggers rhythmical firing which shows comparable results in the autocorrelogram to those that I observed in RIM4 WT PCs (Fig. 3.4.C; Fig. 7D in Cheron et al., 2009). The importance of regulation of rhythmicity via BK channels has been clearly shown in that abnormal PC rhythmicity in their spikes is transmitted to the output level (Cheron et al., 2018). A comprehensive study using a computation model showed that the irregularity of PC spikes can cause drastic alterations in the population response and that the synchronized population activity of PCs is critical on the level of cerebellar output (Glasauer et al., 2011). A disrupted synchronized activity of PCs within the microzone (Fig. 3.7G-I) was found in RIM4 KO mice, indicating a misaligned activity of the cerebellar output.

Taken together, the uncoordinated ensemble outputs of cerebellar PCs in RIM4 ablated mice might induce episodes of motor impairment.

4.4 RIM4 is involved in calcium-related signals in the cerebellar circuit

Monitoring calcium dynamics in neurons is a reliable indicator of neuronal activity. While it is well established that the large RIMs determine the density of VGCCs at presynapses (Han et al., 2011; Kaeser et al., 2011), the question if RIM4 is involved in this process has not been resolved yet. Spontaneous calcium transient in PCs have been assessed both *in vitro* and *in vivo*, and revealed the importance of calcium signals to cause cerebellar outputs (Konnerth et al., 1992; Roome and Kuhn, 2018). As discussed earlier, calcium signaling is critical for many channels and deficits in calcium-dependent channels in PCs induce motor impairments. It was clearly shown in electron microscopic images that $Ca_v2.1$ channels are clustered on PC dendrites and colocalize with SK2 and BK channels (Indriati et al., 2013). $Ca_v2.1$ channels are the most abundant type of VGCCs in PC dendrites, accounting for over 90% of Ca^{2+} currents (Ross and Werman, 1987; Tank et al., 1988; Regan, 1991). In clinical research, a point mutation in the *CACNA1A* gene, encoding the α subunit of the $Ca_v2.1$, has been identified in EA patients (Ophoff et al.,

1996; Jodice et al., 1997). Hence, numerous studies have been investigated $Ca_v2.1$ mutant mice: *tottering* (Fletcher et al., 1996), *leaner* (Tsuji and Meier, 1971), and *ducky* mice (Barclay et al., 2001). The calcium current density via $Ca_v2.1$ is drastically reduced in the *tottering* mice by 40%, in the *leaner* mice by 60% (Wakamori et al., 1998), and in the *ducky* mice by 40% (Donato et al., 2006). Another mouse line, the *rolling Nagoya* mice, carrying a mutation in the voltage sensing segment S4 of the $Ca_v2.1$ protein, show a reduced calcium current (by 40%) due to lower voltage sensitivity resulting in an ataxic phenotype (Mori et al., 2000).

According to a previous study focused on the physiology of glutamatergic inputs on PCs in the *tottering* and the *rolling Nagoya* mice, synaptic transmission in PF- and CF-PC synapses is altered (Matsushita et al., 2002). In these mutant mice, the EPSCs in PCs evoked by PF activation is reduced without changes in the kinetics and in the magnitude of paired-pulse facilitation (Matsushita et al., 2002). Dysfunction of the PF-PC synapses has been also reported in mice exhibiting ataxic phenotype such as a glutamate receptor $\delta2$ KO mice (Kurihara et al., 1997), the *waggler*, and the *stargazer* mice (mutation in the γ subunit of VGCCs; Chen et al., 1999; Hashimoto et al., 1999). Unlike these studies, the synaptic transmission evoked by PF stimulation is unchanged in RIM4 KO mice (Kim et al., unpublished).

In the RIM4-deficient mice, aberrant calcium signals are found in PCs with a strongly reduced amplitude of spontaneous calcium events (Fig. 3.7.C). The distribution of the amplitude of calcium transient in RIM4 KO mice was shifted towards the lower amplitude (Fig. 3.7.D) suggesting two explanations for this phenomenon depending on the location of impairment: a reduced presynaptic input from CFs or a postsynaptic signaling deficit of the VGCC $Ca_v2.1$ in PCs. It has been noted that the spontaneous activity of olivary neurons primarily contributes to the spontaneous calcium events in PCs (Roh et al., 2020). The average event rate is slightly lower in the RIM4 KO lines (0.2 Hz, Fig. 3.7.E) than the reported firing rate of olivary neurons (0.5-1 Hz; Roh et al., 2020), however, this is due to the fact that the RIM4 KO mice were anesthetized (Arancillo et al., 2015). No signs of multiple innervations of CFs to PCs were found in RIM4 KO mice displaying a stereotypical "all-or-none" event, showing the same response independent of the level of CF input once it reached the threshold to evoke calcium transients in PCs (Fig. 3.9.F). As the distribution of CF-PC synapses is changed (Fig. 3.19.D-F), CF-induced EPSCs (Fig. 3.8.C) and

calcium currents (Fig. 3.10) in PCs are enhanced in RIM4 KO mice. The observation that CF input is not reduced argues against the first hypothesis. Instead, the enhanced signals might be due to the shorter dendrites in RIM4 lacking PCs causing less attenuated signals to arrive at the soma where the recording electrodes are positioned. This phenomenon has been demonstrated in previous studies supporting my conclusion. In both the *rolling Nagoya* mice and mice lacking the auxiliary subunit of VGCCs $\alpha 2\delta 2$ the magnitude of EPSCs driven by CF inputs is enhanced (Matsushita et al., 2002; Beeson et al., 2020). More interestingly, this phenotype has been explained by the more abundant proximal innervation of CFs in the $\alpha 2\delta 2$ KO mice (Beeson et al., 2020). An altered CF-PC synapse has been noted in mouse models of SCA (reviewed in Smeets and Verbeek, 2016): SCA1 (Orr et al., 1993), SCA7 (David et al., 1997), SCA14 (Chen et al., 2003), and SCA23 (Bakalkin et al., 2010). In SCA1 mice, the spatial distribution of CF-PC synapses is similar to the one observed in RIM4 KO mice (Fig. 3.19.E-F): shorter CF terminals along the ML compared to the control group (Duvick et al., 2010). Also, CF-evoked responses in PCs of SCA1 mice are reduced (Barnes et al., 2011). However, SCA1 mice exhibit multiple innervations of CFs onto a single PC in addition to the remaining somatic innervation (Ebner et al., 2013) which is not found in RIM4 KO mice (Fig. 3.9.F).

Surprisingly, a single activation of CFs induces calcium transients of the same magnitude in PCs of RIM4 KO and WT mice (Fig. 3.9.B-C). However, a burst mimicking the input of olivary neurons triggers a failure of integration of the calcium transient in RIM4 KO mice (Fig. 3.9.D-E). Three distinct populations of inter calcium-event intervals are observed in control mice: calcium bursts (0.3 s), regular calcium spikes (2 s), and inter-burst intervals (4.5 s), which are lost in RIM4 KO mice (Fig. 3.7.F). Since olivary neurons exhibit a bursting activity composed of 1-3 spikes in anesthetized mice (Mathy et al., 2009), the loss of the ability to integrate burst inputs in RIM4 KO mice might be the main reason for the reduced amplitude of spontaneous calcium transients.

Here we can address a question, how the ablation of RIM4 in PCs affects the presynaptic input of CFs exhibiting a loss of burst inputs. The analysis of the calcium bursts detected at the postsynapses is an indirect measurement for accessing inputs at the presynaptic neurons. In case PCs display a dysfunction of VGCCs, the recorded calcium transient in PCs could appear to be a single event independent of the burst inputs of CFs. However, the calcium currents via VGCCs in PCs are increased in RIM4 KO mice (Fig. 3.10) which

is most likely due to a reduced dendritic arbor In PCs similar to the phenotype of the enhanced EPSCs. An investigation of the localization of $Ca_v2.1$ in RIM4 KO mice, such as imaging it via immunogold electron microscopy or dSTORM superresolution microscopy, could help to answer this question. Considering that signaling in the cerebellar circuit in RIM4 KO mice was disturbed throughout development, the observed cerebellar pathology could be the consequence of resulting long-term changes.

In summary, RIM4 is crucial for maintaining normal calcium signaling in PCs. A reduced magnitude of CF-driven calcium transients in PCs without RIM4 is caused by the impaired ability to integrate multiple CF-inputs *in vivo*. Abnormal distribution of CF terminals and a reduced dendritic arborization of PCs in RIM4 lacking mice results in enhanced CF-evoked EPSCs as well as calcium currents via VGCCs.

4.5 A novel function of RIM4 in the cerebellar circuit

In the central nervous system, RIMs have a key role in the modulation of synaptic transmission at the AZ (Schoch et al., 2002; Fourcaudot et al., 2008; Han et al., 2011; Kaeser et al., 2011). In this study, I've demonstrated signaling deficits in cerebellar PCs in RIM4 lacking mice. RIM4 is a key modulator of intrinsic membrane properties as well as calcium transients in PCs. One of my former colleagues performed affinity purification followed by mass spectrometry to identify novel binding partners of RIM4 and revealed that several candidate proteins are involved in intracellular trafficking of vesicles and in cytoskeleton remodeling (K. Michel, Dissertation, 2015). For example, RIM4 interacts with proteins related to the Exocyst complex, such as sec3, sec6, and sec8 (K. Michel, Dissertation, 2015). It has been shown that the Exocyst complex is a regulator for targeting vesicles to the plasma membrane via microtubules (Vega and Hsu, 2001). Also, RIM4 interacts with plakophilin4 which is an intracellular protein involved in the recycling of vesicles via Rab11 binding (K. Michel, Dissertation, 2015; Keil and Hatzfeld, 2014).

An important finding of this study is the observation that RIM4 in contrast to the full-length RIM isoforms, RIM1/2, does not play a role in the regulation of synaptic transmission. RIM4 is composed only of the RIM C2B domain and an isoform-specific N-terminal sequence (Wang and Südhof, 2002). Rab3 plays a role in neurotransmitter release (Geppert et al., 1994). Therefore, it is not surprising that RIM4 is not involved in the regulation of synaptic transmission since it is lacking the zinc-finger domain which is the

binding site for the Rab3. It is known that the C2 domains of RIM are the binding site for SNAP-25, synaptotagmin1, and Liprin-α (Coppola et al., 2001; Schoch et al., 2002; Kaeser et al., 2012). A previous report focused on the importance of the C2B domain of RIM1 for its function needs to be discussed in detail (De Jong et al., 2018). In this comprehensive study, cultured hippocampal neurons of the RIM1/2 double KO mice lacking the C2B domain show a reduction in the magnitude of IPSCs and an altered probability of vesicular release. In RIM1 C2B domain lacking neurons, RIM1/2 are normally located at the AZ, showing a colocalization with Bassoon revealed by a super-resolution microcopy. Besides, these neurons exhibit a comparable level of the readily releasable pool at the AZ by recruiting Munc13 and normal presynaptic calcium influx compared to the control group. The C2B domains of RIM1 also interacts with PIP_2 which is important for synaptic vesicle fusion at the AZ. Although the C2B domain of RIM4 is highly homologous to that of RIM1, strikingly, RIM4 is not directly involved in the regulation of synaptic transmission as the probability of neurotransmitter release is unchanged at the three major synapses of the cerebellar circuit: CF-PC synapses (Fig. 3.8.E), PF-PC synapses (E. Poguzhelskaya, unpublished), and PC-DCN synapses (Fig. 3.15). These findings support that RIM4 displays a novel function in the cerebellar circuit.

In slice experiments RIM4 KO mice showed functional changes in multiple channels and receptors: VGCCs (Fig. 3.10), K^+ channels (Fig. 3.16, 3.17, and 3.18), and mGluR1 (Fig. 3.20). PCs express three members of high threshold potassium channels (K_v3 subfamily,) and $K_v3.3$ is the most highly expressed isoform in PCs (Weiser et al., 1994; Boda et al., 2012). A point mutation in the *KCNC3* gene, encoding $K_v3.3$, was found in SCA13 patients (Waters et al., 2006) and mice lacking $K_v3.3$ develop an ataxia showing a poor performance in a balanced beam (Joho et al., 2006). $K_v3.3$ ablated PCs display a reduced rate of spontaneous spikes which can be rescued by its re-introduction (Akemann and Knöpfel, 2006), a broader AP waveform with a larger amplitude and a reduced fAHP (McMahon et al., 2004), and an altered waveform of CF-evoked CSs show a lower number of spikelets (Zagha et al., 2008). These phenotypes are also clearly found in RIM4 deficient mice (Fig. 3.3.B, 3.16 and 3.18.A), indicating that the function of $K_v3.3$ might be disturbed. According to previous reports, another similar phenotype related to the sub-threshold potassium channels is also found in RIM4 KO mice. In PCs, the sub-threshold potassium channels are known to be important for modulating membrane excitability and

three subtypes are expressed (K_v1, K_v4, and K_v11; Guasti et al., 2005; Khavandgar et al., 2005; Wang and Schreuers, 2006). Among the three subtypes, the K_v4 is a key source of inactivating K^+ currents and is the only channel expressed in PCs (Serôdio and Rudy, 1998). In PCs, $K_v4.3$ is distributed along the soma and dendrites (Wang and Schreurs, 2006), where it is associated with Ca_v3 (Anderson et al., 2013). Mutations in the *KCND3* gene, encoding $K_v4.3$, were detected in SCA19 and SCA22 patients (Duarri et al., 2012; Lee et al., 2012). Similar to the effects of Mefloquine, a $K_v4.3$ blocker, on AP duration (Perez-Cortes et al., 2015), WT PCs increased the width of the AP with a bath application of 50 µM Mefloquine while no effect was detected in RIM4 KO mice (Fig. 3.17). This result suggests a functional deficit of $K_v4.3$ in the absence of RIM4.

  mGluR1 is very important in PCs mediating synaptic plasticity, proper motor coordination (Ichise et al., 2000), and large calcium transients in PC dendrites (Becker et al., 2009). mGluR1 is located outside of the postsynaptic density where it is primarily activated by the spillover of glutamate driven by multiple PF inputs (Batchelor et al., 1994). The $G_{\alpha11}$ and G_q proteins are coupled to mGluR1 involved in the signaling cascades, activating phospholipase C and generating slow EPSCs mostly through the short transient receptor potential channel 3 (Hartmann and Konnerth, 2008). During postnatal development, mGluR1-PKCγ signaling regulates synaptic pruning by eliminating PF synapses from the proximal dendrites of PCs and CF synapses from the PC soma (Watanabe and Kano, 2011; Ichikawa et al., 2015). Hence, it might be that mGluR1-related signaling deficits in RIM4 KO mice alter CF terminals during the postnatal development resulting in the abundant proximal distribution of CF-PC synapses (Fig. 3.19).

  When RIM4 is introduced in RIM4-ablated PCs even in the fully matured cerebellum, altered electrophysiological properties are restored to the level of the WT control group: an increased spontaneous firing rate as an indicator of the rescue in intrinsic membrane properties, no changes in caffeine-induced firing rate reduction, detection of a rhythmical burst firing, and restored mGluR1-related signaling (Fig. 3.23). Following question can be addressed if the dysfunction in multiple channels and in receptors in RIM4 lacking mice might be due to the mislocation at the active sites on PC dendrites rather than the possibility that RIM4 directly binds to those channels and receptors. Neurons adjust their synaptic strength to the activity they experience, for example by regulating their molecular composition (Douglas et al., 1988). After kainic acid injection into the hippocampus, the

level of RIM4 is enhanced by an increased activity in the hippocampus (Hermey et al., 2013). Likewise, the level of RIM4 in PCs might be dependent on neuronal activity as the expression of RIM4 in RIM4 KO mice restored the PC activity to the level of control group. We also found evidence showing the occurrence of episodic motor impairment in RIM4 KO mice follows a circadian rhythm. Future work on an acute deletion of RIM4 in adult mice, e.g. testing whether these mice develop episodes of motor impairment, and on the analysis of RIM4 expression at different time points of the day could help to answer the question.

In conclusion, this study demonstrates the importance of RIM4 in the maintenance of the somato-dendritic excitability of PCs by regulating the function of multiple channels and receptors, possibly via an involvement in the vesicular transport of membrane proteins. Thereby the results of this study show for the first time that RIM4 is essential for the physiological function of PCs but that its function is different from that of the large RIMs.

5. Abstract

Our brain comprises large number of neurons, which are elaborately interconnected by a complex network of neuronal contacts via synapse where neuronal information is transmitted from one neuron to another by releasing neurotransmitters. Within the cytomatrix at the active zone, a specialized area on the plasma membrane at synapse, RIMs are the key proteins that are important for regulating synaptic function by recruiting other synaptic proteins as well as voltage-dependent calcium channels. In mammalian, the RIMs are expressed in seven different isoforms encoded by four RIM genes: the large RIM isoforms (RIM1α/β and RIM2α/β) and the small RIM isoforms (RIM2/3/4γ). In contrast to the large RIM isoforms which are known to be important for mediating synaptic transmission, the function of the small RIM isoforms has not been fully understood yet. Previous studies of RIM4 revealed a strong expression of RIM4 in the cerebellar Purkinje cells, a distinct distribution in culture neurons that are not exclusively localized at presynapse and its novel function in establishing dendritic arbors in culture neurons.

Previously, constitutive RIM4 KO mice and conditional RIM4 KO mice in Purkinje cells were generated in Schoch's lab. These RIM4-deficient mice developed an episodic motor phenotype with impaired their hindlimbs. In this study, I investigated the role of RIM4 in the cerebellar circuit by characterizing the effects of RIM4 ablation in cytoarchitecture in the cerebellum, electrophysiological properties of Purkinje cells, and calcium dynamics.

First, we identified a megascopic alteration in the cerebellar morphology in RIM4-lacking mice, showing a significantly reduced size of the cerebellum. Moreover, the ablation of RIM4 drastically reduced a dendritic arborization of the Purkinje cells. These results suggested that a dysfunction in Purkinje cells of RIM4 knock-out mice might be the key explaining motor episodes. To investigate this, I recorded spontaneous activity of Purkinje cells in the absence of synaptic inputs in order to understand intrinsic excitability and in the presence of caffeine as a widely used method to induce ataxic phenotype. As a result, Purkinje cells without RIM4 displayed disturbed spontaneous spikes lacking a population of the burst firing cells and showed a stronger effect of caffeine on firing rates compared to wild-type mice.

Next, we performed calcium imaging in slice and *in vivo* to investigate the functional role of RIM4 in modulation of calcium signaling in the cerebellar network. Overall, calcium influx in Purkinje cell dendrites mediated by climbing fiber inputs was strongly reduced in

mice and a temporal pattern of calcium spikes were also disturbed in RIM4 KO mice. In addition, *In vivo* calcium imaging data showed a reduced synchronicity of the spontaneous calcium events in neighboring Purkinje cells in RIM4 knock-out mice, suggesting an uncoordinated output from the cerebellar cortex. Further investigations in properties of calcium-related signaling in Purkinje cells in slice revealed that both climbing fiber-evoked excitatory postsynaptic potentials and voltage-gated calcium currents are elevated in RIM4 KO mice without a change in single climbing fiber-evoked postsynaptic transient in Purkinje cell. Immunolabeling of climbing fiber using a VGlut2 marker revealed a change in climbing fiber innervation showing a higher proximal distribution of presynaptic terminal in RIM4 KO mice. Taken together, RIM4 is important to maintain postsynaptic calcium transient in Purkinje cells.

In line with the finding that Purkinje cell-specific RIM4 knock-out mice phenocopied the impaired motor coordination, the size of the cerebellum as well as spontaneous spikes of Purkinje cells were reduced in conditional RIM4 KO mice. The effect of caffeine on pace-making activity of Purkinje cells was comparable to the results of constitutive RIM4 KO mice. Electrophysiological recordings were performed in the Purkinje cell-specific RIM4 KO line to elucidate a novel function of RIM4 in the cerebellum. Unlike the large RIM isoforms, we found that the ablation of RIM4 had no impact on presynaptic short-term plasticity both in Purkinje cell-deep cerebellar nuclei synapse and in climbing fiber-Purkinje cell synapse. In other words, RIM4 was not involved in regulating the probability of neurotransmitter release in these synapses.

As a former colleague, K. Michel (Dissertation, 2015), showed in the proteomics data, RIM4 might be involved in vesicles tracking instead of mediating synaptic function at the active zone. Therefore, I characterized functions of several ion channels of which the level was reduced in RIM4 KO mice. Voltage-gated potassium channels were the first candidate as Purkinje cells of RIM4 KO mice displayed a broader action potential without changes in sodium spike. A subfamily of subthreshold potassium channels highly expressed in Purkinje cells, KCND3 ($K_v4.3$) channels, was tested and the pharmacological blocking of these channels resulted in broadening action potential waveforms only in wild-type mice. Climbing fiber-evoked complex spikes of Purkinje cells showed altered the waveform with a smaller coast-line index and the lower number of spikelets in RIM4 KO mice, suggesting that KCNC3 ($K_v3.3$) channels, a subfamily of high-threshold potassium channels, might

be also associated according to many other previous studies. In addition, the signaling deficits of group I metabotrophic glutamate receptors were observed in RIM4 KO mice.

Finally, we tested whether described phenotypes were rescued by delivery of AAV-RIM4 constructs into RIM4-ablated Purkinje cells and whether the time of the delivery was crucial for the rescue of phenotypes. To answer this, we injected AAV carrying RIM4 genes in the cerebellum at either postnatal day 0 or adult. In both conditions, surprisingly, the re-introduction of RIM4 in Purkinje cells fully rescued at functional level, showing no alterations in spontaneous activities and in signaling of group I metabotrophic glutamate receptors. However, the rescue in dendritic arborization was found only in the mice which were injected in earlier time.

Taken together, the results in this study characterized the signaling deficits of cerebellar in RIM4-deficient mice suggest a novel function of RIM4 in regulating somato-dendritic excitability in Purkinje cells by mediating vesicles trafficking in contrast to the functions of the large RIM isoforms. Also, the specific alterations in Purkinje cell signaling provide new insights that could elucidate the physiological mechanism of ataxia phenotypes in mice.

6. List of figures

7. List of tables

8. References

A. Kimberley McAllister. Cellular and Molecular Mechanisms of Dendrite Growth. Cerebral Cortex. 2000; 10: 963–973

A.L Hodgkin. A.F Huxley. Action potentials recorded from inside a nerve fibre. Nature 1939; 114: 710-711

Aiba A. Kano M. Chen C. Stanton ME. Fox GD. Herrup K. Zwingman TA. Tonegawa S. Deficient cerebellar long-term depression and impaired motor learning in mGluR1 mutant mice. Cell 1994; 79(2):377-88

Akemann W. Knöpfel T. Interaction of Kv3 potassium channels and resurgent sodium current influences the rate of spontaneous firing of Purkinje neurons. J Neurosci 2006; 26(17): 4602-12

Alvarez-Baron E. Michel K. Mittelstaedt T. Opitz T. Schmitz F. Beck H. Dietrich D. Becker AJ. Schoch S. RIM3γ and RIM4γ are key regulators of neuronal arborization. J Neurosci 2013; 33(2): 824-39

Alviña K. Khodakhah K. The therapeutic mode of action of 4-aminopyridine in cerebellar ataxia. J Neurosci 2010; 30(21): 7258-68

Anderson D. Engbers JD. Heath NC. Bartoletti TM. Mehaffey WH. Zamponi GW. Turner RW. The Cav3-Kv4 complex acts as a calcium sensor to maintain inhibitory charge during extracellular calcium fluctuations. J Neurosci 2013; 33: 7811-24

Andersson G. Oscarsson O. Climbing fiber microzones in cerebellar vermis and their projection to different groups of cells in the lateral vestibular nucleus. Exp Brain Res 1978; 32(4): 565-79

Apps R. Garwicz M. Anatomical and physiological foundations of cerebellar information processing. Nat Rev Neurosci 2005; 6(4): 297-311

Arancillo M. White JJ. Lin T. Stay TL. Sillitoe RV. In vivo analysis of Purkinje cell firing properties during postnatal mouse development. J Neurophysiol 2015; 113(2): 578-91

Arata A. Ito M. Purkinje cell functions in the in vitro cerebellum isolated from neonatal rats in a block with the pons and medulla. Neurosci Res 2004; 50(3): 361-7

Azevedo FA. Carvalho LR. Grinberg LT. Farfel JM. Ferretti RE. Leite RE. Jacob Filho W. Lent R. Herculano-Houzel S. Equal numbers of neuronal and nonneuronal cells make the human brain an isometrically scaled-up primate brain. J Comp Neurol 2009; 513(5): 532-41

Bakalkin G. Watanabe H. Jezierska J. Depoorter C. Verschuuren-Bemelmans C. Bazov I. Artemenko KA. Yakovleva T. Dooijes D. Van de Warrenburg BP. Zubarev RA. Kremer B. Knapp PE. Hauser KF. Wijmenga C. Nyberg F. Sinke RJ. Verbeek DS. Prodynorphin mutations cause the neurodegenerative disorder spinocerebellar ataxia type 23. Am J Hum Genet 2010; 87(5): 593-603

Barclay J. Balaguero N. Mione M. Ackerman SL. Letts VA. Brodbeck J. Canti C. Meir A. Page KM. Kusumi K. Perez-Reyes E. Lander ES. Frankel WN. Gardiner RM. Dolphin AC. Rees M. Ducky mouse phenotype of epilepsy and ataxia is associated with mutations in the Cacna2d2 gene and decreased calcium channel current in cerebellar Purkinje cells. J Neurosci 2001; 21(16): 6095-104

Barnes JA. Ebner BA. Duvick LA. Gao W. Chen G. Orr HT. Ebner TJ. Abnormalities in the climbing fiber-Purkinje cell circuitry contribute to neuronal dysfunction in ATXN1[82Q] mice. J Neurosci 2011; 31(36): 12778-89

Barski JJ. Dethleffsen K. Meyer M. Cre recombinase expression in cerebellar Purkinje cells. Genesis 2000; 28(3-4): 93-8

Batchelor AM. Garthwaite J. Frequency detection and temporally dispersed synaptic signal association through a metabotropic glutamate receptor pathway. Nature 1997; 385(6611): 74-7

Batchelor AM. Madge DJ. Garthwaite J. Synaptic activation of metabotropic glutamate receptors in the parallel fibre-Purkinje cell pathway in rat cerebellar slices. Neuroscience 1994; 63(4): 911-5

Becker EB. Oliver PL. Glitsch MD. Banks GT. Achilli F. Hardy A. Nolan PM. Fisher EM. Davies KE. A point mutation in TRPC3 causes abnormal PC development and cerebellar ataxia in moonwalker mice. Proc Natl Acad Sci U S A 2009; 106: 6706-11

Beeson KA. Beeson R. Westbrook GL. Schnell E. α2δ-2 Protein Controls Structure and Function at the Climbing Fiber Synapse. J Neurosci 2020; 40: 2403-2415

Bell CC. Grimm RJ. Discharge properties of Purkinje cells recorded on single and double microelectrodes. J Neurophysiol 1969; 32(6): 1044-55

Belmeguenai A. Hosy E. Bengtsson F. Pedroarena CM. Piochon C. Teuling E. He Q. Ohtsuki G. De Jeu MT. Elgersma Y. De Zeeuw CI. Jörntell H. Hansel C. Intrinsic plasticity complements long-term potentiation in parallel fiber input gain control in cerebellar Purkinje cells. J Neurosci 2010; 30(41): 13630-43

Benton MD. Lewis AH. Bant JS. Raman IM. Iberiotoxin-sensitive and -insensitive BK currents in Purkinje neuron somata. J Neurophysiol 2013; 109(10): 2528-41

Betz A. Thakur P. Junge HJ. Ashery U. Rhee JS. Scheuss V. Rosenmund C. Rettig J. Brose N. Functional interaction of the active zone proteins Munc13-1 and RIM1 in synaptic vesicle priming. Neuron 2001; 30(1): 183-96

Blundell J. Kaeser PS. Südhof TC. Powell CM. RIM1alpha and interacting proteins involved in presynaptic plasticity mediate prepulse inhibition and additional behaviors linked to schizophrenia. J Neurosci 2010; 30(15): 5326-33

Boda E. Hoxha E. Pini A. Montarolo F. Tempia F. Brain expression of Kv3 subunits during development. adulthood and aging and in a murine model of Alzheimer's disease. J Mol Neurosci 2012; 46(3): 606-15

Browne DL. Gancher ST. Nutt JG. Brunt ER. Smith EA. Kramer P. Litt M. Episodic ataxia/myokymia syndrome is associated with point mutations in the human potassium channel gene. KCNA1. Nat Genet 1994; 8(2): 136-40

Cerminara NL. Lang EJ. Sillitoe RV. Apps R. Redefining the cerebellar cortex as an assembly of non-uniform PC microcircuits. Nat Rev Neurosci 2015; 16(2): 79-93

Chen G. Popa LS. Wang X. Gao W. Barnes J. Hendrix CM. Hess EJ. Ebner TJ. Low-frequency oscillations in the cerebellar cortex of the tottering mouse. J Neurophysiol 2009; 101(1): 234-45

Chen Y. Song X. Ye S. Miao L. Zhu Y. Zhang RG. Ji G. Structural insight into enhanced calcium indicator GCaMP3 and GCaMPJ to promote further improvement. Protein Cell 2013; 4(4): 299-309

Cheron G. Márquez-Ruiz J. Cheron J. Prigogine C. Ammann C. Lukowski R. Ruth P. Dan B. Purkinje cell BKchannel ablation induces abnormal rhythm in deep cerebellar nuclei and prevents LTD. Sci Rep 2018; 8(1): 4220

Cheron G. Sausbier M. Sausbier U. Neuhuber W. Ruth P. Dan B. Servais L. BK channels control cerebellar Purkinje and Golgi cell rhythmicity in vivo. PLoS One 2009; 4(11): e7991

Cingolani LA. Gymnopoulos M. Boccaccio A. Stocker M. Pedarzani P. Developmental regulation of small-conductance Ca2+-activated K+ channel expression and function in rat Purkinje neurons. J Neurosci 2002; 22(11): 4456-67

Conquet F. Bashir ZI. Davies CH. Daniel H. Ferraguti F. Bordi F. Franz-Bacon K. Reggiani A. Matarese V. Condé F. et al. Motor deficit and impairment of synaptic plasticity in mice lacking mGluR1. Nature 1994; 372(6503): 237-43

Coppola T. Magnin-Luthi S. Perret-Menoud V. Gattesco S. Schiavo G. Regazzi R. Direct interaction of the Rab3 effector RIM with Ca2+ channels. SNAP-25. and synaptotagmin. J Biol Chem 2001; 276(35): 32756-62

David G. Abbas N. Stevanin G. Dürr A. Yvert G. Cancel G. Weber C. Imbert G. Saudou F. Antoniou E. Drabkin H. Gemmill R. Giunti P. Benomar A. Wood N. Ruberg M. Agid Y. Mandel JL. Brice A. Cloning of the SCA7 gene reveals a highly unstable CAG repeat expansion. Nat Genet 1997; 17(1): 65-70

de Jong APH. Roggero CM. Ho MR. Wong MY. Brautigam CA. Rizo J. Kaeser PS. RIM C2B Domains Target Presynaptic Active Zone Functions to PIP2-Containing Membranes. Neuron 2018; 98(2): 335-349.e7

De Zeeuw CI. Berrebi AS. Postsynaptic targets of Purkinje cell terminals in the cerebellar and vestibular nuclei of the rat. Eur J Neurosci 1995; 7(11): 2322-33

DEL CASTILLO J. KATZ B. Statistical factors involved in neuromuscular facilitation and depression. J Physiol 1954; 124(3): 574-85

Ding M. Weng C. Fan S. Cao Q. Lu Z. Purkinje Cell Degeneration and Motor Coordination Deficits in a New Mouse Model of Autosomal Recessive Spastic Ataxia of Charlevoix-Saguenay. Front Mol Neurosci 2017; 10: 121

Donato R. Page KM. Koch D. Nieto-Rostro M. Foucault I. Davies A. Wilkinson T. Rees M. Edwards FA. Dolphin AC. The ducky(2J) mutation in Cacna2d2 results in reduced spontaneous Purkinje cell activity and altered gene expression. J Neurosci 2006; 26(48): 12576-86

Duarri. A.. Jezierska. J.. Fokkens. M.. Meijer. M.. Schelhaas. H. J.. den Dunnen. W. F.. et al. Mutations in potassium channel KCND3 cause spinocerebellar ataxia type 19. Ann. Neurol 2012; 72: 870–880

DUDEL J. KUFFLER SW. Presynaptic inhibition at the crayfish neuromuscular junction. J Physiol 1961; 155(3): 543-62

Duvick L. Barnes J. Ebner B. Agrawal S. Andresen M. Lim J. Giesler GJ. Zoghbi HY. Orr HT. SCA1-like disease in mice expressing wild-type ataxin-1 with a serine to aspartic acid replacement at residue 776. Neuron 2010; 67(6): 929-35

Ebner BA. Ingram MA. Barnes JA. Duvick LA. Frisch JL. Clark HB. Zoghbi HY. Ebner TJ. Orr HT. Purkinje cell ataxin-1 modulates climbing fiber synaptic input in developing and adult mouse cerebellum. J Neurosci 2013; 33(13): 5806-20

Eccles JC. Llinás R. Sasaki K. The excitatory synaptic action of climbing fibres on the Purkinje cells of the cerebellum. J Physiol 1966; 182(2): 268-96

ECCLES JC. McINTYRE AK. The effects of disuse and of activity on mammalian spinal reflexes. J Physiol 1953; 121(3): 492-516

Fletcher CF. Lutz CM. O'Sullivan TN. Shaughnessy JD Jr. Hawkes R. Frankel WN. Copeland NG. Jenkins NA. Absence epilepsy in tottering mutant mice is associated with calcium channel defects. Cell 1996; 87(4): 607-17

Fourcaudot E. Gambino F. Humeau Y. Casassus G. Shaban H. Poulain B. Lüthi A. cAMP/PKA signaling and RIM1alpha mediate presynaptic LTP in the lateral amygdala. Proc Natl Acad Sci U S A 2008; 105(39): 15130-5

Fureman BE. Jinnah HA. Hess EJ. Triggers of paroxysmal dyskinesia in the calcium channel mouse mutant tottering. Pharmacol Biochem Behav 2002; 73(3): 631-7

Gao Y. Perkins EM. Clarkson YL. Tobia S. Lyndon AR. Jackson M. Rothstein JD. β-III spectrin is critical for development of purkinje cell dendritic tree and spine morphogenesis. J Neurosci 2011; 31(46): 16581-90

Geppert M. Bolshakov VY. Siegelbaum SA. Takei K. De Camilli P. Hammer RE. Südhof TC. The role of Rab3A in neurotransmitter release. Nature 1994; 369: 493-7

Giovannucci A. Friedrich J. Gunn P. Kalfon J. Brown BL. Koay SA. Taxidis J. Najafi F. Gauthier JL. Zhou P. Khakh BS. Tank DW. Chklovskii DB. Pnevmatikakis EA. CaImAn an open source tool for scalable calcium imaging data analysis. Elife 2019; 8: e38173

Girard M. Larivière R. Parfitt DA. Deane EC. Gaudet R. Nossova N. Blondeau F. Prenosil G. Vermeulen EG. Duchen MR. Richter A. Shoubridge EA. Gehring K. McKinney RA. Brais B. Chapple JP. McPherson PS. Mitochondrial dysfunction and Purkinje cell loss in autosomal recessive spastic ataxia of Charlevoix-Saguenay (ARSACS). Proc Natl Acad Sci U S A 2012; 109(5): 1661-6

Glasauer S. Kalla R. Büttner U. Strupp M. Brandt T. 4-aminopyridine restores visual ocular motor function in upbeat nystagmus. J Neurol Psychiatry 2005; 76: 451-3

Glasauer S. Rössert C. Strupp M. The role of regularity and synchrony of cerebellar Purkinje cells for pathological nystagmus. Ann N Y Acad Sci 2011; 1233: 162-7

Goldin AL. Barchi RL. Caldwell JH. Hofmann F. Howe JR. Hunter JC. Kallen RG. Mandel G. Meisler MH. Netter YB. Noda M. Tamkun MM. Waxman SG. Wood JN. Catterall WA. Nomenclature of voltage-gated Na channels. Neuron 2000; 28: 365-8

Gracheva EO. Hadwiger G. Nonet ML. Richmond JE. Direct interactions between C. elegans RAB-3 and Rim provide a mechanism to target vesicles to the presynaptic density. Neurosci Lett 2008; 444(2): 137-42

Graf ER. Valakh V. Wright CM. Wu C. Liu Z. Zhang YQ. DiAntonio A. RIM promotes calcium channel accumulation at active zones of the Drosophila neuromuscular junction. J Neurosci 2012; 32(47): 16586-96

GRANIT R. PHILLIPS CG. Excitatory and inhibitory processes acting upon individual Purkinje cells of the cerebellum in cats. J Physiol 1956; 133(3): 520-47

GREEN MC. SIDMAN RL. Tottering--a neuromusclar mutation in the mouse. And its linkage with oligosyndacylism. J Hered 1962; 53: 233-7

Gruol DL. Jacquin T. Yool AJ. Single-channel K+ currents recorded from the somatic and dendritic regions of Purkinje neurons in culture. J Neurosci 1991; 11: 1002-15

Guasti L. Cilia E. Crociani O. Hofmann G. Polvani S. Becchetti A. Wanke E. Tempia F. Arcangeli A. Expression pattern of the ether-a-go-go-related (ERG) family proteins in the adult mouse central nervous system: evidence for coassembly of different subunits. J Comp Neurol 2005; 491(2): 157-74

Han. Y.. Kaeser. P.. Südhof. T.. and Schneggenburger. R. RIM determines Ca2+ channel density and vesicle docking at the presynaptic AZ. Neuron 2011; 69: 304–316

Hansen ST. Meera P. Otis TS. Pulst SM. Changes in Purkinje cell firing and gene expression precede behavioral pathology in a mouse model of SCA2. Hum Mol Genet. 2013; 22(2): 271-83

Hartmann J. Dragicevic E. Adelsberger H. Henning HA. Sumser M. Abramowitz J. Blum R. Dietrich A. Freichel M. Flockerzi V. Birnbaumer L. Konnerth A. TRPC3 channels are required for synaptic transmission and motor coordination. Neuron 2008; 59(3): 392-8

Harvey RJ. Napper RM. Quantitative study of granule and Purkinje cells in the cerebellar cortex of the rat. J Comp Neurol 1988; 274(2): 151-7

Hashimoto K. Tsujita M. Miyazaki T. Kitamura K. Yamazaki M. Shin HS. Watanabe M. Sakimura K. Kano M. Postsynaptic P/Q-type Ca2+ channel in Purkinje cell mediates synaptic competition and elimination in developing cerebellum. Proc Natl Acad Sci U S A 2011; 108(24): 9987-92

Häusser M. Clark BA. Tonic synaptic inhibition modulates neuronal output pattern and spatiotemporal synaptic integration. Neuron 1997; 19(3): 665-78

Herculano-Houzel S. Ribeiro P. Campos L. Valotta da Silva A. Torres LB. Catania KC. Kaas JH. Updated neuronal scaling rules for the brains of Glires (rodents/lagomorphs). Brain Behav Evol 2011; 78(4): 302-14

Herculano-Houzel S. Coordinated scaling of cortical and cerebellar numbers of neurons. Front Neuroanat 2010; 4: 12

Hermey G. Mahlke C. Gutzmann JJ. Schreiber J. Blüthgen N. Kuhl D. Genome-wide profiling of activity-dependent hippocampal transcriptome. PLoS One 2013; 8: e76903

Hoebeek FE. Stahl JS. van Alphen AM. Schonewille M. Luo C. Rutteman M. van den Maagdenberg AM. Molenaar PC. Goossens HH. Frens MA. De Zeeuw CI. Increased noise level of purkinje cell activities minimizes impact of their modulation during sensorimotor control. Neuron 2005; 45(6): 953-65

Hounsgaard J. Pacemaker properties of mammalian Purkinje cells. Acta Physiol Scand 1979; 106(1): 91-2

Hourez R. Servais L. Orduz D. Gall D. Millard I. de Kerchove d'Exaerde A. Cheron G. Orr HT. Pandolfo M. Schiffmann SN. Aminopyridines correct early dysfunction and delay neurodegeneration in a mouse model of spinocerebellar ataxia type 1. J Neurosci 2011; 31(33): 11795-807

Hoxha E. Balbo I. Miniaci MC. Tempia F. Purkinje Cell Signaling Deficits in Animal Models of Ataxia. Front Synaptic Neurosci 2018; 10: 6

Hurlock EC. McMahon A. Joho RH. Purkinje-cell-restricted restoration of Kv3.3 function restores complex spikes and rescues motor coordination in Kcnc3 mutants. J Neurosci 2008; 28(18): 4640-8

Ichikawa R. Sakimura K. Watanabe M. GluD2 Endows Parallel Fiber-Purkinje Cell Synapses with a High Regenerative Capacity. J Neurosci 2016; 36(17): 4846-58

Ichise T. Kano M. Hashimoto K. Yanagihara D. Nakao K. Shigemoto R. Katsuki M. Aiba A. mGluR1 in cerebellar Purkinje cells essential for long-term depression. synapse elimination. and motor coordination. Science 2000; 288(5472): 1832-5

Indriati DW. Kamasawa N. Matsui K. Meredith AL. Watanabe M. Shigemoto R. Quantitative localization of Cav2.1 (P/Q-type) voltage-dependent calcium channels in Purkinje cells: somatodendritic gradient and distinct somatic coclustering with calcium-activated potassium channels. J Neurosci 2013; 33(8): 3668-78

Isaacs KR. Abbott LC. Cerebellar volume decreases in the tottering mouse are specific to the molecular layer. Brain Res Bull 1995; 36(3): 309-14

Ito M. Cerebellar circuitry as a neuronal machine. Prog Neurobiol 2006; 78: 272-303

Ito M. The modifiable neuronal network of the cerebellum. J Physiol 1984; 34: 781-92

Jaeger D. Bower JM. Prolonged responses in rat cerebellar Purkinje cells following activation of the granule cell layer: an intracellular in vitro and in vivo investigation. Exp Brain Res 1994; 100(2): 200-14

Jayabal S. Chang HH. Cullen KE. Watt AJ. 4-aminopyridine reverses ataxia and cerebellar firing deficiency in a mouse model of spinocerebellar ataxia type 6. Sci Rep 2016; 6: 29489

Jayabal S. Ljungberg L. Erwes T. Cormier A. Quilez S. El Jaouhari S. Watt AJ. Rapid Onset of Motor Deficits in a Mouse Model of Spinocerebellar Ataxia Type 6 Precedes Late Cerebellar Degeneration. eNeuro 2015; 2(6): ENEURO.0094-15

Jodice C. Mantuano E. Veneziano L. Trettel F. Sabbadini G. Calandriello L. Francia A. Spadaro M. Pierelli F. Salvi F. Ophoff RA. Frants RR. Frontali M. Episodic ataxia type 2 (EA2) and spinocerebellar ataxia type 6 (SCA6) due to CAG repeat expansion in the CACNA1A gene on chromosome 19p. Hum Mol Genet 1997; 6(11): 1973-8

Joho RH. Street C. Matsushita S. Knöpfel T. Behavioral motor dysfunction in Kv3-type potassium channel-deficient mice. Genes Brain Behav 2006; 5(6): 472-82

Kaeser PS. Deng L. Fan M. Südhof TC. RIM genes differentially contribute to organizing presynaptic release sites. Proc Natl Acad Sci USA 2012; 109, 29: 11830-5

Kaeser PS. Südhof TC. RIM function in short- and long-term synaptic plasticity. Biochem Soc Trans 2005; 33(Pt 6): 1345-9

Kaeser. P. S.. Deng. L.. Wang. Y.. Dulubova. I.. Liu. X.. Rizo. J.. et al. RIM proteins tether Ca2+ channels to presynaptic active zones via a direct PDZ-domain interaction. Cells 2011; 144: 282–295

Kaeser. P. S.. Kwon. H. B.. Chiu. C. Q.. Deng. L.. Castillo. P. E.. and Südhof. T. C. RIM1α and RIM1β are synthesized from distinct promoters of RIM1 gene to mediate differential but overlapping synaptic functions. J Neurosci 2008; 28. 13435–13447

Kalume F. Yu FH. Westenbroek RE. Scheuer T. Catterall WA. Reduced sodium current in Purkinje neurons from Nav1.1 mutant mice: implications for ataxia in severe myoclonic epilepsy in infancy. J Neurosci 2007; 27(41): 11065-74

Kano M. Watanabe T. Uesaka N. Watanabe M. Multiple Phases of Climbing Fiber Synapse Elimination in the Developing Cerebellum. Cerebellum 2018; 17(6): 722-734

Kasumu AW. Hougaard C. Rode F. Jacobsen TA. Sabatier JM. Eriksen BL. Strøbæk D. Liang X. Egorova P. Vorontsova D. Christophersen P. Rønn LC. Bezprozvanny I. Selective positive modulator of calcium-activated K+ channels exerts beneficial effects in a mouse model of spinocerebellar ataxia type 2. Chem Biol 2012; 19(10): 1340-53

Katz B. Miledi R. Spontaneous and evoked activity of motor nerve endings in calcium Ringer. J Physiol 1969; 203(3): 689-706

Keil R. Hatzfeld M. The armadillo protein p0071 is involved in Rab11-dependent recycling. J Cell Sci 2014; 127(Pt 1): 60-71

Khavandgar S. Walter JT. Sageser K. Khodakhah K. Kv1 channels selectively prevent dendritic hyperexcitability in rat Purkinje cells. J Physiol 2005; 569(Pt 2): 545-57

Kintscher M. Wozny C. Johenning FW. Schmitz D. Breustedt J. Role of RIM1α in short- and long-term synaptic plasticity at parallel fibres. Nat Commun 2013; 4: 2392

Knöpfel T. Audinat E. Gähwiler BH. Climbing Fibre Responses in Olivo-cerebellar Cultures. Microelectrode Recordings from PCs. Eur J Neurosci. 1990; 2(8): 726-732

Köhler M. Hirschberg B. Bond CT. Kinzie JM. Marrion NV. Maylie J. Adelman JP. Small-conductance. calcium-activated potassium channels from mammalian brain. Science 1996; 273(5282): 1709-14

Konnerth A. Dreessen J. Augustine GJ. Brief dendritic calcium signals initiate long-lasting synaptic depression in cerebellar Purkinje cells. Proc Natl Acad Sci U S A 1992; 89(15): 7051-5

Koushika SP. Richmond JE. Hadwiger G. Weimer RM. Jorgensen EM. Nonet ML. A post-docking role for active zone protein Rim. Nat Neurosci 2001; 4(10): 997-1005

Kurihara H. Hashimoto K. Kano M. Takayama C. Sakimura K. Mishina M. Inoue Y. Watanabe M. Impaired parallel fiber-->Purkinje cell synapse stabilization during cerebellar development of mutant mice lacking the glutamate receptor delta2 subunit. J Neurosci 1997; 17(24): 9613-23

Kuriyama H. Asakawa S. Minoshima S. Maruyama H. Ishii N. Ito K. Gejyo F. Arakawa M. Shimizu N. Kuwano R. Characterization and chromosomal mapping of a novel human gene. ANKHZN. Gene 2000; 253(2): 151-60

Lallemand Y. Luria V. Haffner-Krausz R. Lonai P. Maternally expressed PGK-Cre transgene as a tool for early and uniform activation of the Cre site-specific recombinase. Transgenic Res 1998; 7(2): 105-12

LARRABEE MG. BRONK DW. Prolonged facilitation of synaptic excitation in sympathetic ganglia. J Neurophysiol 1947; 10(2): 139-54

Latham A. Paul DH. Spontaneous activity of cerebellar Purkinje cells and their responses to impulses in climbing fibres. J Physiol 1971; 213(1): 135-56

Leblond CS. Cliquet F. Carton C. Huguet G. Mathieu A. Kergrohen T. Buratti J. Lemière N. Cuisset L. Bienvenu T. Boland A. Deleuze JF. Stora T. Biskupstoe R. Halling J. Andorsdóttir G. Billstedt E. Gillberg C. Bourgeron T. Both rare and common genetic variants contribute to autism in the Faroe Islands. NPJ Genom Med. 2019; 4

Lee. Y. C.. Durr. A.. Majczenko. K.. Huang. Y. H.. Liu. Y. C.. Lien. C. C.. et al. Mutations in KCND3 cause spinocerebellar ataxia type 22. Ann. Neuro. 2012; 72: 859–869

Liang F. Zhang B. Tang J. Guo J. Li W. Ling EA. Chu H. Wu Y. Chan YG. Cao Q. RIM3gamma is a postsynaptic protein in the rat central nervous system. J Comp Neurol 2007; 503(4): 501-10

Lorenzetto E. Caselli L. Feng G. Yuan W. Nerbonne JM. Sanes JR. Buffelli M. Genetic perturbation of postsynaptic activity regulates synapse elimination in developing cerebellum. Proc Natl Acad Sci U S A. 2009; 106(38): 16475-80

Lu. J.. Li. H.. Wang. Y.. Südhof. T. C.. and Rizo. J. Solution structure of the RIM1alpha PDZ domain in complex with an ELKS1b C-terminal peptide. J. Mol. Biol 2005; 352: 455–466

Mariotti C. Fancellu R. Di Donato S. An overview of the patient with ataxia. J Neurol 2005; 252(5): 511-8

Marshall. L.H.. Magoun. H.W. The Cerebellum. In: Discoveries in the Human Brain. Humana Press. Totowa. NJ 1998: 177-198

Mathy A. Ho SS. Davie JT. Duguid IC. Clark BA. Häusser M. Encoding of oscillations by axonal bursts in inferior olive neurons. Neuron 2009; 62(3): 388-99

Matsushita K. Wakamori M. Rhyu IJ. Arii T. Oda S. Mori Y. Imoto K. Bidirectional alterations in cerebellar synaptic transmission of tottering and rolling Ca2+ channel mutant mice. J Neurosci 2002; 22(11): 4388-98

McMahon A. Fowler SC. Perney TM. Akemann W. Knöpfel T. Joho RH. Allele-dependent changes of olivocerebellar circuit properties in the absence of the voltage-gated potassium channels Kv3.1 and Kv3.3. Eur J Neurosci 2004; 19(12): 3317-27

Mori Y. Wakamori M. Oda S. Fletcher CF. Sekiguchi N. Mori E. Copeland NG. Jenkins NA. Matsushita K. Matsuyama Z. Imoto K. Reduced voltage sensitivity of activation of P/Q-type Ca2+ channels is associated with the ataxic mouse mutation rolling Nagoya (tg(rol)). J Neurosci 2000; 20(15): 5654-62

Mori. Y.. Itsukaichi. Y.. Nishida. M.. Oka. H. Calcium Channel Mutations and Associated Diseases. In: McDonough. S.I. (eds) 2004; 303-330

Nakai J. Ohkura M. Imoto K. A high signal-to-noise Ca(2+) probe composed of a single green fluorescent protein. Nat Biotechnol 2001; 19(2): 137-41

Nedelescu H. Chowdhury TG. Wable GS. Arbuthnott G. Aoki C. Cerebellar sub-divisions differ in exercise-induced plasticity of noradrenergic axons and in association with resilience to activity-based anorexia. Brain Struct Funct 2017; 222(1): 317-339

Neves G. Cooke SF. Bliss TV. Synaptic plasticity. memory and the hippocampus: a neural network approach to causality. Nat Rev Neurosci 2008; 9(1): 65-75

Niwa N. Wang W. Sha Q. Marionneau C. Nerbonne JM. Kv4.3 is not required for the generation of functional Ito.f channels in adult mouse ventricles. J Mol Cell Cardiol 2008; 44(1): 95-104

Ophoff RA. Terwindt GM. Vergouwe MN. van Eijk R. Oefner PJ. Hoffman SM. Lamerdin JE. Mohrenweiser HW. Bulman DE. Ferrari M. Haan J. Lindhout D. van Ommen GJ. Hofker MH. Ferrari MD. Frants RR. Familial hemiplegic migraine and episodic ataxia type-2 are caused by mutations in the Ca2+ channel gene CACNL1A4. Cell 1996; 87(3): 543-52

Orr HT. Chung MY. Banfi S. Kwiatkowski TJ Jr. Servadio A. Beaudet AL. McCall AE. Duvick LA. Ranum LP. Zoghbi HY. Expansion of an unstable trinucleotide CAG repeat in spinocerebellar ataxia type 1. Nat Gene. 1993; 4(3): 221-6

Palay SL. Chan-Palay V. A guide to the synaptic analysis of the neuropil. Cold Spring Harb Symp Quant Biol 1976; 40: 1-16

PALAY SL. PALADE GE. The fine structure of neurons. J Biophys Biochem Cytol 1955; 1(1): 69-88

Palkovits M. Mezey E. Hámori J. Szentágothai J. Quantitative histological analysis of the cerebellar nuclei in the cat. I. Numerical data on cells and on synapses. Exp Brain Res 1977; 28(1-2): 189-209

Paulson HL. Shakkottai VG. Clark HB. Orr HT. Polyglutamine spinocerebellar ataxias - from genes to potential treatments. Nat Rev Neurosci 2017; 18(10): 613-626

Perez-Cortes EJ. Islas AA. Arevalo JP. Mancilla C. Monjaraz E. Salinas-Stefanon EM. Modulation of the transient outward current (Ito) in rat cardiac myocytes and human Kv4.3 channels by mefloquine. Toxicol Appl Pharmacol 2015; 288(2): 203-12

Perkins EM. Clarkson YL. Sabatier N. Longhurst DM. Millward CP. Jack J. Toraiwa J. Watanabe M. Rothstein JD. Lyndon AR. Wyllie DJ. Dutia MB. Jackson M. Loss of beta-III spectrin leads to PC dysfunction recapitulating behavior and neuropathology of spinocerebellar ataxia type 5 in humans. J Neurosci 2010; 30(14): 4857-67

Person AL. Raman IM. Synchrony and neural coding in cerebellar circuits. Front Neural Circuits 2012; 6: 97

Picher MM. Oprişoreanu AM. Jung S. Michel K. Schoch S. Moser T. Rab Interacting Molecules 2 and 3 Directly Interact with the Pore-Forming CaV1.3 Ca2+ Channel Subunit and Promote Its Membrane Expression. Front Cell Neurosci 2017; 11: 160

Pin JP. Duvoisin R. The metabotropic glutamate receptors: structure and functions. Neuropharmacology 1995; 34(1): 1-26

Piochon C. Kloth AD. Grasselli G. Titley HK. Nakayama H. Hashimoto K. Wan V. Simmons DH. Eissa T. Nakatani J. Cherskov A. Miyazaki T. Watanabe M. Takumi T. Kano M. Wang SS. Hansel C. Cerebellar plasticity and motor learning deficits in a copy-number variation mouse model of autism. Nat Commun 2014; 5: 5586

Powell CM. Schoch S. Monteggia L. Barrot M. Matos MF. Feldmann N. Südhof TC. Nestler EJ. The presynaptic active zone protein RIM1alpha is critical for normal learning and memory. Neuron 2004; 42(1): 143-53

Raike RS. Weisz C. Hoebeek FE. Terzi MC. De Zeeuw CI. van den Maagdenberg AM. Jinnah HA. Hess EJ. Stress. caffeine and ethanol trigger transient neurological dysfunction through shared mechanisms in a mouse calcium channelopathy. Neurobiol Dis 2013; 50: 151-9

Raman IM. Bean BP. Ionic currents underlying spontaneous action potentials in isolated cerebellar Purkinje neurons. J Neurosci 1999; 19(5): 1663-74

Raman IM. Sprunger LK. Meisler MH. Bean BP. Altered subthreshold sodium currents and disrupted firing patterns in Purkinje neurons of Scn8a mutant mice. Neuron 1997; 19(4): 881-91

Regan LJ. Voltage-dependent calcium currents in Purkinje cells from rat cerebellar vermis. J Neurosci 1991; 11(7): 2259-69

Roh SE. Kim SH. Ryu C. Kim CE. Kim YG. Worley PF. Kim SK. Kim SJ. Direct translation of climbing fiber burst-mediated sensory coding into post-synaptic Purkinje cell dendritic calcium. Elife 2020; 9: e61593

Roome CJ. Kuhn B. Simultaneous dendritic voltage and calcium imaging and somatic recording from Purkinje neurons in awake mice. Nat Commun 2018; 9(1): 3388

Ross WN. Werman R. Mapping calcium transients in the dendrites of Purkinje cells from the guinea-pig cerebellum in vitro. J Physiol 1987; 389: 319-36

Rudy B. McBain CJ. Kv3 channels: voltage-gated K+ channels designed for high-frequency repetitive firing. Trends Neurosci 2001; 24(9): 517-26

Sausbier M. Hu H. Arntz C. Feil S. Kamm S. Adelsberger H. Sausbier U. Sailer CA. Feil R. Hofmann F. Korth M. Shipston MJ. Knaus HG. Wolfer DP. Pedroarena CM. Storm JF. Ruth P. Cerebellar ataxia and Purkinje cell dysfunction caused by Ca2+-activated K+ channel deficiency. Proc Natl Acad Sci USA 2004; 101(25): 9474-8

Schoch S. Gundelfinger ED. Molecular organization of the presynaptic active zone. Cell Tissue Res 2006; 326(2): 379-91

Schoch. S.. Castillo. P. E.. Jo. T.. Mukherjee. K.. Geppert. M.. Wang. Y.. et al. RIM1alpha forms a protein scaffold for regulating neurotransmitter release at the active zone. Nature 2002; 415: 321–326

Serôdio P. Rudy B. Differential expression of Kv4 channel subunits mediating subthreshold transient K+ currents in rat brain. J Neurophy 1998; 79(2): 1081-91

Shakkottai VG. do Carmo Costa M. Dell'Orco JM. Sankaranarayanan A. Wulff H. Paulson HL. Early changes in cerebellar physiology accompany motor dysfunction in the polyglutamine disease SCA3. J Neurosci 2011; 31(36): 13002-14

Smeets CJ. Verbeek DS. Climbing fibers in spinocerebellar ataxia: A mechanism for the loss of motor control. Neurobiol Dis 2016; 88: 96-106

Sotelo C. Wassef M. Cerebellar development: afferent organization and Purkinje cell heterogeneity. Philos Trans R Soc Lond B Biol Sci 1991; 331(1261): 307-13

Stahl JS. James RA. Oommen BS. Hoebeek FE. De Zeeuw CI. Eye movements of the murine P/Q calcium channel mutant tottering and the impact of aging. J Neurophysiol 2006; 95(3): 1588-607

Stocker M. Krause M. Pedarzani P. An apamin-sensitive Ca2+-activated K+ current in hippocampal pyramidal neurons. Proc Natl Acad Sci USA 1999; 96(8): 4662-7

Strupp M. Kalla R. Dichgans M. Freilinger T. Glasauer S. Brandt T. Treatment of EA2 with the K+ channel blocker 4-aminopyridine. Neurology 2004; 62(9): 1623-5

Strupp M. Zwergal A. Brandt T. EA2. Neurotherapeutics 2007; 4(2): 267-73

Südhof TC. The presynaptic active zone. Neuron 2012; 75(1): 11-25

Südhof TC. The synaptic vesicle cycle. Annu Rev Neurosci 2004; 27: 509-47

Swensen AM. Bean BP. Ionic mechanisms of burst firing in dissociated Purkinje neurons. J Neurosci 2003; 23(29): 9650-63

Tank DW. Sugimori M. Connor JA. Llinás RR. Spatially resolved calcium dynamics of mammalian Purkinje cells in cerebellar slice. Science 1988; 242(4879): 773-7

Tara E. Vitenzon A. Hess E. Khodakhah K. Aberrant cerebellar PC activity as a cause of motor attacks in a mouse model of EA2. Dis Model Mech 2018; 11(9): dmm034181

Tsuji S. Meier H. Evidence for allelism of leaner and tottering in the mouse. Genet Res 1971; 17(1): 83-8

Tsuji S. Meier H. Evidence for allelism of leaner and tottering in the mouse. Genet Res 1971; 17(1): 83-8

Uriu Y. Kiyonaka S. Miki T. Yagi M. Akiyama S. Mori E. Nakao A. Beedle AM. Campbell KP. Wakamori M. Mori Y. Rab3-interacting molecule gamma isoforms lacking the Rab3-binding domain induce long lasting currents but block neurotransmitter vesicle anchoring in voltage-dependent P/Q-type channels. J Biol Chem 2010; 285: 21750-67

Vega IE. Hsu SC. The exocyst complex associates with microtubules to mediate vesicle targeting and neurite outgrowth. J Neurosci 2001; 21(11): 3839-48

Wakamori M. Yamazaki K. Matsunodaira H. Teramoto T. Tanaka I. Niidome T. Sawada K. Nishizawa Y. Sekiguchi N. Mori E. Mori Y. Imoto K. Single tottering mutations responsible for the neuropathic phenotype of the P-type calcium channel. J Biol Chem 1998; 273(52): 34857-67

Walter JT. Alviña K. Womack MD. Chevez C. Khodakhah K. Decreases in the precision of Purkinje cell pacemaking cause cerebellar dysfunction and ataxia. Nat Neurosci 2006; 9(3): 389-97

Wang D. Schreurs BG. Characteristics of IA currents in adult rabbit cerebellar Purkinje cells. Brain Res 2006; 1096(1): 85-96

Wang JY. Yu IS. Huang CC. Chen CY. Wang WP. Lin SW. Jeang KT. Chi YH. Sun1 deficiency leads to cerebellar ataxia in mice. Dis Model Mech 2015; 8(8): 957-67

Wang. Y.. and Sudhof. T. C. Genomic definition of RIM proteins: evolutionary amplification of a family of synaptic regulatory proteins. Genomics 2003; 81: 126–137

Wang. Y.. Okamoto. M.. Schmitz. F.. Hofmann. K.. and Sudhof. T. C. Rim is a putative Rab3 effector in regulating synaptic-vesicle fusion. Nature 1997; 388: 593–598

Wang. Y.. Sugita. S.. and Sudhof. T. C. The RIM/NIM family of neuronal C2 domain proteins. Interactions with Rab3 and a new class of Src homology 3 domain proteins. J. Biol. Chem 2000; 275: 20033–20044

Watanabe M. Kano M. Climbing fiber synapse elimination in cerebellar Purkinje cells. Eur J Neurosci 2011; 34(10): 1697-710

Waters MF. Minassian NA. Stevanin G. Figueroa KP. Bannister JP. Nolte D. Mock AF. Evidente VG. Fee DB. Müller U. Dürr A. Brice A. Papazian DM. Pulst SM. Mutations in voltage-gated potassium channel KCNC3 cause degenerative and developmental central nervous system phenotypes. Nat Genet 2006; 38(4): 447-51

Weidenhofer J. Bowden NA. Scott RJ. Tooney PA. Altered gene expression in the amygdala in schizophrenia: up-regulation of genes located in the cytomatrix active zone. Mol Cell Neurosci 2006; 31(2): 243-50

Weidenhofer J. Scott RJ. Tooney PA. Investigation of the expression of genes affecting cytomatrix active zone function in the amygdala in schizophrenia: effects of antipsychotic drugs. J Psychiatr Res 2009; 43(3): 282-90

Weiser M. Vega-Saenz de Miera E. Kentros C. Moreno H. Franzen L. Hillman D. Baker H. Rudy B. Differential expression of Shaw-related K+ channels in the rat central nervous system. J Neurosci 1994; 14(3 Pt 1): 949-72

Westenbroek RE. Merrick DK. Catterall WA. Differential subcellular localization of the RI and RII Na+ channel subtypes in central neurons. Neuron 1989; 3(6): 695-704

White JJ. Sillitoe RV. Postnatal development of cerebellar zones revealed by neurofilament heavy chain protein expression. Front Neuroanat 2013; 7: 9

Witter L. Rudolph S. Pressler RT. Lahlaf SI. Regehr WG. Purkinje Cell Collaterals Enable Output Signals from the Cerebellar Cortex to Feed Back to Purkinje Cells and Interneurons. Neuron 2016; 91(2): 312-9

Womack M. Khodakhah K. Active contribution of dendrites to the tonic and trimodal patterns of activity in cerebellar Purkinje neurons. J Neurosci 2002; 22(24): 10603-12

Womack MD. Chevez C. Khodakhah K. Calcium-activated potassium channels are selectively coupled to P/Q-type calcium channels in cerebellar Purkinje neurons. J Neurosci 2004; 24(40): 8818-22

Womack MD. Hoang C. Khodakhah K. Large conductance calcium-activated potassium channels affect both spontaneous firing and intracellular calcium concentration in cerebellar Purkinje neurons. Neuroscience 2009; 162(4): 989-1000

Xia XM. Fakler B. Rivard A. Wayman G. Johnson-Pais T. Keen JE. Ishii T. Hirschberg B. Bond CT. Lutsenko S. Maylie J. Adelman JP. Mechanism of calcium gating in small-conductance calcium-activated potassium channels. Nature 1998; 395(6701): 503-7

Yang Y. Sun K. Liu W. Zhang L. Peng K. Zhang S. Li S. Yang M. Jiang Z. Lu F. Zhu X. Disruption of Tmem30a results in cerebellar ataxia and degeneration of Purkinje cells. Cell Death Dis 2018; 9(9): 899

Zagha E. Lang EJ. Rudy B. K_v3.3 channels at the PC soma are necessary for generation of the classical CS waveform. J Neurosci. 2008; 28(6): 1291-300

Zhang CL. Messing A. Chiu SY. Specific alteration of spontaneous GABAergic inhibition in cerebellar purkinje cells in mice lacking the potassium channel Kv1. 1. J Neurosci 1999; 19(8): 2852-64

Zoghbi HY. Orr HT. Pathogenic mechanisms of a polyglutamine-mediated neurodegenerative disease. spinocerebellar ataxia type 1. J Biol Chem 2009; 284(12): 7425-9

9. Acknowledgements

It has been a long journey to get to this point, spanning over 5 years from November 2017 to May 2023. Throughout my PhD, I encountered numerous challenges, including struggling with "not-working" experiments, deciphering "incomprehensible" data that appeared to me as mere sets of numbers, and more. However, reaching this final summit of my PhD has become a reality. It would not have been possible without the help and support of the people around me, and for that I would like to express my deepest gratitude to them.

I would like to express my gratitude to my family for their unwavering trust and support throughout my journey. I got married during my PhD, and last year we welcomed a baby into our world. These are the most previous gifts and have been the main source of strength that propelled me forward.

I would like to thank Prof. Dirk Dietrich and Prof. Susanne Schoch for their guidance and support throughout my PhD projects. I started my RIM4 project from January 2017 as a Master's thesis, and it has been an exciting time investigating lots of captivating data sets. They have been instrumental in helping me decipher the data, enabling us to gain a better understanding of the role of RIM4. I vividly remember when Prof. Dirk. Dietrich advised me to become a friend of Igor Pro software, and I eventually became its closest ally. I'm able to do anything with Igor Pro thanks to you.

I would like to thank all members of the AG Dietrich and AG Schoch for their help, support, discussion, critics, suggestions, feedback, and lots of fun moments we've shared. It has been a wonderful time being your colleague.

And also a shoutout to all of my friends who have been by my sides no matter what, when, and how.